LEABHARLANN CHOLÁISTE NA TRÍONÓIDE, BAILE ÁTHA CLIATH | TRINITY COLLEGE LIBRARY DUBLIN
Ollscoil Átha Cliath | The University of Dublin

Terms and Conditions of Use of Digitised Theses from Trinity College Library Dublin

Copyright statement

All material supplied by Trinity College Library is protected by copyright (under the Copyright and Related Rights Act, 2000 as amended) and other relevant Intellectual Property Rights. By accessing and using a Digitised Thesis from Trinity College Library you acknowledge that all Intellectual Property Rights in any Works supplied are the sole and exclusive property of the copyright and/or other IPR holder. Specific copyright holders may not be explicitly identified. Use of materials from other sources within a thesis should not be construed as a claim over them.

A non-exclusive, non-transferable licence is hereby granted to those using or reproducing, in whole or in part, the material for valid purposes, providing the copyright owners are acknowledged using the normal conventions. Where specific permission to use material is required, this is identified and such permission must be sought from the copyright holder or agency cited.

Liability statement

By using a Digitised Thesis, I accept that Trinity College Dublin bears no legal responsibility for the accuracy, legality or comprehensiveness of materials contained within the thesis, and that Trinity College Dublin accepts no liability for indirect, consequential, or incidental, damages or losses arising from use of the thesis for whatever reason. Information located in a thesis may be subject to specific use constraints, details of which may not be explicitly described. It is the responsibility of potential and actual users to be aware of such constraints and to abide by them. By making use of material from a digitised thesis, you accept these copyright and disclaimer provisions. Where it is brought to the attention of Trinity College Library that there may be a breach of copyright or other restraint, it is the policy to withdraw or take down access to a thesis while the issue is being resolved.

Access Agreement

By using a Digitised Thesis from Trinity College Library you are bound by the following Terms & Conditions. Please read them carefully.

I have read and I understand the following statement: All material supplied via a Digitised Thesis from Trinity College Library is protected by copyright and other intellectual property rights, and duplication or sale of all or part of any of a thesis is not permitted, except that material may be duplicated by you for your research use or for educational purposes in electronic or print form providing the copyright owners are acknowledged using the normal conventions. You must obtain permission for any other use. Electronic or print copies may not be offered, whether for sale or otherwise to anyone. This copy has been supplied on the understanding that it is copyright material and that no quotation from the thesis may be published without proper acknowledgement.

Characterisation of Laser Produced Plasmas

Brendan Doggett

Submitted for the degree of
Doctor of Philosophy
School of Physics
University of Dublin
Trinity College

TRINITY COLLEGE
15 MAY 2006
LIBRARY DUBLIN
THOSIS
7907

Declaration

This thesis has not been submitted as an exercise for a degree in any other university.

This thesis is entirely my own work, except for the advice and assistance mentioned in the acknowledgements and the collaborative work mentioned in the list of publications.

I agree to allow the library of Trinity College Dublin copy or lend a section or this entire thesis on request.

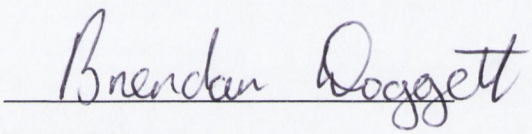

Brendan Doggett

March 2006

Summary

This thesis describes the application of planar Langmuir probes in laser produced plasmas. The influence of the ion flow on the probe behaviour and its effect on the measured plasma parameters has been investigated for different probe orientations. The expansion dynamics of the laser produced plasma were studied using the probes and the results obtained were compared to adiabatic expansion models.

The application of Langmuir probes to the plasma was considered in terms of the possible perturbation of the plasma and sheath effects. It was suggested that rotating the probe so that its surface was aligned parallel to the flow would eliminate the ion current due to the flow and so increase the accuracy of the results. In this orientation better agreement was found with the isentropic expansion models. In addition we showed that the plasma immersion implantation models could be used to describe the ion current to the probe and indirectly determine the electron temperature.

Finally the plume was analysed using an energy selective-time of flight mass analyser. The mass-to-charge ratios and the energy distributions of the various ions could be determined and compared to the energy distributions obtained from the ion probe results.

Acknowledgements

Acknowledgements; the last to be written yet the first (and sometimes only part) to be read. It won't do justice to everyone but still……

To my parents, particularly my mother, for selflessly providing me with every opportunity in life. This thesis is for you guys.

To Andrew, Anita, Lauren, Ruth and Chris; well what can I say? Thanks for your help, lifts, clothes, money and for popping in whenever you could. Much appreciated. As for you Patsy; Happy Birthday! A special mention to Niall; you've provided some high points over the past few years. Those days and nights in Risø, Flannerys, Whelan's, Neds, the Point, the Vibe and the RDS……..

A special thanks to Master Reilly and Reverend Cowan for many interesting debates and pints at PN.

Thank you to my supervisor, James Lunney, for giving me the opportunity to complete this work. Your advice and encouragement over the past few years is sincerely appreciated. Thanks to Yitzhak Kaufman for some very useful discussion during his time here, to Bo Toftmann and Jørgen Schou during my time in Roskilde and Crete and to Peter Sheerin and Myles Turner for our collaboration during the past few years. The staff of the physics department, (school of physics?) deserve particular mention. To Ken, Joe, Pat, Mick and Dave; thanks for the help in (and outside) the lab.

Thanks to my fellow researchers past and present; particularly members of group D. Thanks Chris for opening my eyes to the far-east and Lee for giving me a few black ones in the squash court. I've been very lucky to work with some great guys in group L. Working backwards there's Tonii, Fintan, Amit and Casper among many others; thanks for the help (and coffee), particularly over the last few months. I have fond memories when I first started of the three amigos; Tue, Donagh and Eduardo. The mad dog of Dingle still lives.

Finally and most importantly thank you Miriam. You've kept me going and have made the last few years the best of my life. Níl aon leigheas ar an ngrá ach pósadh.

Table of contents

Introduction **1**

Diagnostic Techniques: 3

Outline of the thesis 5

References: 7

1. Theory and modelling **8**

1.1 Laser heating of the target 9

1.1.1 Model Output 11

1.2 Plasma Ionisation 13

1.3 Expansion of the laser ablation plume 15

1.3.1 Isentropic plasma expansion 17

1.3.2 Isothermal plume expansion 23

1.4 Conclusions 28

1.5 References 29

2. Experimental Methods **31**

2.1 Experimental Setup 31

2.2 Plasma characterisation techniques 33

2.2.1 Langmuir probe 33

2.2.2 Energy Selective-Time of Flight Mass Spectrometer 35

2.3 Estimated errors 38

2.4 References 39

3. Langmuir Probe **40**

3.1 Plasma equilibrium 41

3.2 Probe Regime 45

3.3 Probe theory 48

3.4 Probe Perturbation 52

3.5 Probe size, sheath and edge effects 56

3.6 Conclusion I 59

3.7 Ion velocity and energy distribution 60

3.8 Probe rotation 62

3.9 Plasma immersion ion implantation 66

3.9.1 Lieberman model 68

3.9.2 Riemann & Daube model 70

3.9.3 Sheerin & Turner model 72

3.10 Comparison of Models 73

3.11 Conclusions II 74
3.12 References 75
4. Experimental Results 77
4.1 Probe orientation 78
4.2 Plane probe perpendicular to flow 79
4.2.1 Ion angular distribution 81
4.2.2 Ion and neutral distribution 83
4.2.3 Electron temperature 85
4.3 Plane probe aligned parallel to flow 89
4.4 PIII Models 91
4.5 Conclusion I 96
4.6 Multiply ionised species and contamination 98
4.7 Energy Selective-Time of Flight Mass Spectrometer 101
4.8 Conclusions II 110
4.9 References 111
Conclusions and future work 112
Appendix A: Laser heating model 115
Appendix B: Light transmission calculation 118
Appendix C: Publications 119

Introduction

In 1954, Charles Townes and Arthur Schawlow invented the maser (**m**icrowave **a**mplification by **s**timulated **e**mission of **r**adiation), using ammonia gas and microwave radiation. By the late 1950s scientists all over the world were trying to develop an optical maser. While employed at Hughes Research Laboratories as a section head in May 1960, Theodore Maiman developed, demonstrated, and patented a laser using a pink ruby medium with silvered ends, for which he gained worldwide recognition. His ruby laser was eight inches long and produced a single pure frequency of deep red light (694.3 nm). The first gas laser, a helium-neon with a wavelength of 1150 nm, was produced in December of the same year and during the following years the area exploded with the CO_2 and Nd:YAG lasers created by 1964.

Initially, theoretical and experimental studies on the interaction of laser beams with solid, liquid, and gaseous materials were carried out. The ease with which material could be vaporised led to the first deposition of a thin film by Smith and Turner in 1965 [1]. However the limitations in the wavelength and the peak power meant that the material selection was limited and the film quality was poor in comparison to other techniques available at the time. It was not until the mid 1970s with two major developments that greater interest in laser technology took place. First, electrically Q-switched lasers became available. These could generate very short pulses with a peak power exceeding 10^8 Wcm^{-2}. The second advance was the development of a high-efficiency second harmonic generator to deliver shorter wavelength light. Up until the 1990s the most common lasers used in material science were the CO_2 and the Nd:YAG but the availability of lasers in the ultraviolet regime resulted in a lower absorption depth and hence heated volume. In general, the most useful range of laser wavelengths for material processing lie between 200 to 400 nm, as most materials show strong absorption in this region. Together these two developments widened the material choice and improved the overall film quality.

For the laser material interaction the main parameters are the surface reflectivity at the particular laser wavelength, the optical absorption depth and the thermal diffusion depth. The optical absorption depth is given by: $d_{opt} = \frac{\lambda}{4\pi k}$, where k is the extinction coefficient.

The thermal diffusivity is given by:

$$D = \frac{k}{\rho c_p}$$

where k, ρ and c_p are the thermal conductivity, density and specific heat capacity respectively. The heat diffusion depth is then defined as:

$$d_{th} = 2\left(D\tau_p\right)^{1/2}$$

where τ_p is the length of the laser pulse. In metals the laser radiation is absorbed by the excitation of free electrons. The excited electrons thermalise rapidly by electron-electron collisions, with a characteristic relaxation time; τ_e. Energy from the electrons is then transferred to the lattice by electron-phonon interactions characterised by; τ_l, where $\tau_e \ll \tau_l$.

For various pulse lengths three situations can arise. For relatively long pulses, i.e. nanosecond pulses, $\tau_e \ll \tau_l \ll \tau_p$. The pulse length is sufficiently long for extensive heating of the target to occur resulting in a large molten zone. For a 6 nanosecond (ns) pulse the heat diffusion depth in silver, the best conductor of all, is $d_{th} \approx 1$ μm, which is much larger than the optical absorption depth $d_{opt} \approx 20$ nm at a wavelength of 250 nm. For picoseconds pulses (ps), $\tau_e \ll \tau_l \approx \tau_p$, the pulse length is at least comparable with the electron-phonon relaxation time. In this regime $d_{th} \sim 10$ nm for metals and heating of the target allows molten material to form. For femtosecond pulses, (fs), $\tau_e \ll \tau_p \ll \tau_l$, the pulse length is shorter than the electron-phonon relaxation by three orders of magnitude so in this regime d_{th} is confined to the surface and heat conduction into the target can be neglected within the time duration of the pulse. The choice of pulse length and wavelength finally depends on the choice of laser application.

Up until the late 1980s the principle application of laser ablation was in optical and mass spectrometry for chemical analysis. It now includes a growing number of applications such as Pulsed Laser Deposition (PLD), nanoparticle production, micro machining and surgery. The PLD process became widespread after the production of a thin film of the high temperature superconductor YBCO by Venkatesan [2] in 1987.

It is now used to deposit multi-component targets, dielectrics and glasses. Laser ablation using fs pulses has many interesting features. It has been shown recently to produce nanoparticles during ablation and can have several advantages over more standard techniques.

Laser ablation can also be used in several analytical technique. These include matrix assisted laser desorption ionisation (MALDI), laser micro-probe mass spectrometry (LMMS) and laser induced breakdown spectrometry (LIBS). For example LIBS uses a short-pulsed laser (~7 ns) focused on the sample to be analysed to create a plasma. The plasma consists of neutrals and charged species and radiates at specific wavelengths depending on the elements. By capturing the light the elements are identified by their specific wavelengths and the abundances are measured by the intensity of the light at specific wavelengths.

Diagnostic Techniques:

A plasma, by definition, is charge neutral with equal number of positive and negative charges. Its key parameters are the density and temperature of its constituents. There are many techniques available to determine these parameters such as optical spectroscopy, photographic techniques, mass spectroscopy and charge collection. Optical spectroscopy and interferometry techniques are particularly useful in analysing the plume expansion close to the target. Among other methods, relative line intensity measurements are the most common technique to determine the temperature in a laser-produced plasma. This technique is due to the fact that densities of atoms in various states are proportional to the exponentials of the negative ratios between the excitation energy and the thermal energy. Photographic techniques such as gated ICCD photography can be used to characterise the expansion of the plume in vacuum or in the presence of a background gas [3].

The characterisation by charged species analysis is important as the plasma can be highly ionised with energetic ions (10 – 200 eV), which can influence the growth process during PLD. Techniques such as time-of-flight mass spectroscopy (TOFMS) allows mass identification and energy analysis to be performed simultaneously and on a shot to shot basis. TOFMS contains various methods such as linear-TOFMS where the spectrometer is mounted along the direction of the plume expansion, and reflectron-TOFMS where an ion reflector is used to improve mass resolution.

Charge collection techniques are possibly the most common diagnostic technique used to characterise a plasma. The charge is collected using an electrostatic probe immersed in the plasma. The use of electrostatic probes to obtain localised information of plasma parameters is a well-established technique dating back to 1923, where it was first introduced by Langmuir and Mott-Smith [4], and as such it is commonly referred to as a Langmuir probe. The literature provides numerous experiments and review articles concerning the device with some of the most comprehensive being by Demidov *et al* [5] and Chen [6].

Conceptually a Langmuir probe is a very simple device. It consists of a small metallic electrode inserted into the plasma and connected externally to an electrical circuit. In some cases a honeycombed structure is used to overcome secondary electron emission. The circuit allows the probe be biased positively or negatively with respect to the plasma potential and an oscilloscope is then used to determine the voltage drop across a resistor. Its most common application is in recording the TOF spectra of positive ions within the plume. If the laser produced plasma can be considered to have rapid acceleration then the TOF spectra can be converted into kinetic energy distributions. When the current to the probe is measured for a range of probe potentials a current-voltage (IV) characteristic is obtained from which several plasma parameters such as density and temperature can be determined.

Unfortunately, in contrast to the simple design, the theory for describing the probe response is rather complicated. The reason is that the probe is a boundary to the plasma and due to charge neutrality the probe potential will only affect the electrons a short distance from the probe. This region is called the sheath and within it the equations of motion change and quasi-neutrality cease to be fulfilled [7]. A full description and analysis of the theory used to interpret the probe results will be presented in the following chapters.

Outline of the thesis

The aim of this thesis is to advance the understanding and application of Langmuir probes in laser produced plasmas. We attempt to understand the effect of the plasma flow on the probe behaviour and provide a new method to determine the plasma parameters.

This thesis can be divided into two main themes; a description of the ablation process, plasma formation and subsequent expansion, and the identification and characterisation of the plasma using various techniques. The individual chapter content can be summarised as follows.

Chapter 1: Theory and modelling

This chapter introduces the theory used to develop a number of models of the ablation process. These include a model for the laser heating of a target and the subsequent evaporation of material[8]. We also introduce the isentropic hydrodynamic expansion model for a plume into vacuum by Anisimov [9] and the isothermal model of Singh and Narayan [10].

Chapter 2: Experimental method

The experimental setup is presented in this chapter. Techniques that are used for the analysis of the plasma such as a Langmuir probe and a mass-to-charge analyser will be introduced. Finally estimates of the errors will be presented.

Chapter 3: Langmuir probe

This chapter describes the general theory for Langmuir probes. Particular emphasis is placed on its application to a laser produced plasma. A model to describe the probe behaviour for when its surface is aligned parallel to the ion flow is presented.

Chapter 4: Results

This final chapter presents the general results obtained for the ablation of silver. The results of particle density and temperature from different probe orientations are compared and finally the results from the mass-to-charge analyser are presented.

Appendix A:

Laser heating model

Appendix B:

Light transmission technique

Appendix C:

List of Publications

References:

1. Smith, H.M. and Turner, A.F., *Applied Optics*, **4**: p. 147(1965).
2. Dijkkamp, D., *et al.*, *Applied Physics Letters*, **51**(8): p. 619(1987).
3. Geohegan, D.B. and Puretzky, A.A., *Applied Physics Letters*, **67**(2): p. 197(1995).
4. Langmuir, I. and Mott-Smith, H.M., *Gem. Electr. Rev.*, **26**: p. 731(1923).
5. Demidov, V.I., Ratynskaia, S.V., and Rypdal, K., *Review of Scientific Instruments*, **73**(10): p. 3409(2002).
6. Chen, F.F., *Introduction to plasma physics and controlled fusion*. 2nd ed. 1984, New York: Plenum Press.
7. Riemann, K.U., *Journal of Physics D (Applied Physics)*, **24**(4): p. 493(1991).
8. Lunney, J.G. and Jordan, R., *Applied Surface Science*, **127-129**: p. 941(1998).
9. Anisimov, S.I., Luk'yanchuk, B.S., and Luches, A., *Applied Surface Science*, **96-98**: p. 24(1996).
10. Singh, R.K. and Narayan, J., *Phys. Rev. B*, **41**(13): p. 8843–8859 (1990).

1. Theory and modelling

The laser solid interaction and plasma formation is a complicated process since the laser absorption and subsequent material removal are characterised by different but interconnecting processes. The laser ablation process is generally broken into two stages. The first is the evaporation and ionisation of material from the target and the second is the plume expansion. The laser light strikes the target and interacts with the electrons in the solid. The excited electrons then collide with the lattice phonons and transfer the absorbed energy to the lattice. Since the energy relaxation time is of the order of ps for metals [1, 2] the optical energy can be thought of as being instanteously turned into heat for ns ablation.

The reflection of the laser light from the target is an important parameter which affects the efficiency of the ablation. For metals in the UV regime it can be quite low, for example silver at 248 nm the reflectivity is 0.25. As the laser heats the target the temperature increases rapidly with temperatures up to several thousand Kelvin easily achieved and as a result vaporisation becomes significant. The plasma, which primarily consists of atoms, ions and electrons may also contain nano and micro-particles. As the plasma is produced in front of the target, it will begin to absorb the incoming light leading to further heating and ionising of the plume and a reduction in the laser intensity reaching the target. The laser light is absorbed primarily by inverse Bremsstrahlung (IB) (electron-neutral or electron-ion), which involves the absorption of a photon by a free electron (within the field of a heavy particle to conserve momentum) and by direct single-photon excitation processes. For IR laser ablation absorption by IB is dominant while for visible and UV wavelengths, photoionisation is the dominant ionisation process. At the end of the pulse the layer of plasma can be tens of microns thick and have a high internal pressure which drives its subsequent expansion.

In the literature a variety of models for laser ablation exist for various experimental conditions [3]. A large number are based on thermal processes, which describe the laser-target interaction using the thermal heat conduction equation [4]. This is suitable for ns pulses whereas for ps and fs a two-temperature model is needed as the optical energy cannot be considered as being instantaneously turned into heat [5].

The first step of modelling laser ablation for a solid is usually to determine the surface temperature.

1.1 Laser heating of the target

The following model is similar to that developed by Jordan and Lunney [6] and we present the main features here. We described in the introduction that for ns pulses the penetration depth is much less than the heat diffusion depth and so the energy flux from the laser can be treated as a source term at the surface. One-dimensional heat conduction equations can be used since the laser spot dimensions are orders of magnitude larger than the heat conduction depth. It is then possible to use Duhamel's theorem [7] to describe the surface temperature change of the target for a time-varying heat source [8].

$$T_s(t) = \frac{1}{\sqrt{\kappa\rho\pi c_p}} \int_0^t \frac{I(t-\tau)}{\sqrt{\tau}} d\tau \tag{1.1}$$

where I is the energy flux at the target surface, and κ, ρ and c_p are the thermal conductivity, mass density and specific heat capacity of the target respectively. The irradiance, I, contains a term that takes into account absorption by the evaporated particles, ρ_{vap}. The irradiance is expressed as follows:

$$I(t) = (1-R) I_l(t) \exp\left[-\frac{\sigma_{vap}\rho_{vap}}{\cos\theta} \right] \tag{1.2}$$

$$\rho_{vap}(t) = \int_0^t j_{vap} d\tau$$

I_l is the input laser intensity at the target before accounting for the reflectivity of the target surface, R. The intensity was obtained by fitting the laser pulse profile measured using a fast photodiode. σ_{vap} is the photo-absorption cross-section at the laser wavelength and is taken as the threshold value of the hydrogen-like photoionisation cross-section. From [9] it is of the order 10^{-17} cm^2. θ is the angle of incidence of the laser beam with respect to the target normal , ρ_{vap} is the total number of vapour particles accumulated up to a time t, and finally j_{vap} is the evaporation rate.

The evaporation rate is determined by the surface temperature and pressure and can be calculated using the Hertz-Knudsen equation for evaporation:

$$j_{vap} = p_s \times \sqrt{\frac{1}{2\pi k_B u M_{mol} T_s}} \quad (1.3)$$

where u is the atomic mass unit, M_{mol} is the molar mass and p_s is the pressure above the surface. An additional factor is sometimes included to account for recondensation at the surface and is referred to as the sticking coefficient 's'.

In the case where a material evaporates as single atoms or molecules the vapour pressure above the surface is commonly expressed in terms of latent heat of evaporation per particle (L_v) in the form of the Clausius-Clapeyron equation:

$$\frac{p_s}{p_0} = \exp\left[\frac{L_v}{k_B}\left(\frac{1}{T_0} - \frac{1}{T_s}\right)\right] \quad (1.4)$$

where p_0 is the equilibrium vapour pressure at a specific temperature T_0, which is usually taken as the boiling point. The calculation was carried out using the Mathematica software and the code is presented in Appendix A.

1.1.1 Model Output

From the previous calculations it is possible to estimate some of the ablation parameters. Fig.1.1 shows the output from the model for the change in surface temperature and ablation rate with fluence. As yet, other parameters that affect the ablation process such as re-radiation from the plasma and change in reflectivity due to surface roughening are not included.

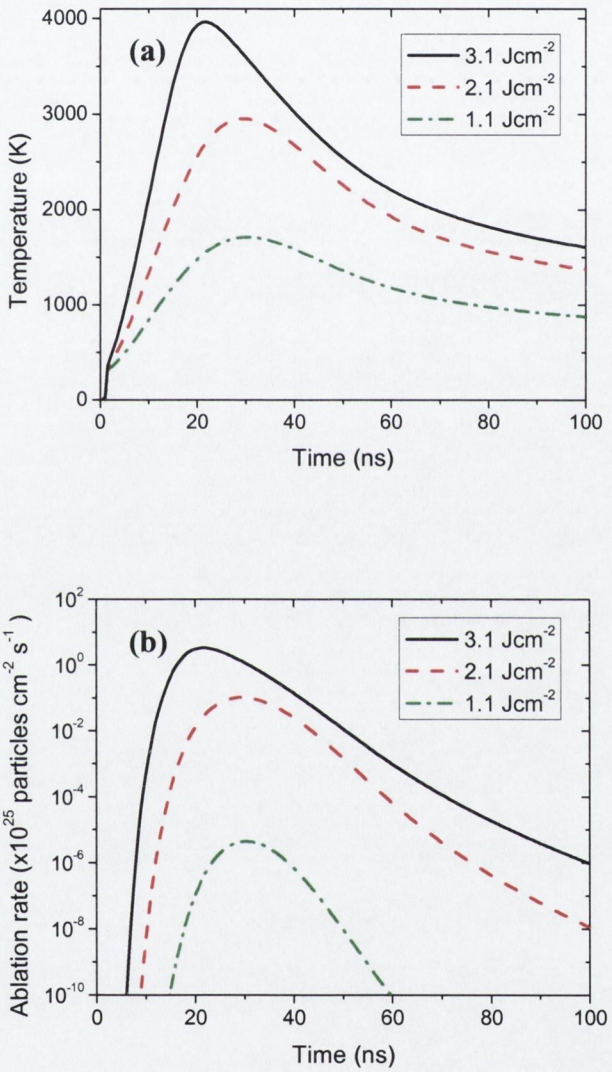

Fig.1.1(a) The surface temperature for a range of fluences **(b)** The ablation rate determined from (1.3). Note the log scale on the y-axis.

Table 1 Estimates from the model for the ablation of silver with a spot size of 2 x 1.5 mm^2

Fluence (J cm^{-2})	Mass Loss (ng)	Ablation Depth (nm)
1	0.0056	0.0002
1.5	1.3	0.04
2	24.3	0.8
5	561	18

If we look at the results obtained for a fluence of 2 J cm^{-2}, the mass loss corresponds to an ablation rate of 1.3×10^{14} atoms / pulse. It is important to note that in these calculations, material removal is solely attributed to vaporisation, whereas in laser ablation splashing of the molten material can be significant. The results should therefore be considered to represent a lower limit of the ablation depth.

1.2 Plasma Ionisation

A mean ionisation, $\bar{Z}$, is often assigned to the plasma. We shall estimate the mean ionisation of the plume using the semi-analytical approach by Zel'dovich and Raizer [9]. A comparison with a plasma physics code "FLY" by Lee [10] was carried out in the thesis of Hansen [11] and showed good agreement with the analytical approach. The approximation by Zel'dovich and Raizer starts with the Saha-equation relating the particle populations of the various ionisation stages in the plasma, with the plasma assumed to be in local thermodynamic equilibrium. From the Saha equation:

$$\frac{n_e n_{m+1}}{n_m} = 2\frac{g_{m+1}}{g_m}\left(\frac{2\pi m_e kT}{h^2}\right)^{3/2} \exp\left(-\frac{I_{m+1}}{kT}\right) \tag{1.5}$$

where n_e and n_m are the electron density and ion density of the m ionised ion. g_m is the statistical weight of an m-ion in its ground state and I_{m+1} is the ionisation potential of the m-ion in its ground state.

The method is based on two steps. First it is assumed that the ion number density n_m and the ionisation potentials I_{m+1} are considered to be continuous functions of the ionic charge m. These are obtained by connecting the discrete values of n_m and I_{m+1} by a continuous curve. The system of recurrence relations defined by the Saha equation can then be transformed into a differential equation for the function n(m) by replacing the finite differences by differentials:

$$n(m+1) = n(m) + dn/dm \tag{1.6}$$

The Saha equations can then be replaced with one differential equation:

$$\left(1+\frac{d\ln n}{dm}\right) n_e = AT^{3/2}\exp\left(-\frac{I(m+1)}{kT}\right) \tag{1.7}$$

where $A = 2\times\left(2\pi m_e k/h^2\right)^{3/2} = 4.8\times10^{21}\ K^{-3/2}\ m^{-3} = 6\times10^{21}\ eV^{-3/2}cm^{-3}$. It is assumed that the ratio of the statistical weights is ~1.

The distribution function n(m) has a very narrow and sharp peak about some value m_{max} which depends on the density and temperature of the plasma. The second step is to assume that the average value of the ionic charge, $\bar{m}$, is equal to the value m_{max} where the function n(m) has a maximum. The narrower and more sharp this peak is, the better the approximation.

Finally it is argued that the average value of the ionisation potential should be referred to the point $m + \frac{1}{2}$ on the graph of I_{m+1} vs. m. This results in the following transcendental equation for $\bar{m}(T,n)$, which can be used to predict the mean ionisation:

$$I\left(\bar{m} + \tfrac{1}{2}\right) = kT \ln\left(AT^{3/2}/\bar{m}n\right) \tag{1.8}$$

Starting with a value of m and temperature, the right hand side can be calculated. Then using the interpolation curve of I_{m+1} vs. m a new value of m is found and this is continued until the value converges. This is then the average ionic charge, $\bar{Z} = \bar{m}$.

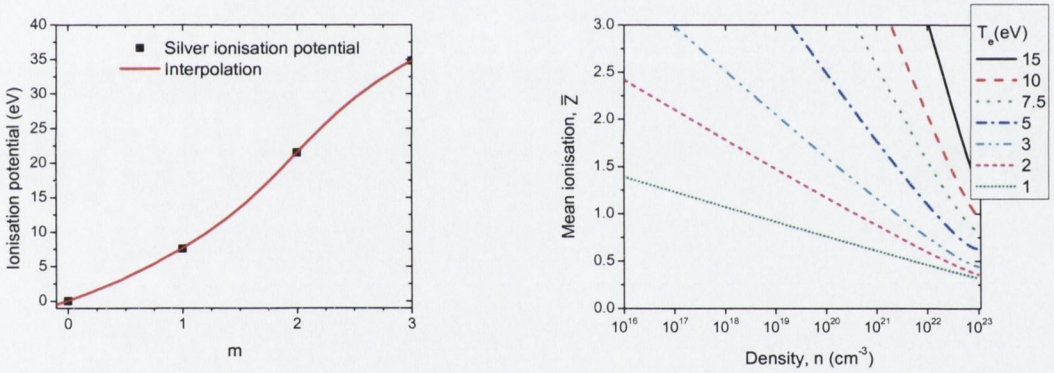

(a) **(b)**

Fig. 1. 2 (a) The interpolation curve to the ionisation potential used with (1.8) for the calculations in (b). **(b)** The average ionic charge as a function of density.

If we take the results from the model in the previous section, for a fluence of 2 J cm^{-2} the ablation rate was 1.3 x 10^{14} atoms / pulse. For the spot size of 2 x 1.5 mm^2 and taking a thickness of 50 μm, the density corresponds to ~10^{18} cm^{-3}. From Fig.1.2 (b) for a temperature between 2–4 eV, the mean ionisation falls between 2–3.

1.3 Expansion of the laser ablation plume

At the end of the laser pulse there remains a dense layer of plasma ($10^{15} - 10^{16}$ atoms) with initial dimensions X_o, Y_o and Z_o (Fig.1.3). X_o and Y_o correspond to the laser spot dimensions and Z_o can be tens of microns thick.

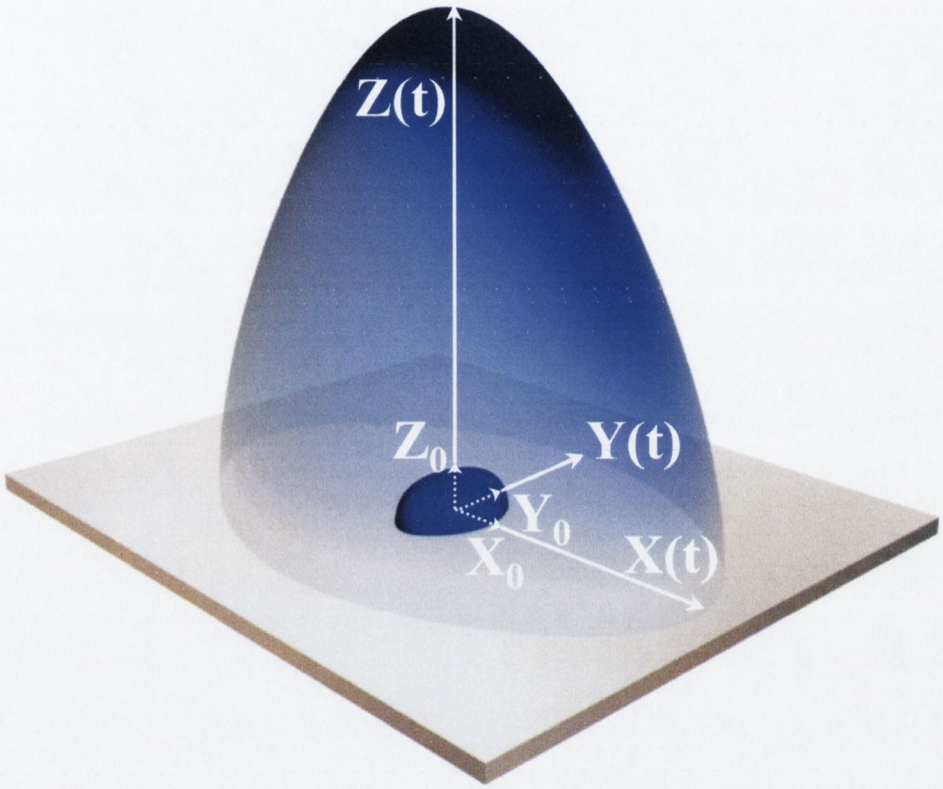

Fig.1.3. The initial dimensions of the plasma plume at the end of the laser pulse, t = 0, and its dimensions after a time t.

As there is little further energy or mass contribution to the plume, its expansion can be considered as adiabatic. The behaviour of the plasma expansion depends primarily on the initial plume dimensions and background gas pressure. At low gas pressures ($< 10^{-3}$ mbar) the expansion is essentially self-similar after an initial acceleration phase of a few mm. After this phase the plume velocity remains nearly constant. In the presence of a background gas the expanding plasma interacts with the gas molecules leading primarily to spatial confinement. Plume splitting and braking of the expansion can occur with even the possibility of the plume moving backwards. Plume splitting occurs when a component of

the plasma travels through the gas experiencing little or no collisions, while a slower component is formed after it interacts with the gas, losing momentum and decelerating. After a period of time the two components will be spatially separated. It is generally characterised by the detection of two peaks in TOF studies of the plasma.

The plume expansion can be investigated using hydrodynamic models, by Monte Carlo simulations or a combination of both [12], and in a background gas, shock wave theories such as the Sedov-Taylor and Freiwald-Axford models have been used [13]. In this work we concentrate on the isentropic model developed by Anisimov [14] and the isothermal model of Singh and Narayan [15] for vacuum.

1.3.1 Isentropic plasma expansion

Anisimov treated the adiabatic expansion of a one-component vapour cloud into vacuum using a particular solution of the gas-dynamic equations, which applies when describing flows with self similar expansion. It is assumed that the formation time of the vapour cloud is much less than its expansion time and that the focal spot of the laser has an elliptical shape with semi-axes X_0 and Y_0. The expansion is modeled as a triaxial gaseous semi-ellipsoid whose semi-axes are initially equal to X_0, Y_0 and $Z_0 \approx c_s\tau_p$, where τ_p is the duration of the laser pulse, and c_s is the sound speed in the vaporised material given by:

$$c_s = \left(\gamma(\gamma-1)\varepsilon\right)^{1/2}$$

γ is the ratio of the plasma specific heats and $\varepsilon = E_p / M_p$ (E_p is the energy of the plume and M_p is its mass) . The adiabatic index, γ, of a gas is the ratio of its specific heat capacity at constant pressure (C_P) to its specific heat capacity at constant volume (C_V). To understand the definition, consider the following experiment: A closed cylinder with a locked piston is filled with air. This cylinder is heated. Since the piston cannot move the volume is constant. Temperature and pressure rise. Heating is stopped and the energy added to the system, which is proportional to C_V, is noted. The piston is now freed and moves outwards, expanding without absorbing energy (adiabatic expansion). Doing this work (proportional to C_P) cools the air to below its starting temperature. To return to the starting temperature the air must be heated. This extra heat amounts to about 40% of the previous amount. Thus air has an adiabatic index of approximately 1.4. For a laser produced plasma values in the range of 1.1 – 1.4 have been reported [16].

The gasdynamic equations are:

$$\begin{aligned} &\frac{\partial \rho}{\partial t} + \mathrm{div}(\rho v) = 0 \\ &\frac{\partial v}{\partial t} + (v\nabla)v + \frac{1}{\rho}\nabla p = 0 \\ &\frac{\partial S}{\partial t} + v\nabla S = 0 \end{aligned} \qquad (1.9)$$

where ρ, p, v and S are the density, pressure, velocity and entropy of the gas respectively. It is assumed that the flow parameters are constant on ellipsoidal surfaces and the density and pressure profiles can be written as:

$$\rho(r,t)=\frac{M}{I_1(\gamma)XYZ}\left[1-\frac{x^2}{X^2}-\frac{y^2}{Y^2}-\frac{z^2}{Z^2}\right]^{\alpha}$$
$$p(r,t)=\frac{E}{I_2(\gamma)XYZ}\left[\frac{X_0Y_0Z_0}{XYZ}\right]^{\gamma-1}\left[1-\frac{x^2}{X^2}-\frac{y^2}{Y^2}-\frac{z^2}{Z^2}\right]^{\alpha+1} \tag{1.10}$$

where $M=\int\rho(r,t)dV$ is the mass and $E=(\gamma-1)^{-1}\int p(r,0)dV$ is the initial energy of the vapor cloud. I_1 and I_2 are functions of gamma and are equal to:

$$I_1(\gamma)=\frac{\pi^{\frac{3}{2}}\Gamma(\alpha+1)}{2\Gamma\left(\alpha+\frac{5}{2}\right)}$$
$$I_2(\gamma)=\frac{\pi^{\frac{3}{2}}\Gamma(\alpha+2)}{2(\gamma-1)\Gamma\left(\alpha+\frac{7}{2}\right)} \tag{1.11}$$

where Γ(z) is the Gamma-function. For the pressure and density profiles defined by (1.10) and when the initial vapour cloud is isentropic ($\alpha=1/\gamma-1$), the entropy depends on the coordinates and time as:

$$S=\frac{1}{\gamma-1}\ln\left\{\frac{E}{I_2(\gamma)X_0Y_0Z_0}\left(\frac{I_1(\gamma)X_0Y_0Z_0}{M}\right)^{\gamma}\left[1-\frac{x^2}{X^2}-\frac{y^2}{Y^2}-\frac{z^2}{Z^2}\right]^{\frac{\gamma-2}{\gamma-1}}(\gamma-1)\right\} \tag{1.12}$$

Using (1.10) and (1.11), the gas-dynamic equations can be reduced to a set of ordinary differential equations:

$$\begin{aligned}
\ddot{X} &= -\frac{\partial U}{\partial X} \\
\ddot{Y} &= -\frac{\partial U}{\partial Y} \\
\ddot{Z} &= -\frac{\partial U}{\partial Z} \\
U &= \frac{5\gamma-3}{\gamma-1}\frac{E}{M}\left[\frac{X_0 Y_0 Z_0}{XYZ}\right]^{\gamma-1}
\end{aligned} \tag{1.13}$$

The initial conditions for (1.13) are set as:

$$\begin{aligned}
&X(0) = X_0, Y(0) = Y_0, Z(0) = Z_0 \\
&\dot{X}(0) = \dot{Y}(0) = \dot{Z}(0) = 0
\end{aligned} \tag{1.14}$$

In order to integrate (1.13) numerically, the following dimensionless quantities are introduced, using X_0 as a spatial scale length:

$$\xi\ddot{\xi} = \eta\ddot{\eta} = \zeta\ddot{\zeta} = \left[\frac{\eta_0\zeta_0}{\xi\eta\zeta}\right]^{\gamma-1} \tag{1.15}$$

with initial conditions:

$$\begin{aligned}
&\xi(0) = 1, \eta(0) = \eta_0, \zeta(0) = \zeta_0 \\
&\dot{\xi}(0) = \dot{\eta}(0) = \dot{\zeta}(0) = 0
\end{aligned} \tag{1.16}$$

where:

$$\begin{aligned}
\xi &= \frac{X}{X_0}, \eta = \frac{Y}{X_0}, \zeta = \frac{Z}{X_0} \\
\tau &= \frac{t\beta^{1/2}}{X_0}, \eta_0 = \frac{Y_0}{X_0} \\
\zeta_0 &= \frac{Z_0}{X_0}, \beta = (5\gamma-3)\frac{E_p}{M_p}
\end{aligned} \tag{1.17}$$

Where E_p is the plume energy and M_p is the plume mass. Eqn (1.15) is solved using a fourth order Runge-Kutta-Nyström method. The details of the program and the

mathematical method used can be found in [11]. From (1.10) we can obtain the mass flux in the Z direction:

$$F(z,t) = \rho(x,y,z,t)v_z(x,y,z,t)$$
$$v_z(x,y,z,t) = \frac{z}{Z}\dot{Z} \tag{1.18}$$

The time-of-flight distribution for a plume can be expressed in units of t/t_f:

$$F(\phi,t)\,dt = \frac{M_p k^2}{mI_1(\gamma)z^2}\left(\frac{1+\tan^2\phi}{1+k^2\tan^2\phi}\right)^{3/2} \times \frac{t_f^4}{t^4}\left[1-\frac{t_f^2}{t^2}\right]^{\frac{1}{\gamma-1}}\frac{dt}{t_f} \tag{1.19}$$

t_f is the leading edge arrival time and k is the plume edge ratios. The expression for temperature from the model is:

$$T = \frac{\varepsilon(5\gamma-3)(\gamma-1)}{2\gamma}\left(\frac{X_0Y_0Z_0}{XYZ}\right)^{\gamma-1}\left[1-\left(\frac{z}{Z}\right)^2\right] \tag{1.20}$$

where $\varepsilon = \beta m(5\gamma-1)^{-1}$ is the energy per particle. It can be seen that the model depends on two pure geometric parameters (X_0 and Y_0), which are related to the shape of the laser spot, and a third parameter related to the dimension of the plasma perpendicular to the target surface after the laser pulse has elapsed (Z_0). This parameter depends on the physical properties of the plasma through γ. For a sudden expansion of a gas into vacuum the velocity of the expansion front (v_f) is related to the sound speed through the following expression [11]:

$$v_f = 2(\gamma\text{-}1)^{-1}c_s \tag{1.21}$$

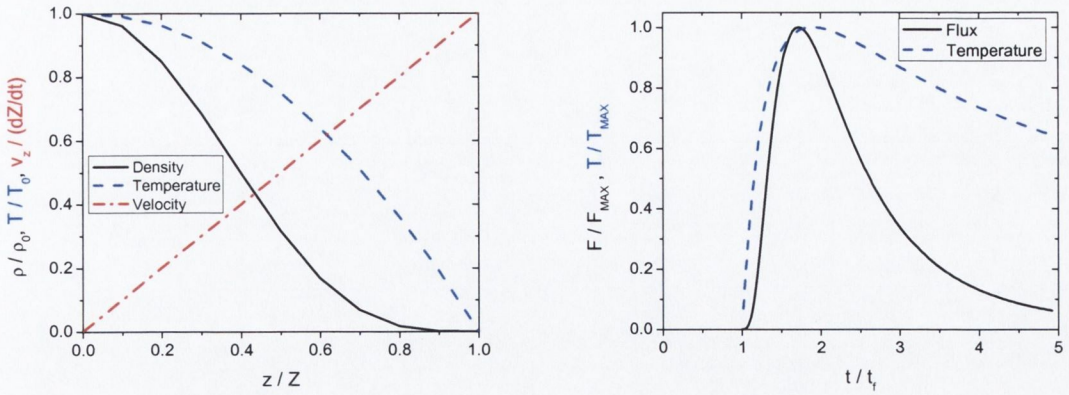

(a) **(b)**

Fig.1.4 (a) The spatial variation of the density, temperature and velocity within the plume. Z is the plume edge and γ was taken as 1.25. **(b)** The flux (1.19) and the temperature (1.20) variation at a distance from the origin. The time is normalised to the front arrival time, t_f.

Fig.1.5 shows the solution for some typical experimental conditions. For these results we took a rectangular spot with the ratios X_0: Y_0: Z_0 = 1: 0.4: 0.13 and γ = 1.25. We can see that at $\tau > 1$, the Y dimension is greater than the X dimension showing the rotation of the semi-axis of the ellipsoid. We can also see that the acceleration phase lasts until $\tau \sim 5$.

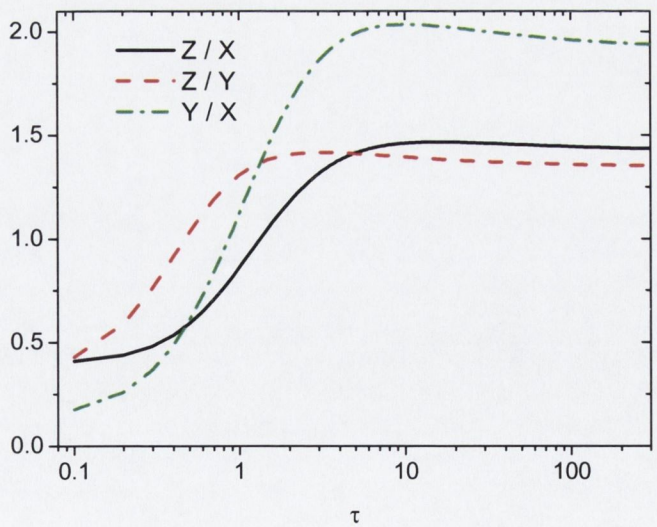

Fig.1.5 The evolution of the plume edge ratios.

The angular dependence of the number of particles arriving per unit area normal to the flow, (ϕ), can be found by integrating (1.18) from the arrival time, t_f, to infinity.
If $t_f >> X_0/\beta^{1/2}$ the analytical expression for $F(\phi)/F(0)$ in the plane x-z will be:

$$\frac{F(\phi)}{F(0)} = \left(\frac{1+\tan^2\phi}{\left(1+(k^2)\tan^2\phi\right)} \right)^{3/2} \tag{1.22}$$

k is the ratio of the plume edges, eg $k_x = Z/X$ and $k_y = Z/Y$, and essentially describes the plume elongation. For example, k = 1 describes a spherical expansion.

Equation (1.22) describes the deposition per unit area on a hemisphere, whereas for a planar surface this is rewritten as:

$$\frac{F(\phi)}{F(0)} = \left(1+(k)^2\tan^2\phi\right)^{-\frac{3}{2}} \tag{1.23}$$

From the Anisimov model the ion flux along the z axis can be written as:

$$I = \frac{N}{I_1(\gamma)} Ak^2 \frac{zv_f}{(v_f t)^4} \left[1 - \frac{z^2}{(v_f t)^2} \right]^{1/\gamma - 1} \tag{1.24}$$

By simplifying this equation, an experimental ion flux signal can be fitted where:

$$I = B \frac{zv_f}{(v_f t)^4} \left[1 - \frac{z^2}{(v_f t)^2} \right]^{1/\gamma - 1} \tag{1.25}$$

The parameter B, depends on the initial parameters and can be let vary to obtain the best fit. z is the distance from the target and v_f is the plasma front velocity. From (1.25), the maximum current occurs when $\frac{dI}{dt} = 0$.

$$\frac{z}{v_f t} = \left(\frac{1}{1 + \lambda/2} \right)^{1/2} \tag{1.26}$$

where λ is $1/\gamma - 1$. For various γ, $\frac{z}{v_f t_{peak}}$ will have the following values:

γ	$z/v_f t_{peak}$
1.1	0.408
1.25	0.577
1.3	0.612

Fig.1.6 shows a typical ion flux signal. The peak time-of-flight, t_{peak}, can be determined accurately hence a value of v_f can be calculated for various γ. Fig.1.6 shows the fits obtained using (1.25) and the above values of γ. The fits indicate that γ falls between 1.1 – 1.3.

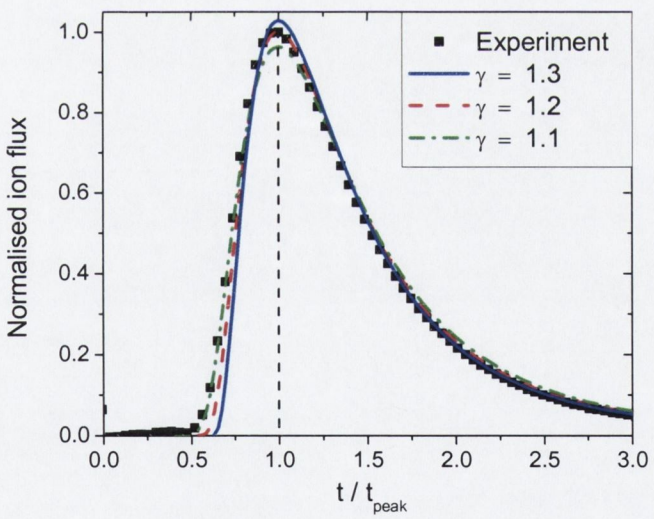

Fig.1.6 An ion flux signal fitted using (1.25) for various γ.

1.3.2 Isothermal plume expansion

The plasma expansion has also been modeled by Singh and Narayan [15], using a uniform temperature, self-similar solution of the gas dynamic equations. In their work the laser-solid interaction is divided into (i) interaction of the beam with the bulk target, and (ii) plasma formation, heating and initial isothermal expansion. After the laser pulse they describe the adiabatic expansion of the plume. From the model the density (n) of the plasma at any point (x, y, z) at time t, can be expressed as a Gaussian function given by:

$$n(x,y,z,t) = \frac{N_T}{2^{1/2}\pi^{3/2}XYZ} \exp\left[-\frac{x^2}{2X^2} - \frac{y^2}{2Y^2} - \frac{z^2}{2Z^2}\right] \tag{1.27}$$

from which the ion flux can be written as:

$$I = \frac{N_T}{2^{1/2}\pi^{3/2}} \frac{k^2}{(v_f t)^4} z v_f A \exp\left[-\frac{z^2}{2(v_f t)^2}\right] \tag{1.28}$$

where N_T is the total number of particles at the end of the laser pulse, A is the probe area, and X, Y and Z are the dimensions of the expanding plasma, and correspond to the distance at which the plasma density decreases to 60.65 % of its maximum. Similar to the previous model we can fit this equation to an experimental signal.

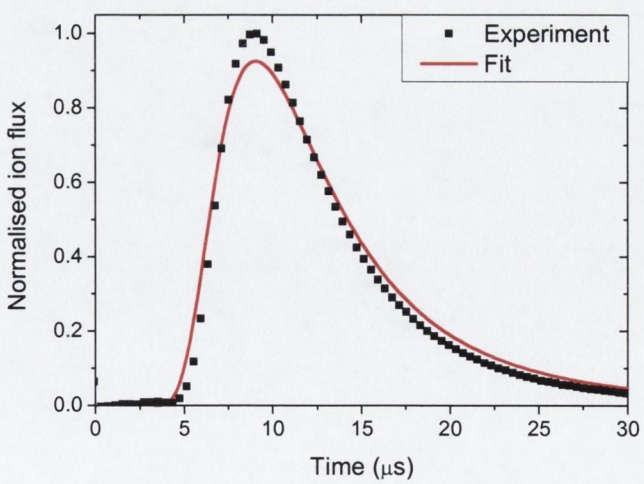

Fig.1.7 Ion signal fitted with Eqn.(1.28)

The Anisimov as well as the Singh and Narayan models have the following differential equations, which describe the propagation of the plume.

$$X(t)\frac{d^2X}{dt^2} = Y(t)\frac{d^2Y}{dt^2} = Z(t)\frac{d^2Z}{dt^2} = A\left[\frac{X_0Y_0Z_0}{XYZ}\right]^{\gamma-1} = \left[\frac{V_0}{V}\right]^{\gamma-1} \qquad (1.29)$$

where $A = (5\gamma - 3)\,{}^{E_p}\!/_{M_p}$ for Anisimov and $A = {}^{k_B T_p}\!/_{m}$ for Singh and Narayan's model.

This equation includes all the plume features observed experimentally such as:

- Strongly peaked in the direction perpendicular to the target surface
- The flip-over effect

The strong peaking of the plume is due to the fact that the acceleration of the front in the Z direction $\left({}^{d^2Z}\!/_{dt^2}\right)$ is proportional to ${}^{1}\!/_{Z}$. Since Z_0 is less than either X_0 or Y_0, the acceleration is much greater away from the target. The flip-over effect will occur because if X_0 is less than Y_0, the plume will have greater acceleration in the X-direction.

The adiabatic expansion models of Anisimov and Singh and Narayan have proved to be very useful for the understanding and interpretation of laser ablation experiments. Both models consider the adiabatic expansion of a small volume of hot gas into vacuum, with the dimensions of the volume of gas chosen to correspond to the dimensions of the vaporised material at the time when evolution and heating of the ablated material is complete. For ns ablation this time corresponds to the end of the laser pulse. The Anisimov model considers the expansion of the plume to be isentropic, which essentially means that there is no heat conduction between parts of the plume. On the other hand the Singh and Narayan model makes the assumption that the plume is isothermal at all times. There is clearly a need to establish which of these extreme constraints is more appropriate [17].

Though the expansion model of Anisimov was developed for the expansion of a neutral gas, it seems to agree with Langmuir probe measurements in ablation plumes [16, 18]. The density gradients in the plasma drive the expansion, which leads to supersonic flow. Since the gradient is greatest normal to the target the acceleration of flow is greatest in the same direction, resulting in the usual forward directed ablation plume. Considering the expression for the electron-ion equipartition, it is clear that the electron-ion collision

rate is sufficient to maintain the equality of temperature between the electrons and ions, i.e $T_e=T_i=T$. Thus the plasma pressure will be:

$$P = n_i(Z+1)kT \tag{1.30}$$

where n_i is the ion density, Z is the mean ion charge, k is the Boltzmann constant and T is the temperature. Since the Debye length is much smaller than the plasma dimension we can ignore the influence of charge separation on the expansion dynamics. Following the analysis of Attwood [19], it can be seen that there are two contributions to the gradient of plasma pressure. The first is due to the ion density gradient:

$$\frac{\partial P_i}{\partial x} = \gamma kT \frac{\partial n_i}{\partial x} \tag{1.31}$$

Secondly the gradient of electron density gives rise to an ambipolar electric field:

$$E = -\frac{1}{en_e}\frac{\partial P_e}{\partial x} = -\frac{1}{en_e}\gamma kT\frac{\partial n_e}{\partial x} \tag{1.32}$$

which of course will act on the ions. The ion momentum equation is given by:

$$m_i n_i\left[\frac{\partial}{\partial t} + v_i\frac{\partial}{\partial x}\right]v_i = -(Z+1)\gamma kT\frac{\partial n_i}{\partial x} \tag{1.33}$$

where γ is the ratio of specific heats. This is the same starting point as used by Anisimov in his analysis of the expansion of a small volume of hot vapour. Thus it is valid to use the models developed by Anisimov and Singh and Narayan to describe the expansion of ionised laser ablation plumes. However the following question remains; is the expansion isentropic or isothermal? Essentially we want to know if electron heat diffusion is sufficiently rapid to keep pace with the plasma expansion. Taking the Spitzer formula [20] for the thermal conductivity of a plasma it can be shown that heat will diffuse a distance s, in time t, given by:

$$s^2 = \frac{9.3\times10^{19}T^{5/2}}{Z(Z+1)n_i}t \tag{1.34}$$

where T is in eV and n_i in cm^{-3}. The rate of plasma expansion is of the same order of the ion sound speed c_s, and in one dimension the length l, of a freely expanding plasma after time t, is approximately:

$$l = c_s t = 9.79\times10^5\left(\frac{\gamma ZT}{M}\right)^{1/2}t \tag{1.35}$$

where M is the atomic weight. For as long as the expression is approximately one-dimensional; $n_i l = n_s d$, where n_s is the atom density in the target and d is the ablation depth. Thus:

$$n_i = \frac{n_s d}{l} \tag{1.36}$$

Substituting for n_i in (1.34) leads to:

$$s^2 = \frac{9.3\times10^{19}T^{5/2}}{Z(Z+1)n_s d}l\,t \tag{1.37}$$

For an isentropic plasma expansion we require that $s < l$, which from (1.35) and (1.37) yields:

$$T^2 < 1.05\times10^{-14}\gamma^{1/2}Z^{3/2}(Z+1)n_s d M^{-1/2} \tag{1.38}$$

Taking $\gamma = 5/3$, Z = 1, d = 10^{-6} cm and for Ag, n_s = 5.86 x 10^{22} cm^3 and M = 108 we get:

$$T < 12.4\,eV \tag{1.39}$$

Thus it would seem that for typical ns ablation conditions the plume expansion may be treated as isentropic if the plasma temperature is less than about 12 eV, which is normally the case [6, 21].

1.4 Conclusions

This chapter set out to describe the laser ablation process and to indicate some typical plasma conditions. The ablation model in section 1.1 enables us to estimate the plasma yield for a range of fluences. For a typical fluence used throughout this of 1.5 J cm^{-2} the model predicts an ablation yield of 7 x 10^{12} particles / pulse. The thickness of the plasma at the end of the pulse is calculated indirectly from an estimate of the initial sound speed in the plume as described in the isentropic model of Anisimov. The thickness was determined to be approximately 50 μm, which gives a density of 5 x 10^{16} particles / cm^3. The ionisation model can then be used to assign a mean ionisation to the plasma. At the end of the laser pulse, the electron temperature can be between 2 – 3 eV. The average ionisation is then predicted to be between 2.5 – 3.5.

The behaviour of the plume has been modelled by Anisimov and can be used to describe the expansion and distribution in vacuum. It provides a description of the ion flux and temperature in terms of the ratio of the specific heat capacities (γ). Fits to some experimental data indicate it lies between 1.1 – 1.3. The sharp edges of the pressure and density profiles at the front at which the density is equal to zero, means that the temperature at the edge approaches zero as well. This is in contrast to Singh and Narayan's model, in which the temperature of the plume is considered constant. Singh and Narayan's model assumes the plume is isothermal, i.e.$\nabla T = 0$, and that the variation of the density is Gaussian throughout the laser irradiation and the subsequent expansion.

1.5 References

1. Miller, J.C. and Haglund, R.F., *Laser ablation and desorption*. Experimental methods in the physical sciences, v.30. 1998, San Diego ; London: Academic.
2. Wang, X.Y., Riffe, D.M., Lee, Y.S., and Downer, M.C., *Physical Review B (Condensed Matter)*, **50**(11): p. 8016(1994).
3. Bogaerts, A., Chen, Z., Gijbels, R., and Vertes, A., *Spectrochimica Acta - Part B Atomic Spectroscopy*, **58**(11): p. 1867(2003).
4. Amoruso, S., *Applied Physics A: Materials Science and Processing*, **69**(3): p. 323(1999).
5. Wellershoff, S.S., Gudde, J., Hohlfeld, J., Muller, J.G., and Matthias, E., *Proceedings of the SPIE - The International Society for Optical Engineering*, **3343**(pt.1-2): p. 378(1998).
6. Lunney, J.G. and Jordan, R., *Applied Surface Science*, **127-129**: p. 941(1998).
7. Carslaw, H.S. and Jaeger, J.C., *Conduction of heat in solids*. 2nd ed. 1986, Oxford: Clarendon.
8. Ready, J.F., *Effects of high-power laser radiation*. 1971, New York ; London: Academic Press.
9. Zel'dovich, I.A.B. and Raizer, I.P., *Physics of shock waves and high-temperature hydrodynamic phenomena*, ed. W.D. Hayes and R.F. Probstein. 1966, New York ; London: Academic P.
10. Lee, R.W., Whitten, B.L., and Stout, R.E., II, *Journal of Quantitative Spectroscopy and Radiative Transfer*, **32**(1): p. 91(1984).
11. Hansen, T.N., *Ion outflow and soft X-ray radiation from a micro capillary discharge source and laser produced prisma*. 2002, Dublin: Trinity College.
12. Itina, T.E., Hermann, J., Delaporte, P., and Sentis, M., *Applied Surface Science*, **208-209**: p. 27(2003).
13. de Posada, E., *The influence of the laser induced plasma in the pulsed laser depositon of ZnO*. 2005, Dublin: Trinity College.
14. Anisimov, S.I., Luk'yanchuk, B.S., and Luches, A., *Applied Surface Science*, **96-98**: p. 24(1996).
15. Singh, R.K. and Narayan, J., *Phys. Rev. B*, **41**(13): p. 8843–8859 (1990).

16. Hansen, T.N., Schou, J., and Lunney, J.G., *Applied Physics A (Materials Science Processing)*, **69**(suppl.): p. 601(1999).

17. Lunney, J.G., Doggett, B., and Kaufman, Y., *Langmuir probe diagnosis of laser ablation plasmas*. Submitted Journal of Physics, Conference series, (COLA '05).

18. Toftmann, B., Schou, J., and Lunney, J.G., *Physical Review B (Condensed Matter and Materials Physics)*, **67**(10): p. 104101(2003).

19. Attwood, D.T., *Soft x-rays and extreme ultraviolet radiation : principles and applications*. 2000, Cambridge: Cambridge University Press.

20. Spitzer, L., *Physics of fully ionized gases*. 2nd revised ed. Tracts on Physics and Astronomy;no.3. 1962: Interscience.

21. Toftmann, B., Schou, J., Hansen, T.N., and Lunney, J.G., *Physical Review Letters*, **84**(17): p. 3998(2000).

2. Experimental Methods

The basic equipment required for plasma production and characterisation has been discussed in detail elsewhere [1]. This chapter only serves to summarise the features of the setup used for the plasma formation and the specifications of the characterisation techniques used throughout this thesis. In general the requirements can be split into two distinct sections. The first consists of the laser, capable of delivering up to a few hundred millijoules per pulse, a vacuum chamber in which the ablation is carried out and a substrate if required where the plasma plume deposits a thin film. The second section includes the various methods and techniques used for the characterisation or monitoring of the deposition process. These can include RHEED and surface reflectivity for analysing thin films, and electrostatic probes, optical absorption / emission spectroscopy and energy analysers for characterising the laser ablation plume.

2.1 Experimental Setup

In this thesis a Lambda Physic KrF (LPX 100, 248 nm, 26 ns pulse width) excimer laser was used for most of the ablation. We used an aperture to select a rectangular part of the beam to minimise hotspots and imaged it onto the target using a 30 cm focal length lens. This results in a final spot of approximately 1 mm x 0.5 mm. The fluence was varied using the focusing lens. The average energy per pulse was measured inside the chamber using a Scientech thermopile joulemeter, which was calibrated against a known electrical power input yielding a sensitivity of 96 mV W^{-1}.

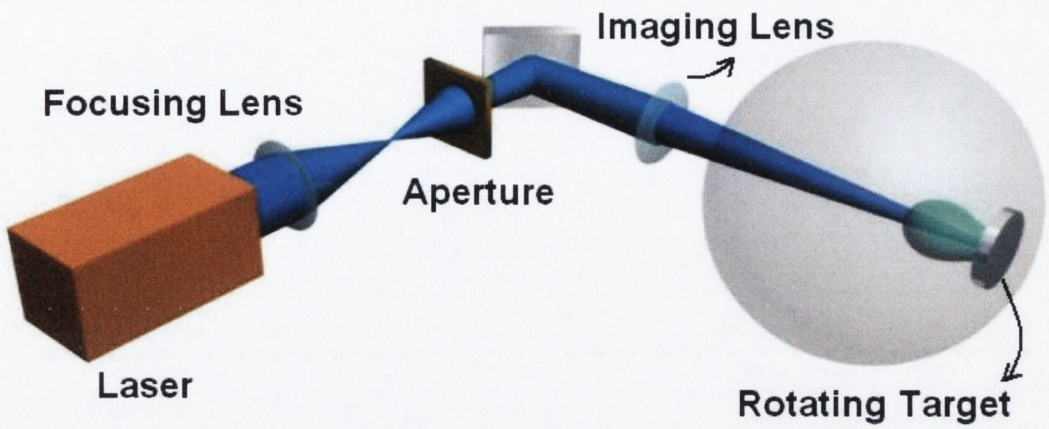

Fig.2.1 A Schematic of the laser ablation setup.

The work was carried out in a stainless steel barrel chamber (15 litres) with an obtainable base pressure of 5×10^{-6} mbar (with baking) using a Pfeiffer-Balzers TSH 050 turbo molecular system (50 l s^{-1}). A Balzers Penning gauge was used for the 10^{-5} to10^{-3} mbar regime. For the region of 0.2-1 mbar an Edwards Pirani gauge was used. The latter was calibrated using a Hastings HPM-2002-OBE wide range gauge, which consists of a dual sensor unit containing a piezoresistive direct force sensor and a thin film Pirani type sensor.

2.2 Plasma characterisation techniques

2.2.1 Langmuir probe

The technique of using an electrostatic probe to measure the properties of a plasma was introduced in 1923 by Langmuir [2]. The theory was presented for steady and collisionless plasmas in which the electron energy distribution function (EEDF) is Maxwellian. In general the basis of the theory and the experimental set up are relatively simple. The electric probe is a conducting object inserted into the plasma and is connected outside the chamber to some circuit. Probe theory creates a connection between the measured probe currents or voltages and the parameters of the undisturbed plasma. However, in contrast to the simple operation of probes the theoretical interpretation of the results remains complicated. The use of electrostatic probes in a flowing plasma was further developed by Koopman [3].

Fig.2.2(a) shows a schematic of the typical Koopman bias circuit used for a flowing plasma. The operating principle of a Langmuir probe at first glance is very simple. The electrical circuit allows variation of the probe voltage, V, with respect to the plasma and to measure the current voltage characteristic I(V). Generally a few guidelines need to be followed when deciding on the components for the circuit.

1. The total collected integrated charge in a pulse must be much less than that stored in the blocking capacitor (C_B).
2. The voltage measured over the load resistor (R_L) should be much less than the bias voltage (V_B) applied to the probe at all times.

For example, the RC time ($R = R_c = 22\ k\Omega$, $\therefore RC = 14$ ms), restricts the rate at which the experiment can be carried out. Once the capacitor is charged only transient currents from the plasma are allowed.

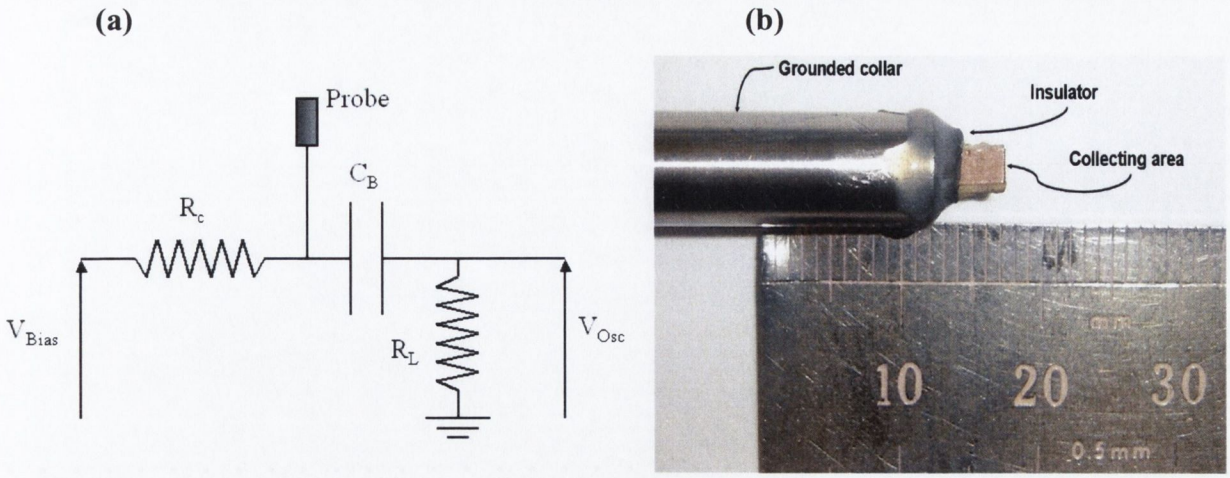

Fig.2.2 (a) A RC 'Koopman' circuit for flowing plasmas. The bias voltage (V_B) could be varied between ± 30 V and the load resistor (R_L) could be varied to keep V_{Osc} to a minimum. The blocking capacitor (C_B) remained fixed at 0.65 μF. **(b)** An example of a planar probe which has dimensions 3 x 2 mm.

Throughout the experiments a small planar probe with dimensions 4.5 x 2 mm^2 was positioned 10 cm from the target. Its purpose was to ensure reproducibility of the ablation plume and was orientated to face the target. It was biased at -30 V to record the ion signal due to the plasma flow, and by maintaining a constant ion flux to this probe using the focusing lens, any variation in laser energy and ablation rate could be corrected. For probe experiments a second probe of typically 5 x 5 mm^2 was used. This probe was positioned close to the target normal and could be rotated around its axis so as to change its orientation relative to the plasma flow. For both probes, the current was determined by using a digital oscilloscope to measure the voltage across a load resistor and was averaged over 10 laser shots.

2.2.2 Energy Selective-Time of Flight Mass Spectrometer

Throughout this work we will show how Langmuir probes can be used to measure the plasma density and temperature, the plasma flow velocity and the shape of the ablation plume expansion. However one clear disadvantage of these probes is their inability to distinguish between different ion species and charge states. An energy spectrometer is a useful addition to the Langmuir probe in determining the plasma parameters. Many principles have been used to achieve energy analysis of charged particles such as the measurement of the time of flight, the retardation by a potential barrier and the dispersion in a deflecting field.

In this work the Energy Selective – Time of Flight Mass Spectrometer (ES-TOFMS), achieves mass separation of ions by accelerating them in a constant electric field. Since the kinetic energy is the same for all ions of equal charge those of lower mass reach a higher velocity and arrive at the detector earlier. To date most energy analysers use micro-channel plates (MCP) as detectors, however we used cylindrical wires coupled through an operational amplifier to detect the ionic current. We will be particularly interested in identifying the charge state of the species and the energy distribution of ions from single and multi component targets. Fig.2.3 shows a schematic of the Energy Selective-Time of Flight Mass Spectrometer (ES-TOFMS). It consists of an entrance slit of typically tens of microns, two curved parallel electrodes of radii R_1 and R_2, and a wire detector. The plates are biased with equal and opposite voltages using a dual output power supply capable of delivering up to 32 V.

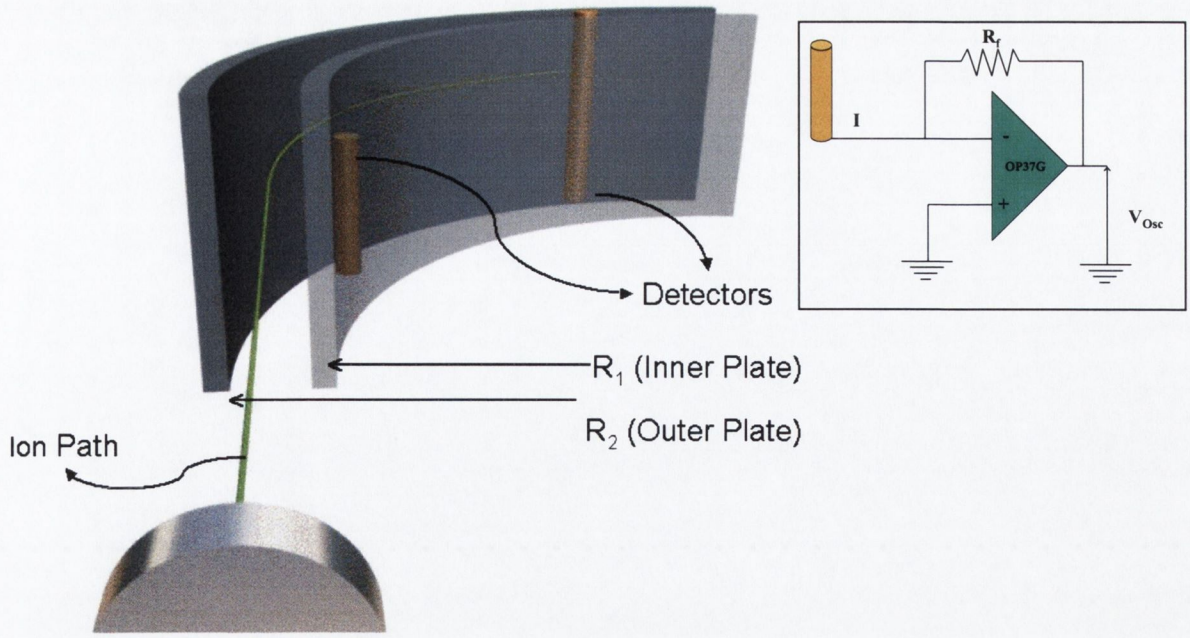

Fig.2.3 The ES-TOFMS, with the ion trajectory and detectors. The inset shows the circuit used to measure the current collected.

When a voltage is applied to the plates and an electric field established, the spectrometer acts as an energy filter, allowing only ions with certain energies to reach the detector. The pass energy of the spectrometer is given by:

$$E_{\text{Filter}} = \frac{Z\Delta V R_0}{2d} \tag{2.1}$$

where Z is the ion charge, ΔV is the voltage applied between the plates, R_0 is the centreline radius of curvature and d is the plate separation. By choosing suitable values of R_0 and d we can determine the energy range of the spectrometer. We selected R_0 = 3.5 cm and d = 3.25 mm which gives the analyser an energy range of $0-350$ eV assuming Z = 1. The device was isolated inside a grounded aluminium box, (7 x 10 x 2 cm), with a 1 cm diameter entrance to mount the entrance slit (3 mm x 50 μm). It was situated along the target normal at a distance of 29 cm with all electrical connections made through grounded BNC connectors. The charge collected by the detector was determined using an operational amplifier operating in inverting mode with a feedback resistor (R_f) of 220 kΩ.

One limitation of the device is that low energy ions cannot be reliably detected due to space charge effects at low transmission energies. The space charge causes shifts in the positions of the peaks and corresponding errors in determining their TOF. Its magnitude can be determined as:

$$E_{space} = \frac{wn_i e}{2\varepsilon_0} \tag{2.2}$$

where w is the slit width and n_i is the ion density at the slit. For a slit of 50 μm and a typical ion density of 10^{10} cm^{-3} at 29 cm then $E_{space} \sim 4000$ V m^{-1}.

Only ions with the same energy, $\left(E_{ion} = \frac{m_i v_i^2}{2e} \right)$, as the pass energy of the spectrometer will travel the length of the analyser to reach the detector. The output of the analyser then gives the time of flight and hence the velocity of the ions. The mass-to-charge ratio is then determined by balancing both energy equations:

$$\frac{m}{Z} = \frac{e\Delta V R_0}{dv_i^2} \tag{2.3}$$

Resolution

As the energy is determined using (2.1), the associated error can be calculated as:

$$\Delta E_{filter} = \frac{\Delta R}{R} E_{filter} \tag{2.4}$$

Taking $\Delta R = 3$ mm (the diameter of the wire detector) and $R = R_0$, then $\Delta E_{filter} = 0.09 E_{filter}$. It is also possible to estimate the error in the TOF from:

$$\frac{\Delta E_{filter}}{E_{filter}} = \frac{\Delta R}{R} = \frac{2\Delta v}{v} = \frac{-2\Delta t}{t}$$
$$\therefore \Delta t = \frac{t}{2}\frac{\Delta R}{R} \tag{2.5}$$

2.3 Estimated errors

The following tables summarise the errors for some of the frequently used quantities.

Quantity	Symbol	Units	Error
Probe distance	D	cm	0.2 cm
Laser spot dimensions	x, y	mm	0.1 mm
Powermeter voltage	V	mV	5 mV
Time of flight	t_{tof}	μs	0.05 μs

	Definition	Explicit error	Approx
Fluence	$F = \frac{E}{A}$	$F \times \left(\frac{\Delta E}{E} + \frac{\Delta A}{A} = \frac{\Delta V}{V} + \frac{\Delta x}{x} + \frac{\Delta y}{y} \right)$	0.3F
Time of flight	$v_{tof} = \frac{d}{t_{tof}}$	$v_{tof} \times \left(\frac{\Delta d}{d} + \frac{\Delta t_{tof}}{t_{tof}} \right)$	$0.15 v_{tof}$
Ion energy	$E_{ion} = \frac{1}{2} m_i v_{tof}^2$	$E_{ion} \times \frac{2\Delta v_{tof}}{v_{tof}}$	$0.2 E_{ion}$
Ion flux	$F = \frac{1}{RAe} \int^{t} V(t) dt$	$F \times \left(\frac{\Delta R}{R} + \frac{\Delta A}{A} \right)$	0.2F

2.4 References

1. Chrisey, D.B. and Hubler, G.K., *Pulsed laser deposition of thin films*. 1994, New York ; Chichester: J. Wiley.
2. Langmuir, I. and Mott-Smith, H.M., *Gem. Electr. Rev.*, **26**: p. 731(1923).
3. Koopman, D.W., *Physics of Fluids*, **14**(8): p. 1707(1971).

3. Langmuir Probe

The full characterisation of a plasma plume requires many different techniques, each giving information about a particular aspect. Diagnostics of plasmas can generally be divided into two main categories: active non-contact methods, such as optical spectroscopy, and contact methods, such as energy analysers and electrostatic probes. In this thesis we restrict ourselves primarily to the electrostatic probe. It was one of the first techniques for measuring the properties of a plasma, and has proved itself to be a versatile and robust device. The subject of electric probes in plasmas is immense with thousands of references in the literature.

Electric probes come in all sizes and shapes, but the more common are spheres, cylinders and flat discs. They are usually made out of materials like molybdenum, tungsten or graphite and the holders can be made from glass, quartz or ceramic materials. Some general requirements must be satisfied before using the probes. These include that the probe tip must be able to withstand the heat load from the plasma and that the probe should not perturb the overall state of the plasma. The first requires a small probe size compared with the typical plasma scale lengths. The second is not as easy to satisfy. The perturbation of the plasma occurs primarily through changes of the electric potential and hence the particle density and energy. The perturbation depends on the potential of the probe and the current drawn by it. Therefore a good understanding of the perturbative effects of the probe is important before interpreting the results.

In this chapter we shall discuss the probe-plasma interaction, the relevant probe theories and some parameters such as density and temperature obtained using electrostatic probes.

3.1 Plasma equilibrium

Various collisional and radiative processes between charged and neutral particles take place within the plasma, with their relative importance depending upon the density, temperature and degree of ionisation. There are two basic ionisation processes: impact ionisation, where an electron strikes an atom resulting in an ion and two electrons; and radiative ionisation where a photon with sufficient energy is absorbed by an atom, dissociating it into an ion and an electron. Recombination processes are the reverse of the ionisation processes and are: three-body recombination, where two electrons and an ion join to make an atom and free electron; and radiative recombination, where an electron and ion combine into an atom with the release of a photon. All these rates depend on the electron temperature and density.

Different plasma equilibrium models assume different relative strengths of these various processes. For example, in low-density ($< 10^8$ cm^{-3}) plasmas, radiative recombination is larger than three-body recombination and the model of 'coronal equilibrium' can be used. In this case impact ionisation and radiative recombination are in balance. At high densities, ($> 10^{16}$ cm^{-3}) the 'Local Thermal Equilibrium' model is applicable and the atom, ion and electron densities will be described by the Saha-Boltzman model. The collisional processes within a plasma are discussed in detail in [1] so we shall just present the relevant equations here.

If we have a density, n_n, of neutral atoms with a cross sectional area, σ, then an electron will travel a distance $1/n_n\sigma$ before it has a reasonable probability of colliding with an atom. This quantity is called the mean-free path for collisions, λ_{mfp}, and for electrons of velocity, v_e, the mean time between collisions is given by $\tau = \lambda_{mfp}/v_e$.

The collisional frequency is usually defined in terms of an average over all velocities in the Maxwellian distribution and is written as:

$$\nu = \left\langle \tau^{-1} \right\rangle = n_n \left\langle \sigma v \right\rangle \tag{3.1}$$

For a hydrogen atom, the Bohr radius is given by $a_0 \approx 5\times10^{-11}$ m. The cross-section for elastic scattering of an electron by a neutral atom can then be estimated roughly as:

$$\sigma_n \sim \pi a_0^2 \sim 10^{-20} \text{ m}^2 \tag{3.2}$$

At a distance a_0 from a neutral atom an incoming electron has a substantial chance of undergoing a collision. However when an electron approaches an ion it will experience an attractive Coulomb force, which deflects the electron trajectory towards the ion. The interaction with the Coulomb force of another charged particle is essentially the same as a 'collision'. We then define an effective 'Coulomb cross-section' of the ion in terms of the distance of closest approach 'b' of the electron to the ion:

$$\sigma_i \sim \pi b^2 \sim \frac{\pi e^4}{\left(4\pi\varepsilon_0\right)^2 T_e^2} \sim \frac{10^{-17}}{T_e^2} \text{ m}^2 \tag{3.3}$$

where T_e is given in eV. If we compare the two cross sections we see that Coulomb collisions will dominate over collisions with neutrals in any plasma that is just a few percent ionised. Only if the ionisation level is very small can neutral collisions dominate.

The effective Coulomb cross-section is actually considerably larger than the estimate above because of the long-range nature of the Coulomb force. In practise, small-angle collisions are much more frequent than large-angle collisions with the cumulative effect of the many small-angle collisions turning out to be larger than the relatively fewer large-angle collisions.

The electron-ion collision rate is defined by:

$$\begin{aligned} \nu_{ei} &= 4\pi n v_e b_0^2 \ln\Lambda \\ &= \frac{n_i Z^2 e^4 \ln\Lambda}{4\pi\varepsilon_0^2 m_e^{\,2} v_e^{\,3}} \end{aligned} \tag{3.4}$$

where $\Lambda = b_{max}/b_0$. b_0 is the impact parameter for scattering through 90°, and b_{max} is the maximum impact parameter [1]. In a plasma electrons will gather near a positive charge and will tend to screen out the electric field from the charge preventing it from penetrating into the plasma. The distance over which the field is shielded is one of the main characteristic length scales in a plasma and is called the Debye length, λ_D:

$$\lambda_D = \sqrt{\frac{\varepsilon_0 T_e}{e^2 n_e}} \tag{3.5}$$

where ε_0 is the permittivity in vacuum. The Debye shielding gives rise to an exponential decrease in the electric potential for distances greater than the Debye length. As a result the maximum impact parameter, b_{max} is taken to be λ_D. Therefore:

$$\begin{aligned} \Lambda &\sim \frac{b_{max}}{b_0} \sim \frac{\lambda_D}{b_0} \\ b_0 &\sim \frac{Ze^2}{12\pi\varepsilon_0 T} \sim \left(\frac{Z}{12\pi}\right)\left(\frac{1}{n\lambda_D^2}\right) \end{aligned} \tag{3.6}$$

The average electron-ion collision rate is then defined as:

$$\langle \nu_{ei} \rangle = \frac{2^{1/2} n_i Z^2 e^4 \ln\Lambda}{12\pi^{3/2}\varepsilon_0^2 m_e^{1/2} T_e^{3/2}} \tag{3.7}$$

In the case of electron-electron collisions, it is a little more difficult to analyse, as the scattering particle can no longer be taken as fixed. However, as the Coulomb force has the same magnitude and the electron will be deflected by the same amount, an approximation can be taken as:

$$\langle \nu_{ee} \rangle \approx \frac{n_e e^4 \ln\Lambda}{\varepsilon_0^2 m_e^{1/2} T_e^{3/2}} \approx \frac{\langle \nu_{ei} \rangle}{n_i Z^2 / n_e} \tag{3.8}$$

Ions make Coulomb-collisions with other ions and electrons, with the average ion-ion collision frequency defined by:

$$\langle \nu_{ii} \rangle = \frac{n_i Z^4 e^4 \ln\Lambda}{12\pi^{3/2}\varepsilon_0^2 m_i^{1/2} T_i^{3/2}} \tag{3.9}$$

The ratio of the mean time between collisions, $\tau = 1/\nu$, for the charged particles is then:

$$\tau_{ee} : \tau_{ei} : \tau_{ii}$$
$$1 : \frac{47 n_e}{n_i Z^2} : \frac{n_e}{n_i}\left(\frac{m_i}{m_e}\right)^{1/2}\left(\frac{T_i}{T_e}\right)^{3/2}\frac{12\pi^{3/2}}{Z^4} \tag{3.10}$$

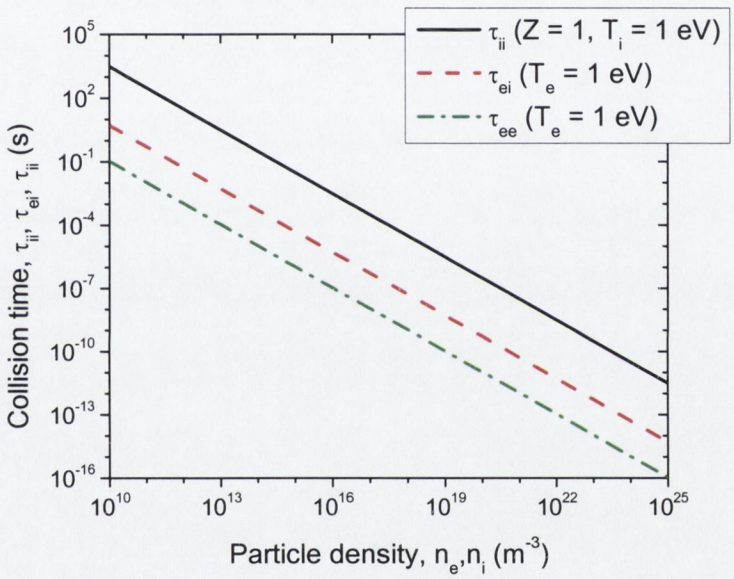

Fig.3.1 Collision times in a fully ionised plasma with a Maxwellian electron distribution. The factor $\ln\Lambda$ is taken from Phipps to be 7 [2].

Fig.3.1 shows the scaling of the collision times with particle density for an electron and ion temperature of 1 eV. From these results we see that the collision times for a typical plasma density at the end of the laser pulse of 10^{23} m^{-3}, are less than the typical time of the plasma evolution (10^{-9} s) studied in this thesis with:

$$\tau_{ii} : \tau_{ei} : \tau_{ee} = 3 \times 10^{-10} : 6 \times 10^{-13} : 1 \times 10^{-14} \text{ s}.$$

From (3.9), the ion-ion collision time is inversely proportional to Z^4 and proportional to $T_i^{3/2}$. If we take for comparison an ionisation of $Z = 2$ and an ion temperature of $T_i = 0.1$ eV then τ_{ii} reduces to 10^{-13} s from 10^{-10} s for a density of 10^{23} m^{-3}.

3.2 Probe Regime

The application of probe theories describing these plasmas is rather complex and has been developed for specific cases such as planar, cylindrical or spherical probe geometries [3]. There are also different regimes of probe operation in which only certain theories apply. The different regimes are defined by the plasma and probe features such as the mean free path between electron and ion collisions ($\lambda_{mfp,e,i}$), energy relaxation length (λ_{relx}) (also described using the equilibration time between electrons and ions, τ_{eiE}), characteristic probe dimension (d_{probe}) and sheath thickness (h). The main regimes can be identified as follows:

- Collisionless: $\lambda_{mfp} >> d_{probe} + h$
- Nonlocal: $\lambda_{relx} >> d_{probe} + h >> \lambda_{mfp}$
- Hydrodynamic: $d_{probe} + h >> \lambda_{relx}$

Furthermore each of the above regimes can be further divided into different subregimes [4]. In order to decide which plasma theory to use, we must first determine which plasma regime we are operating in. At the end of the laser pulse the plasma has a typical density of 10^{25} m^{-3} and a temperature of a few eV [5, 6]. For the following estimates we take T = 4 eV. The cross section for elastic scattering of an electron by a neutral atom can then be estimated as roughly ~ 10^{-20} m^2. The mean free path, $(1/n\sigma)$, for electron-neutral collisions is then ~ 10 μm. For ions the Coulomb cross section is approximately $10^{-17}/T_e(eV)^2 \sim 6 \times 10^{-19}$ m^2. The mean free path between electron-ion collisions is then ~ 0.2 μm. (If we take into account multiple small angle collisions the mean free path will become even smaller). It is clear however, that Coulomb collisions will dominate over collisions with neutrals.

Taking $n = n_i = n_e$, $T = T_e = T_i$ and $Z = 4$, the time between charged-particle collisions can be determined using (3.7) - (3.9) as:

$$\tau_{ii} : \tau_{ei} : \tau_{ee} = 3.2 \text{ ps}: 4.4 \text{ fs} : 0.84 \text{ fs} \tag{3.11}$$

The time an electron needs to lose its energy in collisional processes is called the energy relaxation time or equilibration time, τ_{eiE}. If electron-electron collisions are dominant this requires only one collision and the energy relaxation length, $\lambda_{relx,}$ corresponds to the mean free path. The electron – ion energy transfer time or equilibration time is defined as:

$$\tau_{eiE} = \frac{3\pi(2\pi)^{1/2}\varepsilon_0^2 m_i T_e^{3/2}}{n_e Z^2 e^4 m_e^{1/2} \ln\Lambda} \approx \frac{m_i}{2m_e}\tau_{ei} \approx 0.5 \text{ ns} \tag{3.12}$$

Thus it is valid to assume that $T = T_e = T_i$. The density in the plume at a typical probe distance of ~ 5 cm is between 10^{15} to 10^{18} m^{-3}. Taking $n = 10^{16}$ m^{-3}, $T = 1$ eV and $Z = 2$;

$$\tau_{ii} : \tau_{ei} : \tau_{ee} = 2 \text{ ms}: 1.2 \text{ μs} : 104 \text{ ns} \tag{3.13}$$

Taking an electron thermal velocity of 10^5 ms^{-1} ($T_e = 4$ eV) and an average ion velocity of 10^4 m s^{-1} the mean free paths ($\lambda = v\tau$) are estimated as:

$$\begin{aligned} \lambda_{ii} &= v_i \tau_{ii} = 20 \text{ m} \\ \lambda_{ee} &= v_e \tau_{ee} = 7 \text{ cm} \\ \lambda_{ei} &= v_e \tau_{ei} = 79 \text{ cm} \end{aligned} \tag{3.14}$$

As was mentioned in the previous section, probably the most fundamental length scale in plasma science is the Debye length.

$$\lambda_D = \sqrt{\frac{\varepsilon_0 T_e}{e^2 n_0}} \tag{3.15}$$

For a distance larger than the Debye length, the plasma will tend to remain neutral. For a density of 10^{16} m^{-3} and an electron temperature range $T_e = 0.1 - 1$ eV, the Debye length could vary from 24 – 74 μm. The characteristic probe dimension, d, for a disk probe is given by $d \approx \pi R/4$ [7], where R is the probe radius. For a typical probe where R can be between 1 – 5 mm, d can vary between 0.8 – 4 mm.

An initial estimate of the sheath thickness, h, can be calculated using the simplest high-voltage sheath with a uniform ion density known as a matrix sheath [8]. It is defined as: $h = \sqrt{2\varepsilon_0 V / en_i}$. For a bias voltage of 30 V and an ion density of 10^{16} m^{-3}, h = 0.6 mm.

From a comparison of these scale lengths we are in a position to say that: $\lambda_{mfp,e,i} \gg d + h \gg \lambda_D$. Under these conditions, a collisionless sheath theory can be used to interpret the Langmuir probe characteristics.

3.3 Probe theory

An image of a typical planar probe used in this work was shown in the previous chapter. It is introduced in the plasma and biased with respect to ground. The bias voltage is swept from negative to positive voltages allowing for the measurement of ions or electrons respectively. Due to charge neutrality in the plasma, the probe potential will only affect the electrons located a few Debye lengths from the probe. This region is called the sheath. Both theory and experiment show [9] that at negative voltages, high enough to prevent the electrons with the highest thermal energies in the plasma from reaching the probe, the detected ionic current saturates. This current is proportional to the density of ions (n_i) in the plasma through the following expression:

$$I_{ion} = ev_i An_i \tag{3.16}$$

where e is the electron charge, v_i is the flow velocity of the ions and A is the collecting area of the probe. The above equation assumes the presence of singly ionised species. By moving the bias voltage toward positive values, ion repulsion takes place and the current due to electrons increases.

At a certain bias the current due to the ions and electrons are equal and so the measured current is zero. This bias corresponds to the floating potential V_f. For bias voltages greater than V_f the current is related to the electron energy distribution function (EEDF). For a Maxwellian distribution the measured electron current is defined as:

$$I = I_{e,sat} \exp\left(\frac{V_{bias} - V_p}{kT_e}\right) \tag{3.17}$$

where V_p is the plasma potential, T_e is the electron temperature and $I_{e,sat}$ is the saturation electron current [4]. The saturation electron current region is reached with further increase in voltage to values greater than the plasma potential.

The measured current will be proportional to the density of electrons (n_e) and the average thermal velocity in the plasma (v_e), and is defined as:

$$I_{e,sat} = \frac{1}{4} e v_e A n_e \tag{3.18}$$

v_e is the thermal velocity given by $\left(\frac{8kT_e}{\pi m_e}\right)^{1/2}$. From (3.17) kT_e can be readily found from a $\frac{d\ln(I)}{dV}$ plot of the electron-retarding region. As was mentioned before, this is possible only if the EEDF is Maxwellian. More general methods exist that allow the determination of the EEDF from the measured I-V curve. Druyvesteyn [10] demonstrated the proportionality between the EEDF and the second derivative of the electron current with respect to the probe potential. If F(E) is the EEDF, the plasma parameters such as electron density and average electron energy can be obtained as follows:

$$\begin{aligned} n_e &= \int_0^\infty F(E)dE \\ \langle E \rangle &= \frac{1}{n_e} \int_0^\infty E \quad F(E)dE \end{aligned} \tag{3.19}$$

When the first derivative of the I-V characteristic goes through a maximum, the current and voltage at which this occurs and the value of the derivative itself can be used to determine the electron temperature and the plasma potential.

An example of ion time-of-flight (TOF) signals obtained from a planar Langmuir probe for various bias voltages is shown in Fig.3.2(a). The probe distance was 6.5 cm and the plasma was produced by the ablation of silver at a fluence of 1 J cm^{-2}. The TOF signal is characterised by a sudden rise, which relates to the arrival of the plasma front to the probe. It reaches a maximum that indicates the ion velocity corresponding to the maximum ion flux and then falls slowly to return to the zero value. At this point the plasma has moved past the probe. If at a specific time the value of the current is plotted versus the applied voltage the IV characteristic is obtained. Fig.3.2(b) shows the IV characteristic obtained for a TOF of 7 μs.

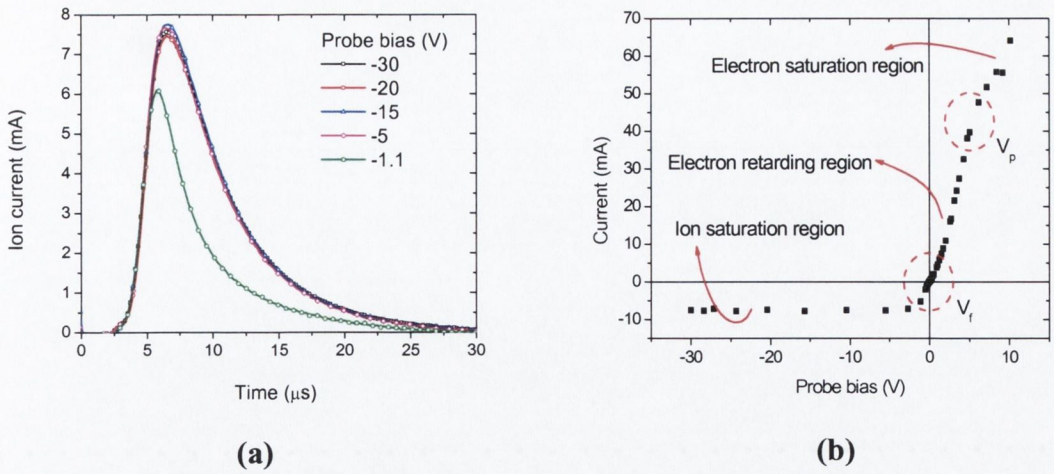

(a) **(b)**

Fig.3.2 (a) Ion TOF signals for different bias voltages are shown, during the ablation of silver at a fluence of 1 Jcm^{-2}. The probe distance was 6.5 cm. **(b)** An IV characteristic obtained at the peak TOF of 7 μs.

The expansion dynamics of the plume can be monitored quite accurately with a Langmuir probe. If the probe is biased sufficiently negative so as to repel all electrons it will detect a pulse of ion current due to the flow of the plasma past its position. The flow velocity of the ions can be initially estimated from the TOF measured by the probe ($v_i = z/t$), while the kinetic energy associated with a particular time is simply $\frac{1}{2} m_i v_i^2$. However these equations do not take into account the plasma formation and acceleration time. We discuss this problem in more detail in section 3.7.

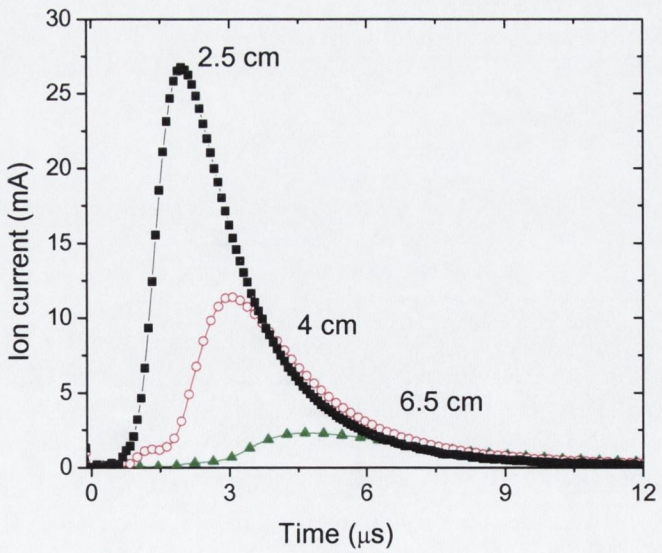

Fig.3.3 Ion TOF signals for various target-probe distances.

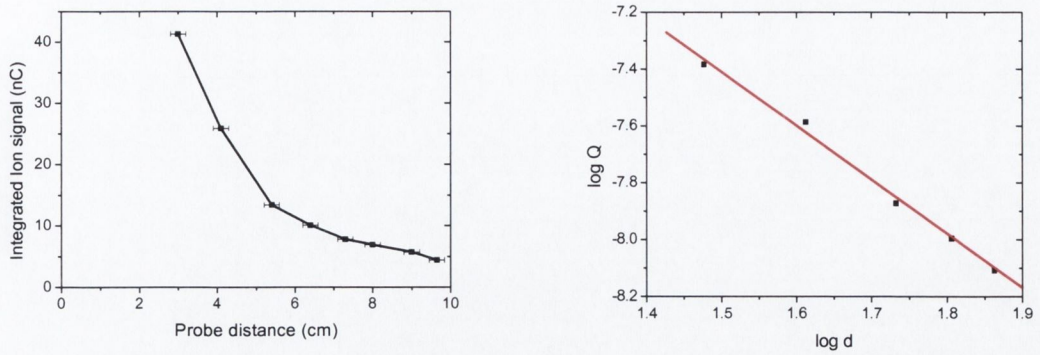

(a) **(b)**

Fig.3.4 (a) The integrated ion flux vs. distance from a silver target during ablation in vacuum at 1 J cm^{-2}. **(b)** A log-log plot of the data.

Fig.3.3 shows how the TOF signal varies with distance. The variation with distance of the integrated ion flux in vacuum is shown in Fig.3.4(a). The log-log plot on the right shows that the ion flux reduces as approximately $1/d^2$, the slope being –1.9. This indicates that little recombination occurs.

3.4 Probe Perturbation

Before carrying out any experiments we need to look at the probe itself and whether any perturbation of the plasma occurs. To estimate whether the probe was perturbing the plasma a method developed by Waymouth [11] can be used. Waymouth states that, if the drain of electron current is sufficiently large in relation to the processes replenishing the high energy "tail" of the electron-energy distribution, the shape of the distribution will be perturbed by the act of measurement and hence any deductions made from the shape of the I-V characteristic would be incorrect. His work essentially compares the time constant with which a given probe will deplete (depletion time) a given plasma of electrons of a particular velocity, with the time constant required to replenish (replenishment time) a Maxwellian "tail" with electrons of a particular velocity. This replenishment time comes from the "self-collision time", defined by Spitzer [12] as the time constant with which an originally non-Maxwellian distribution approaches a Maxwellian by Coulomb collisions only. We summarise the calculations here.

For an isotropic distribution of electron velocities, the particle current of electrons of velocity v, which flows to the probe is given by:

$$\Gamma(v) = n(v)\frac{1}{4}vA\left[1-\left(\frac{v_0}{v}\right)^2\right] \tag{3.20}$$

where v_0 is the critical velocity that electrons have to overcome to reach the probe, which is defined by the bias voltage and A is the area of the probe. If $N_e(v)$ is the total number of electrons with velocity v in the plasma then,

$$n(v) = \frac{N_e(v)}{V} \tag{3.21}$$

where V is the volume of the plasma. The time rate of change of $N_e(v)$ resulting from the loss of electrons of velocity v to the probe is:

$$\frac{dN_e(v)}{dt} = -\Gamma(v)$$

$$\frac{dN_e(v)}{dt} = \frac{N_e(v)}{V}\frac{v}{4}A\left[1-\left(\frac{v_0}{v}\right)^2\right] \tag{3.22}$$

$$N_e(v) = N_0(v)\exp\left(-\frac{t}{\tau_d}\right)$$

where τ_d is the depletion time given by:

$$\tau_d = \frac{4V}{Av}\left[\frac{1}{1-\left(v_0/v\right)^2}\right] \tag{3.23}$$

τ_d becomes infinitely long for electrons of velocity v_0, but for electrons with $v>>v_0$ it approaches a limiting value:

$$\tau_d = \frac{4V}{Av} \tag{3.24}$$

At this point Waymouth discusses the issue of which is the proper value of time constant to use in the criterion and selects a time constant (τ_d), such that half of the electron current drawn by a probe at the potential $-mv_0^2/2e$, is characterised by a depletion time constant shorter than τ_d. The electron current drawn by a probe biased at $-mv_0^2/2e$, from a Maxwellian plasma is proportional to $\exp\left(-mv_0^2/2kT_e\right)$. Half of the total electron current drawn by the probe at this potential is due to electrons with velocity greater than v where:

$$\frac{\exp\left(-mv^2/2kT_e\right)}{\exp\left(-mv_0^2/2kT_e\right)} = \frac{1}{2}$$

$$v_0^2 - v^2 = \frac{2kT_e}{m}\ln(0.5) \tag{3.25}$$

$$\left(1-\frac{v_0^2}{v^2}\right) = -1.38\left(\frac{kT_e}{mv^2}\right)$$

Therefore half the electron current drawn by the probe is characterised by a depletion time constant shorter than:

$$\tau_d = \left(\frac{2.9V}{Av}\right)\frac{mv^2}{kT_e} \tag{3.26}$$

Then comparing equation (3.26) with the replenishment time constant τ_r :

$$\tau_r = \frac{m^2v^3}{8\pi n_e e^4} \tag{3.27}$$

with the condition that $\tau_d >> \tau_r$ and using equation (3.21), the condition for the absence of a depletion effect becomes a determination of the minimum number of electrons in the plasma:

$$N_e >> 1.5x10^4 T_e^2 A \tag{3.28}$$

T_e is the electron temperature in degrees Kelvin, A is the area of the probe in cm^2 and N_e is the total number of electrons. In other words (3.28) gives the maximum number of electrons that can be drained by a probe of a given area from a plasma at a given temperature. In the last step it was assumed that the maximum electron velocity obtained in any experiment will be given by: $\frac{mv^2}{2} = 10\left(\frac{3kT_e}{2}\right)$.

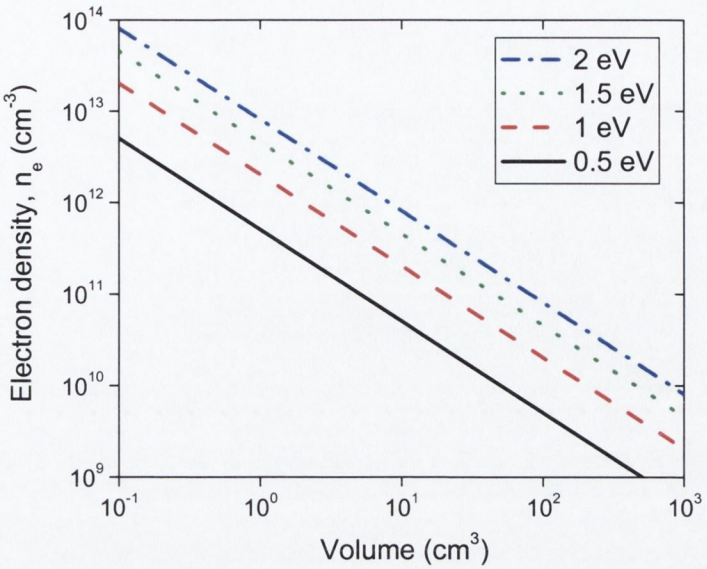

Fig.3.5 Plots of $N = n_e V = 1.5 \times 10^4 T_e^2 A$ for various temperatures and a probe with an area of 1 cm^2.

For a plasma produced by laser ablation of silver at a fluence of 1.5 J cm^{-2} we have determined an ablation rate of approximately 40 ng (2 x 10^{14} atoms) per pulse. An ionisation fraction of 0.2 corresponds to ~10^{13} charged particles. From (3.28) taking T_e = 1 eV and a probe area of 0.25 cm^2 results in $N_e > 10^{11}$. It is clear that the actual number of electrons far exceeds this minimum number and so there should not be any perturbation of the electron-energy distribution by our probes.

3.5 Probe size, sheath and edge effects

Theories are most fully developed for probes with highly symmetric geometries such as spheres, infinite planes and infinitely long cylinders. As a result end and edge effects, which could influence the probe characteristic, have only received modest attention due to the difficulty in their analysis. Hopkins *et al* [13] carried out Langmuir probe analysis of a medium-density plasma (10^{16} - 10^{18} m^{-3}) produced using a tandem multi-pole ion source. Both planar (d = 0.5 cm) and cylindrical (d = 1.9 mm) probes were used for the analysis. The plane probe was initially chosen due to the apparently simple theory required to understand its behaviour [14]. The predicted saturation of the electron current above the plasma potential should make determination of the electron density possible using relatively small bias voltages. Similarly the predicted saturation of the positive ion current should allow determination of the ion density at probe biases sufficiently negative to avoid high-energy electrons. In practise however it was found the IV characteristic did not saturate. The ion current was found to change nonlinearly with voltage resulting in difficulty in extrapolating the ion current.

Weber *et al* [15] used a plane Langmuir probe (d = 1 cm) to detect a low energy ion beam in a low pressure, nearly collisionless plasma produced using a double plasma machine. The parameters were a gas pressure of 6 x 10^{-4} mbar, an electron temperature of 1 eV, an ion temperature of 0.1 eV and an electron density of 10^{15} m^{-3}. This setup is somewhat comparable to our laser produced plasma where we have a highly directional supersonic flow of ions. It was found that the presence of an ion beam arriving perpendicular to the plane of the probe produced a double knee in the IV characteristic at a positive bias with respect to the plasma potential. They suggested that when the beam was stopped and reflected, the ions constitute a large space charge region. This changes the planar symmetry and results in an increase in the electron current to the probe. Electrons are drawn in sideways by the disturbed space-charge field, which acted to increase the effective collecting area of the probe. For a cylindrical probe there was no effect of the ion beam on the IV characteristic. In this case the ion beam would not be stopped but only deflected around the probe and therefore not contribute to the space charge effect.

Stamate *et al* [16] looked at the surface condition of a plane disk probe in a reactive plasma. The measurements were carried out in Ar and O_2 plasmas (discharge current, I_d = 10 – 100 mA and a gas pressure of 0.5 to 10 mTorr) and the plane probes were gold, with a diameter of 1 cm and thickness of 0.3 mm.

The probe bias for the experiments varied from –100 to –150 V. The probe surfaces showed rings where significant sputtering took place. A two-face plane probe was also used and this showed similar rings on the back surface though not as distinct as the front. They found that the edge effect of the probe induced an elliptic-like sheath structure that acted as an electrostatic lens. This focussed the charged particles onto different regions of the probe dividing the probe into distinct areas with different work functions.

The collecting area of a double-sided, planar Langmuir probe was investigated by Sheridan [17] using a hybrid simulation with cold, collisionless ions and Boltzmann electrons.

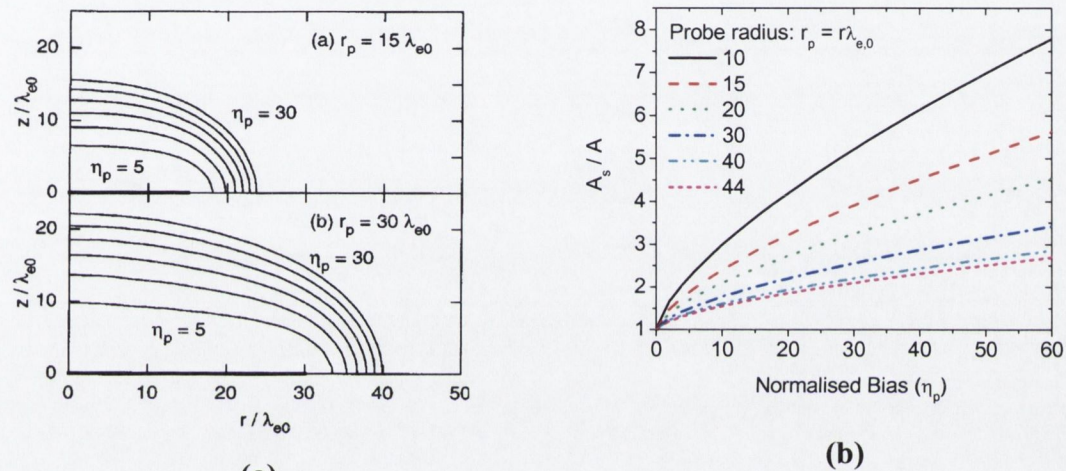

(a) **(b)**

Fig.3.6(a)[1] The expansion of the steady-state sheath with probe bias for two probes of different radii (a) $r_p = 15\lambda_{e,0}$ and (b) $r_p = 30\lambda_{e,0}$ where $\lambda_{e,0}$ is the electron Debye length. The probe bias ranges from $\eta_p = -5 \rightarrow -30$ $^{kT_e}/_{e}$ with $T_e = 0.5$ eV.

(b) Potential dependence, $\eta_p = {}^{-e\phi_p}/_{kT_e}$, of the normalised sheath area for disks of various radii, $^{r_p}/_{\lambda_{e,0}}$.

[1] Fig.3 Sheridan *et al*, Phys. Plasmas, Vol. 7, July 2000

Sheridan *et al* looked at how the collecting area depended on the probe bias and radius. To determine the sheath structure around the disk, a two-dimensional code with PIC (Particle in Cell) ions was used. The sheath edge was taken to be the surface on which the average ion velocity equals the Bohm speed, and the sheath area was normalised by the double-sided probe area ($A = 2\pi r_p^2$). Fig.3.6(a) shows the results from the model. It was found that the sheath showed an oblate ellipsoid-like shape, becoming more spherical as the probe bias was increased. The sheath was seen to be nearest the probe at the edge of the disk, while for the same probe bias the sheath was much closer to the proportionally smaller probe. If we take for comparison a probe which we would consider small, (a plane disk with a diameter of 1 mm) and assume an electron temperature of $T_e = 0.5\,\text{eV}$ and an ion density of $n_i = 2\times10^{17}\,\text{m}^{-3}$ we get the following parameters:

$$\begin{aligned} \lambda_D &= \sqrt{\frac{\varepsilon_0 k T_e}{e^2 n_0}} = 11.5\,\mu\text{m} \\ r_p &= r/\lambda_D = 44 \\ Z &= \sqrt{\frac{2\varepsilon_0 V_0}{e n_0}} = 126\,\mu\text{m} \\ Z/\lambda_D &= 11 \end{aligned} \tag{3.29}$$

where r_p is the probe radius normalised to the Debye length and Z is the sheath thickness estimated using the matrix sheath formula. Fig.3.6 (b) shows the potential dependence of the normalised sheath area (A_s/A) for a range of probe radii. The computed values, A_s/A were fitted with the following function:

$$\begin{aligned} \frac{A_s}{A} &= 1 + a\eta_p^b \\ a &= 2.28 r_p^{-0.749} \\ b &= 0.806 r_p^{-0.0692} \end{aligned} \tag{3.30}$$

where η_p is the probe bias given by $\eta_p = -e\phi_p/kT_e$.

According to the model our probe would be considered relatively large showing a minimal in edge effects, (Fig.3.6(b), pink line). However we see that the area of the sheath exceeds that of the disk by up to a factor of 2.5 depending on the probe bias. The value of $r_p = 10$ would correspond to a probe with radius, r = 0.1 mm.

While these results are for a collisionless, steady-state sheath surrounding a two-sided conducting disk and include a number of uncertainties as discussed in the paper, it provides a useful guide along with the model developed by Waymouth in deciding on the probe geometry and size.

3.6 Conclusion I

As a result of the previous calculations we have designed probes of suitable dimensions to measure the properties of an expanding silver plasma. We saw from Fig.3.2(a) that the magnitude of the ion signal did not vary greatly with bias voltages greater than –3 V. Hence to obtain the ion saturation current, biases greater than this were applied.

3.7 Ion velocity and energy distribution

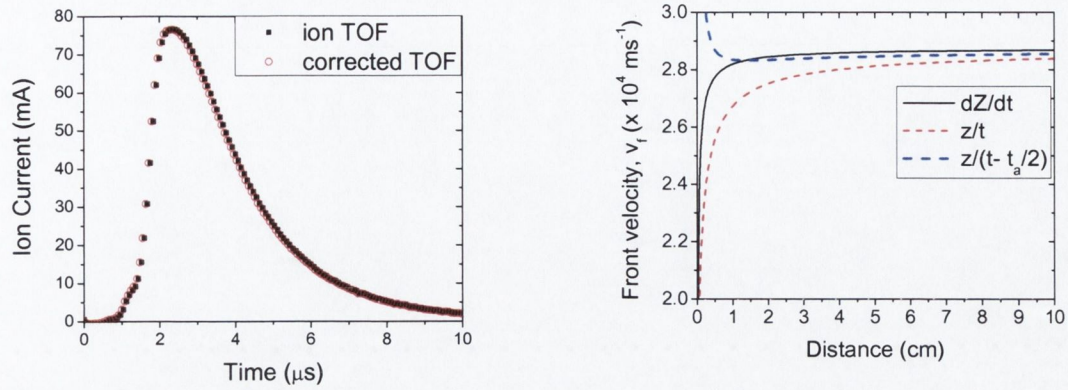

(a) **(b)**

Fig.3.7 (a) Ion signal from a planar probe, biased at –10 V at 4.1 cm from a silver target. The black square is the measured signal while the red circle is the signal corrected for the acceleration time. **(b)** The front velocity determined using z/t, compared to the velocity determined from the Anisimov model, (dZ/dt). z is the plume front position and t is the arrival time.

The ion flow velocity is probably the simplest plasma parameter to determine using a Langmuir probe. The flow velocity is determined from data like that in Fig.3.7(a), by using the equation: $v_i = z/t$, where z is the probe distance. However as we mentioned previously this disregards the time taken for the ablation, plume formation and the initial acceleration of the plasma. Fig.3.7(a) shows a measured ion TOF signal from a plane probe 4.1 cm from a silver target ablated at a fluence of 2 J cm^{-2}. Fig.3.7(b) shows the ion front velocity determined from the Anisimov model using the plume front position, (z / t), compared to the instantaneous velocity, dZ/dt, also determined from the Anisimov model.

The discrepancy, while small, can be corrected for quite easily. We can approximate the plume front as accelerating from rest for a time t_a, after which it reaches a constant velocity, v_f. The distance traveled is then, $s = z = v_f\left(t - t_a/2\right)$. From Fig.3.7(b) we can calculate t_a for each distance, z. The average acceleration time was determined to be approximately 50 ns. The ion TOF signal can now be corrected, by replacing t with, $t - t_a/2$. Fig.3.7(a) shows the corrected TOF signal in red.

The ion density can now be determined from the TOF signal using (3.16). Fig.3.8(a) shows how the ion density varies with time. The ion energy distribution within the plasma can also be determined from the ion TOF signals using the following relationship:

$$I(t) = e\frac{dF}{dt} \;\&\; E = \frac{1}{2}m_i v_i^2$$
$$\frac{dF}{dE} = I(t) \times \frac{t^3}{emd^2} \qquad (3.31)$$

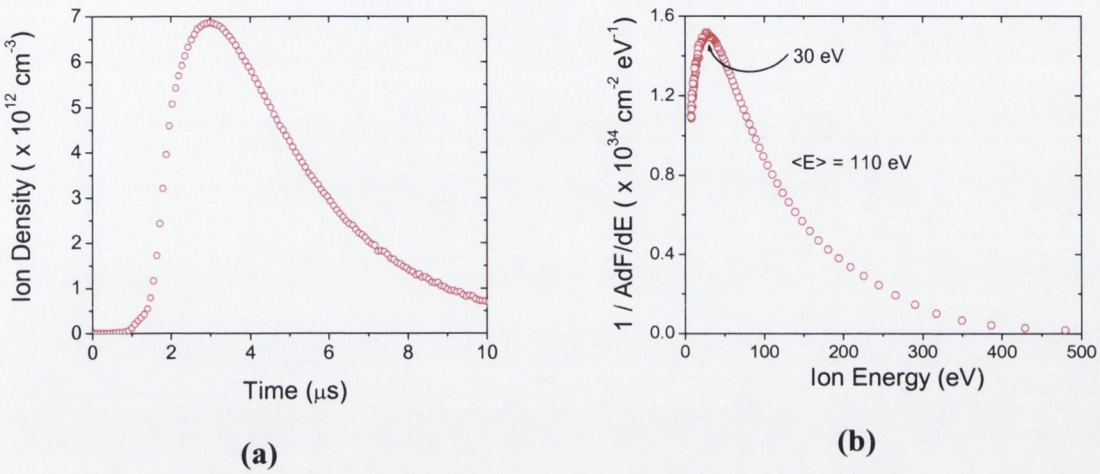

(a) **(b)**

Fig.3.8 (a) Ion density vs. time, 4.1 cm from the target. The peak in the ion density corresponds to the time of maximum ion flux. **(b)** The corresponding ion energy distribution calculated from the TOF spectrum using (3.31).

Fig.3.8 (b) indicates a mean ion energy of ~ 110 eV and a most probable energy of ~ 30 eV for the ablation of silver at 2 J cm^{-2}. Ions with this range of energies (10 – 500 eV) can still reach the probe even with a positive bias of 1 to 3 V applied. While it is possible to correct for this by subtracting the ion current from the IV characteristic [9] it is not yet established that this method yields reliable values of electron temperature. We have studied the behaviour of the planar probe where it is orientated so that the plasma flow is parallel to the surface of the probe, $\theta = 90°$ (Fig.3.9(a)). In this way the ion current due to the plasma flow can be eliminated.

3.8 Probe rotation

The current measured by the probe at a particular time is proportional to the density of ions (n_i) in the plasma through $I_i = ev_i An_i$, where v_i is the ion flow velocity. Other work [18] has included an additional term to include the thermal ion flux to the probe satisfying the Bohm criterion. If we compare the plasma flow velocity to the Bohm velocity, $u_B = \sqrt{kT_e/m_i}$, for a typical electron temperature of $T_e = 0.5\,eV$ and silver ions, we see that $v_i = 23\,u_B$. Thus for a negatively biased planar probe orientated normal to the plasma flow, the ion current will be dominated by the ion flux due to the flow. Fig.3.9 (b) shows the ion TOF signals as the probe is rotated.

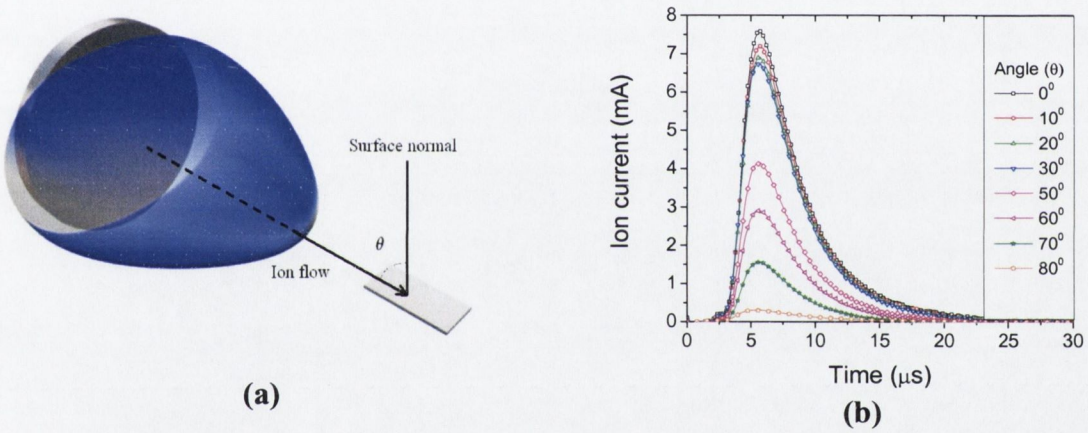

Fig.3.9 (a) Probe orientation (θ) relative to the plasma flow. In this example, θ = 90°. **(b)** The ion TOF signals with increasing angle.

Fig.3.10(a) shows the ion current variation to the probe for $\theta = 0^\circ$ and 90°. It is clear that when the probe surface is parallel to the plasma flow the ion current has a strong dependence on the bias voltage.

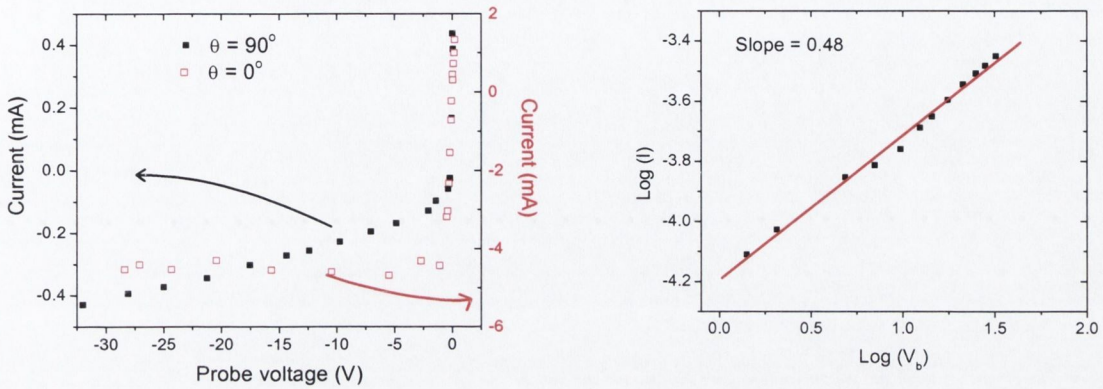

(a) **(b)**

Fig.3.10(a) Ion current variation with $\theta = 0^\circ$ and 90°. **(b)** A log-log plot of the ion current parallel to the flow.

The results from Fig.3.10(a) in the parallel case resemble the trend that would be obtained from a cylindrical probe, where increasing the magnitude of the bias voltage increases the sheath size, thus increasing the collecting area. From the literature [19] the current to a cylindrical probe should have a $V^{1/2}$ dependence. The log-log plot of Fig.3.10(b) shows this dependence.

Work has been carried out with plasma jets flowing parallel to a probe surface [20, 21]. It has been suggested by Clements *et al* [22] that for most experimental situations a negative probe surrounded by a flowing high-pressure plasma operated in one of two regimes. Diffusion-convection or sheath-convection. In the case of diffusion-convection the ions diffuse from the plasma as it moves past the probe and a saturation current independent of the bias voltage is obtained providing the bias was sufficiently negative to repel the electrons. In the sheath-convection regime the sheath expands beyond the diffusion layer extracting more ions from the plasma. No saturation is obtained as an increase in the bias voltage increases the sheath thickness with a corresponding increase in probe current. The various regimes may be categorised using the following parameters:

- The electronic Reynolds number, R_e, given by, $vLe/\mu_i kT_e$, where μ_i is the
- The electronic Reynolds number, R_e, given by, $vLe/\mu_i kT_e$, where μ_i is the ion mobility.
- $\chi = eV_0/kT_e$

When R_e is less than unity, the plasma is considered at rest and the conventional diffusion relations may be applied. When R_e is greater than unity, the ions are convected to the probe by a boundary diffusion layer if $R_e\alpha^2\chi^2 < 1$, or via a convection supported ion sheath if $R_e\alpha^2\chi^2 > 1$. If we take some typical values such as $v_i = 1.5\times10^4\ ms^{-1}$, L = 7 mm, $kT_e = 0.5$ eV and V_0 = 30 V we see that: $R_e\alpha^2\chi^2 \gg 1$. For a negatively biased planar probe operating in the sheath-convection regime the current is given by [23]:

$$I = \left(\frac{9}{2}\right)^{1/4} (n_0 ev)^{3/4} (\varepsilon_0 \mu_i)^{1/4} V^{1/2} L^{1/4} z \qquad (3.32)$$

where n_0 is the ion and electron density in the plasma, L is the length of the probe, parallel to the flow, z is the width of the probe and μ_i is the ion mobility.

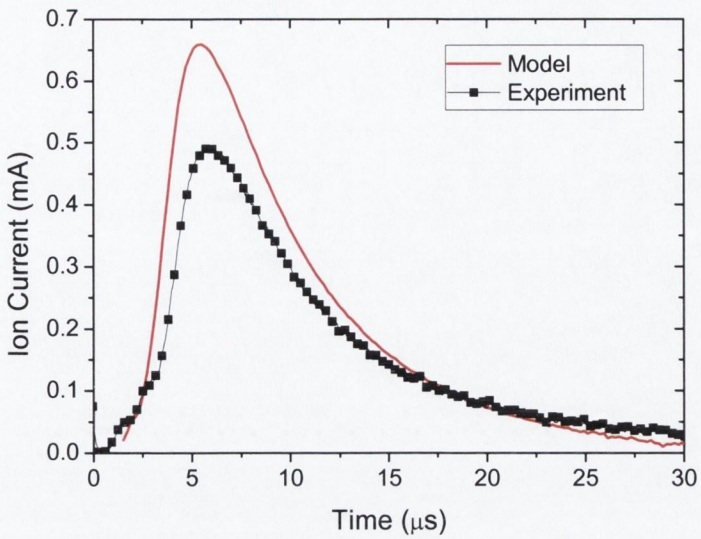

Fig.3.11 The result of (3.32) compared to the experimental result. The value for the ion mobility was taken to be 2×10^{-3} $m^2 V^{-1} s^{-1}$ from [24]·.

This model was developed for a high-pressure plasma where the mean free paths of the charged particles are much less than the probe dimensions and the current to the probe is determined by a diffusion or mobility controlled process. We have shown in section 2.2 that we lie in the collisionless-sheath regime and as such cannot directly compare the results. However it is interesting to note the similar $V^{1/2}$ dependence observed.

3.9 Plasma immersion ion implantation

The common implantation technique of Plasma Immersion Ion Implantation (PIII) shows some similarities to the operation of our plane probe lying parallel to the plasma flow. PIII is a method used to modify the structure and/or the composition of the near-surface region of a target. In PIII, the target is immersed into a quasineutral plasma and bombarded by ions accelerated by negative high-voltage pulses, typically 10 – 100 kV. When the high-voltage pulse is applied, the electrons near the surface are repelled in the time scale of the inverse electron plasma frequency $\left(\omega_{pe}^{-1}\right)$, leaving behind a uniform density 'matrix' sheath of ions. On the time scale of the inverse ion plasma frequency, ions within this sheath are accelerated into the target resulting in a high current peak. Subsequently the sheath expands until a steady state Child-Langmuir sheath is formed, however this regime is generally of little interest because the sheath thickness exceeds the plasma size.

The PIII situation is somewhat similar to that of our probe-plasma interaction as when the leading edge of the plasma encounters the edge of the negatively biased probe nearest the target, the electrons are repelled and a matrix sheath is formed. The thickness, s_0 of this sheath is given by:

$$s_0 = \left(2\varepsilon_0 V / en_0\right)^{1/2} \tag{3.33}$$

Ions from the matrix sheath are collected by the probe / target over a timescale given by:

$$\frac{u_0}{s_0} = \left(\frac{e^2 n_0}{\varepsilon_0 m_i}\right)^{1/2} = \omega_{pi} \tag{3.34}$$

where u_0 is the characteristic ion velocity given by $\left(2eV/m_i\right)^{1/2}$, m_i is the ion mass and ω_{pi} is the ion plasma frequency. On a longer time scale this sheath evolves into a steady state Child-law sheath with the timescale:

$$t_c \approx \left(\sqrt{2}/9\right)\omega_{pi}^{-1}\left(2V/T_e\right)^{3/4} \tag{3.35}$$

with a thickness:

$$s_c = s_0\left[\frac{2}{9}\frac{u_0}{u_B}\right]^{1/2} \tag{3.36}$$

Fig.3. 12 gives an example of the sheath development as an element of plasma travels across the probe. The time taken for the Child-law sheath to be established, t_c, can be shorter than the time taken for the element of plasma to travel the length of the probe. Thus the current to the probe from that plasma element will vary in a complicated manner. It should be possible to use the plasma immersion ion implantation models of Lieberman [25] or Riemann [8] to estimate the average current to the probe as a plasma element travels the length of the probe. In the following sections we shall present the important points of the models and compare them to an analytical model developed in collaboration with Peter Sheerin and Myles Turner from the plasma research group in Dublin City University.

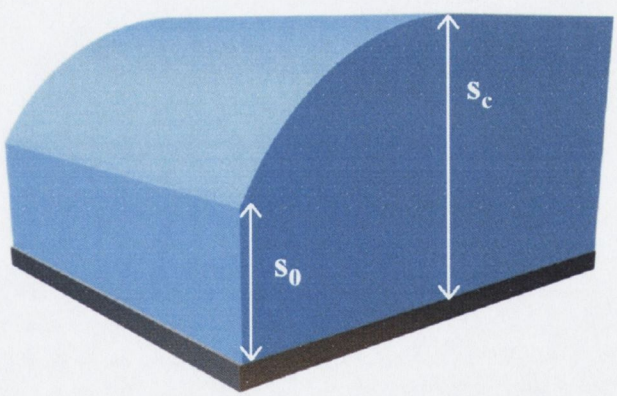

Fig.3. 12 Evolution of the probe sheath from a matrix sheath with thickness s_0 to a Child-law sheath with thickness s_c.

3.9.1 Lieberman model

Lieberman developed an approximate analytical model for an applied rectangular voltage pulse in a 1-D planar geometry. The models start with 5 basic assumptions:

1) The ion flow is collisionless.
2) The electron motion is inertialess (characteristic implantation time scale much larger than ω_{pe}^{-1}).
3) The applied voltage V_0 is much greater than T_e; hence the Debye length $\lambda_d \square s_0$ and the sheath edge is abrupt.
4) During and after the matrix sheath implantation, a quasistatic Child law sheath forms. The current demanded by this sheath is supplied by the uncovering of ions at the moving sheath edge and by the drift of ions towards the target at the Bohm speed.
5) During the motion of an ion across the sheath, the E-field is frozen at its initial value, independent of time, except for the change in field due to the velocity of the moving sheath.

While assumptions 1-3 depend on the plasma process and parameters and seem reasonable, assumptions 4 and 5 are used to permit an analytical solution to the sheath motion and their validity must be questioned. When the voltage step $(-V_0)$ is applied to the plane surface immersed in the plasma, a matrix sheath is formed and from Lieberman's calculations, the normalised current from that sheath is given by:

$$J = \frac{\sinh T}{\cosh^2 T} + \frac{2}{9}\frac{1 + T\sinh T - \cosh T}{\cosh^2 T} \tag{3.37}$$

where T is a normalized time $(T = \omega_{pi} t)$, and J is the normalized implantation current density $J = \frac{j}{en_0 u_0}$. This matrix extraction phase ends after a few ω_{pi}^{-1}, which corresponds to ~T = 3. After this time the sheath begins to expand into a steady Child-law sheath. In this regime, the normalised implantation current density is given by:

$$J = \frac{1}{9/2\left(x_0^2/s_0^2\right) + 3} \tag{3.38}$$

where

$$T = \omega_{pi} t = \frac{3}{2}\left(\frac{x_0^3}{s_0^3}\right) - \frac{3}{2} + 3\left(\frac{x_0}{s_0}\right) \tag{3.39}$$

x_0 is the distance of an ion away from the probe when it begins its flight across the sheath. These equations give J(T) as a parametric function of $\left(\frac{x_0}{s_0}\right)$. An important point to note is that the maximum value of x_0 corresponds to the Child-sheath thickness, which in turn, depends on the electron temperature. As a result, the overall current to the probe will be a function of T_e.

3.9.2 Riemann & Daube model

This model set out to describe the formation of the high current peak during the matrix extraction phase. It agrees with assumptions 1 to 3 from Lieberman as they depend on the plasma process, however they say that assumptions 4 and 5 are artificial and could be disproved by comparison to solutions from the corresponding ion fluid equations. This competing model is based on a special class of simultaneous exact solutions of the ion fluid equations and of Poisson's equation to describe the matrix extraction phase. They then use simple parameters to extend the theory to the sheath expansion phase. The model makes use of the following normalised quantities:

1) $T = \omega_{pi} t$

2) $n(x,t) = {}^{n_i}\!/_{n_0}$, and $u(x,t) = {}^{u_i}\!/_{c_s}$.

3) $\Phi(x,t) = {}^{-eV_0}\!/_{kT_e}$

where n_i is the ion density, n_0 is the undisturbed plasma density, u_i is the ion flow velocity and c_s is the ion sound speed also known as the Bohm velocity. The boundary conditions at the sheath edge $(x = s)$ follow from the constant values:

$$\Phi = 0, n = 1, u = 1 \tag{3.40}$$

of the plasma far from the target. The ion velocity, u = 1, is given by the Bohm criterion. The initial conditions are:

$$n(x,0) = 1, \quad u(x,0) = 1, \quad \Phi(x,0) = \frac{1}{2}(x - s_0)^2, \quad (x \geq s_0) \tag{3.41}$$

of a uniform matrix sheath at t = 0. The model results in the following approximation for the ion current to the target during the matrix regime.

$$j(T) = n(0,T)u(0,T) = \frac{1 + u_0 T + u_0 T^3/12}{(1 + {}^{T^2}\!/_2)^2} \tag{3.42}$$

Here, $s(0) = s_0 = -\sqrt{2\Phi_0}$, measured in Debye lengths (λ_D), and T is the normalised time. Φ_0 can be taken as the bias voltage assuming $|V_0| > kT_e$.

For the sheath expansion phase, T > 3, Riemann presents a '*crude approximation*' for the ion current. He uses two free parameters α and β to obtain:

$$j = 1 - \beta\left(1 + \frac{\alpha s_0^{\,2}}{2s^2}\right)\left(1 - \frac{s_\infty^{\,2}}{s^2}\right) \tag{3.43}$$

in parametric form as a function of the sheath boundary, s. The corresponding time is given by:

$$T(s) = T_E + \frac{1}{\beta}\left[s - s_E + s_\infty\left(\tanh^{-1}\frac{s_E}{s_\infty} - \tanh^{-1}\frac{s}{s_\infty}\right)\right] \tag{3.44}$$

T_E is the time at which the matrix extraction phase has ended and has been found to be ~3. s_E is the sheath thickness at this time and is given by the approximation $s_E \approx 1.6s_0 + 3$.

3.9.3 Sheerin & Turner model

Sheerin and Turner set about developing a similar PIII analytical model [26]. They essentially used the same assumptions as Riemann and their result for the current to the probe was determined to be:

$$j_i(0,\tau) = \frac{en_0\left[u_0 - s_0\left(\omega_i^2\tau + \frac{1}{12}\omega_i^4\tau^3\right)\right]}{\left[1+(\omega_i\tau)^2/2\right]^2} \tag{3.45}$$

where $\tau = L/v_i$, (the probe length over the ion flow velocity). The value of u_0 is the component of the ion velocity towards the probe and in the parallel case is taken to be zero.

3.10 Comparison of Models

We can now compare all three models. For analysis we took a silver plasma with density, $n_0 = 1.3\times10^{17}\ m^{-3}$, an applied voltage of V_0 = 20 kV, and an electron temperature of T_e = 1eV. In PIII potentials of typically 10-100 kV are applied so we use a large potential here when comparing the models.

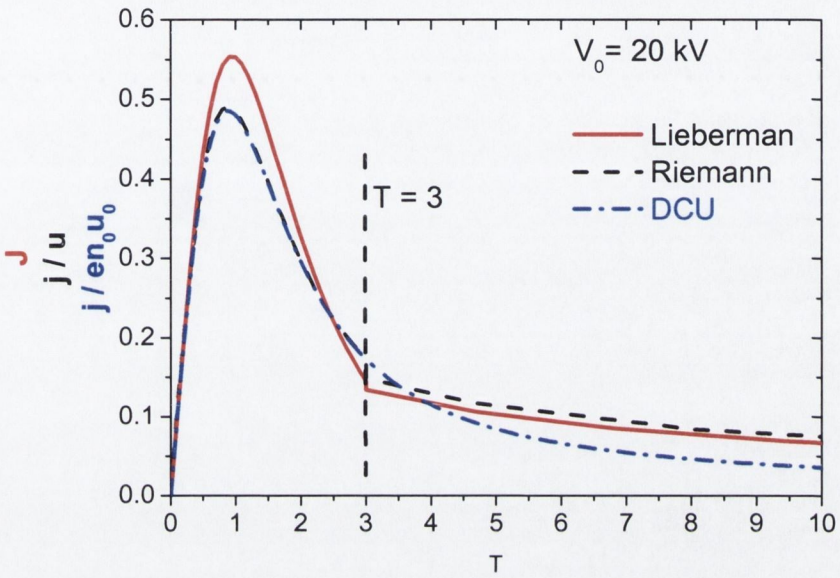

Fig.3.13 A comparison of the three models. The transition between the matrix and sheath expansion regimes occurs at approximately: T = 3. The normalisation factors for the Riemann and DCU models are shown on the Y-axis.

Fig.3.13 shows the normalised results from the models for the plasma parameters mentioned above. As an initial comparison it is useful to look at the two extremities, T = 0 & ∞. The values of the normalised current at T = 0, for the Lieberman, Riemann and DCU models are 0, 0.005 and 0 respectively. Un-normalising, 0.005 becomes 20 A m^{-2}, which is equivalent to the steady-state Child law current density ($j = en_0u_B$). In the matrix extraction phase the DCU and Riemann models agree very well. To corroborate the model, DCU has also carried out some PIC simulations and these have shown excellent agreement with their model. The Lieberman model however estimates a larger current, the integral being 7% larger.

If we look at the transition region, Lieberman shows a large discontinuity between both phases, unlike the Riemann model. This smoother transition is due to the evolution of the sheath during the matrix phase being included in the calculations. The DCU model however does not take into account the sheath expansion and so it approaches zero as T $\rightarrow\infty$. In the sheath expansion phase both the Riemann and Liberman models depend on the ratio of s/s_0. The maximum ratio this can have depends on the Child sheath thickness, which in turn depends on the electron temperature, T_e. This should prove useful when comparing the results for various temperatures to the experimental results.

3.11 Conclusions II

In this chapter we set out to describe the application of a Langmuir probe to a laser produced plasma. The various collisional processes were described and it was shown that for typical plasma parameters we could use a collisionless sheath theory to interpret the probe characteristics.

A model of probe perturbation developed by Waymouth allows us to estimate whether the probe perturbs the plasma, while the results from Sheridan gives us an indication of the sheath size compared to the collecting area of the probe. These results allow us to design a probe small enough to avoid perturbing the plasma yet large enough so that sheath edge effects are kept to a minimum.

The acceleration phase of the plasma has been investigated and from the Anisimov model it has been determined to be approximately 80 ns. With this acceleration time the correct ion flow velocity can be determined from the measured TOF signal. From the corrected TOF signal the ion energy distribution was calculated. For the ablation of silver at 2 J cm^{-2} ions with energies of up to 500 eV are present with the average energy being 110 eV.

We have suggested that rotating the probe so as the collecting surface is aligned parallel to the plasma flow could be advantageous as the current due to the flow is effectively eliminated. Finally, we presented some plasma immersion ion implantation models which could be used to interpret the probe results in this new orientation. From the models the ion current to the probe can be determined and where a Child sheath develops the electron temperature can be deduced.

3.12 References

1. Goldston, R.J. and Rutherford, P.H., *Introduction to plasma physics*. 1995, Bristol: Institute of Physics Publishing.
2. Phipps, C.R. and R.W, D., *The high laser irradiance regime*, in *Laser Ionization Mass Analysis*, A. Vertes, R. Gijbels, and F. Adams, Editors. p.369. John Wiley & Sons (1993)
3. Huddlestone, R.H. and Leonard, S.L., *Plasma diagnostic techniques*. Pure and applied physics series. 1965: Academic P.
4. Chen, F.F., *Introduction to plasma physics and controlled fusion*. 2nd ed. 1984, New York: :Plenum Press.
5. Amoruso, S., *et al.*, *Applied Surface Science*, **138-139**: p. 250(1999).
6. Lunney, J.G. and Jordan, R., *Applied Surface Science*, **127-129**: p. 941(1998).
7. Demidov, V.I., Ratynskaia, S.V., and Rypdal, K., *Review of Scientific Instruments*, **73**(10): p. 3409(2002).
8. Riemann, K.U. and Daube, T., *Journal of Applied Physics*, **86**(3): p. 1202(1999).
9. Doggett, B., Budtz-Joergensen, C., Lunney, J.G., Sheerin, P., and Turner, M.M., *Applied Surface Science*, **247**(1-4): p. 134(2005).
10. Godyak, V.A., Piejak, R.B., and Alexandrovich, B.M., *Journal of Applied Physics*, **73**(8): p. 3657(1993).
11. Waymouth, J.F., *Journal of Applied Physics*, **37**(12): p. 4492(1966).
12. Spitzer, L., *Physics of fully ionized gases*. 2nd revised ed. Tracts on physics and astronomy;no.3. 1962: Interscience.
13. Hopkins, M.B. and Graham, W.G., *Review of Scientific Instruments*, **57**(9): p. 2210(1986).
14. Schott, L., *Plasma Diagnostics*, ed. W.L. Holtgreven. 1968, Amsterdam: North-Holland.
15. Weber, W.J., Armstrong, R.J., and Trulsen, J., *Journal of Applied Physics*, **50**(7): p. 4545(1979).
16. Stamate, E. and Ohe, K., *Applied Physics Letters*, **78**(2): p. 153(2001).
17. Sheridan, T.E., *Physics of Plasmas*, **7**(7): p. 3084(2000).
18. Mayo, R.M., Newman, J.W., Sharma, A., Yamagata, Y., and Narayan, J., *Journal of Applied Physics*, **86**(5): p. 2865(1999).

19. von Gutfeld, R.J. and Dreyfus, R.W., *Applied Physics Letters*, **54**(13): p. 1212(1989).
20. Pert, G.J., *Journal of Physics D (Applied Physics)*, **4**(11): p. 1702(1971).
21. Giles, C.R., Clements, R.M., and Smy, P.R., *Journal of Physics D: Applied Physics*, **12**(1): p. 33(1980).
22. Clements, R.M., Rizvi, A.H., and Smy, P.R., *IEEE Transactions on Plasma Science*, **22**(4): p. 435(1994).
23. Clements, R.M. and Smy, P.R., *Canadian Journal of Physics*, **49**: p. 2540(1971).
24. Clements, R.M. and Smy, P.R., *Journal of Applied Physics*, **41**(9): p. 3745(1970).
25. Lieberman, M.A., *Journal of Applied Physics*, **66**(7): p. 2926(1989).
26. Sheerin, P., Turner, M.M., Doggett, B., and Lunney, J.G., (unpublished).

4. Experimental Results

The experimental results obtained for the analysis of the ablation of silver are presented in this chapter. The experimental setup and the method for interpreting the results have been outlined in the previous chapters. The first step is to accurately determine the orientation of the probe relative to the direction of the plasma flow at the probe position. In the perpendicular orientation the ion density can be determined in a straightforward manner from the ion flow velocity as discussed in chapter 3. The electron temperature and density are measured using the IV characteristic, corrected to account for the ion current contribution. These results are then compared to those obtained with the probe aligned parallel to the plasma flow.

Ablation and deposition experiments are carried out in order to compare the distribution of the ions and neutrals. The amount of material deposited on a film is compared to the amount of material ablated from the target. We compare the ion yield to the measured mass loss and estimate an ion fraction. The electron temperature results from the Langmuir probe results, the PIII and Anisimov models are compared and finally we present the results obtained using the Energy Selective – Time of Flight Mass Spectrometer (ES-TOFMS). This device enables us to determine the mass-to-charge ratio of the various ions and to determine their energy distribution.

4.1 Probe orientation

We show in Fig.4.1(a) the peak ion current obtained from a plane probe as it was rotated relative to the plasma flow ($\theta = 0^\circ - 90^\circ$). It is clear that the magnitude of the ion current depends on the area of the probe projected towards the plume. In contrast, the electron signals do not show a strong dependence on the probe orientation except when the probe moves beyond $\theta = 90^\circ$, the magnitude decreases sharply as shown in Fig.4.1(b). This method was used to accurately align the probe to the plasma flow.

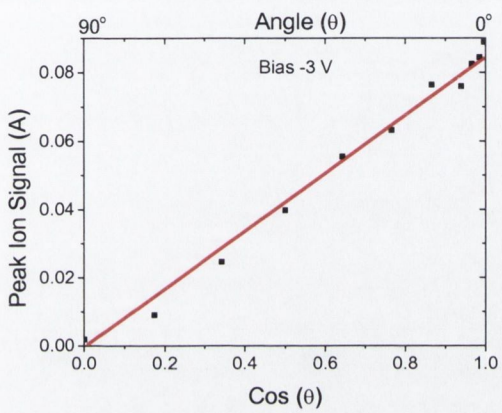

(a)

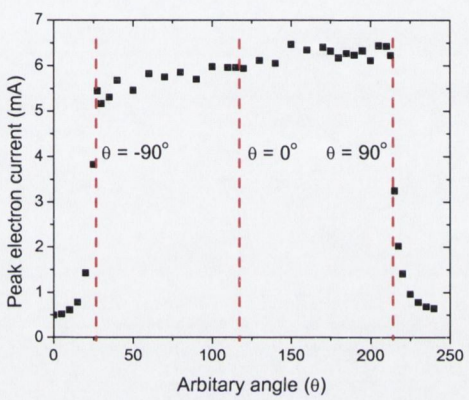

(b)

Fig.4.1 (a) The peak ion current to the probe with probe angle (θ) relative to the target. The solid line is a linear fit to the data. The probe bias was maintained at –3 V. **(b)** Peak electron current from the probe signals as the probe is rotated. The probe is placed initially at a random angle and rotated through 360°. From the graph we can determine the angle at which the probe is perpendicular or parallel to the flow.

4.2 Plane probe perpendicular to flow

Fig.4.2(a) shows a measured ion TOF signal obtained close to the target normal. It was obtained using a planar probe (3 x 1.5 mm^2), biased at – 5 V and positioned 4.1 cm from a rotating silver target. The laser fluence was 2 J cm^{-2} with a laser spot of 1.8 x 0.7 mm^2. From the front arrival time of 1.4 μs, the front velocity, v_f, is 2.9 x 10^4 m s^{-1} or 470 eV, while the peak time of 2.4 μs corresponds to a velocity of 1.7 x 10^4 m s^{-1} or 163 eV. Using this ion flow velocity and the equation: $I_{i,sat} = Aen_iv_i$, the maximum ion density is $n_{i,max} = 6 \times 10^{18}$ m^{-3}.

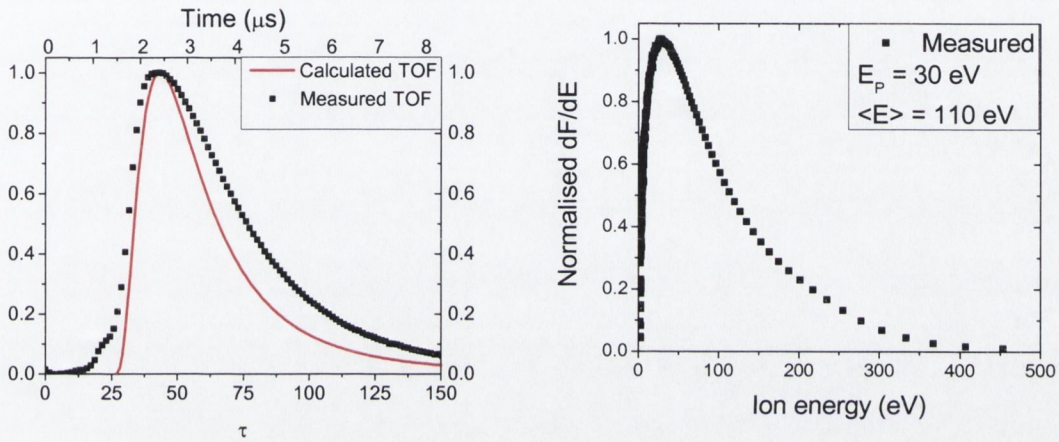

(a) **(b)**

Fig.4.2 (a) The calculated TOF from Anisimov using (1.11) and $\gamma = 1.28$, compared to the measured TOF signal. **(b)** The ion energy distribution from the measured TOF indicating the probable, E_p, and average, <E> ion energy, similar to Fig.3.8(b).

We show in Fig.4.2(a) the measured TOF compared to the calculated TOF using the Anisimov model as described in chapter 1. The values of X_0 and Y_0 were taken to be the laser spot dimensions and were determined using a microscope, while Z_0 was estimated using the front velocity:

$$Z_0 = c_s \tau_p$$
$$c_s = \frac{\gamma - 1}{2} v_f \qquad (4.1)$$

Z_0 was determined to be 109 μm. The adiabatic index, γ, was estimated to be 1.28 from the ratios of the front velocity to the peak TOF using (1.17). This value is in the same region as the value of γ = 1.25 determined for the ablation of silver at a fluence of 0.8 J cm^{-2} by Hansen [1] though at a wavelength of 355 nm (6 ns). For the ablation of silver at 1064 nm Toftmann [2] found that a value of 1.42 gave a best fit to his results.

If we compare the peak time in the measured and calculated signals we can let τ = 43 = 2.4 μs. The relationship between τ and t is defined from Anisimov as:

$$\tau = \frac{t}{X_0}\left((5\gamma - 3)\frac{E_p}{M_p}\right)^{1/2} \tag{4.2}$$

where E_p is the energy of the plume and M_p is the plume mass. From these results the energy to mass ratio corresponds to 6 x 10^7 J kg^{-1} or 67 eV per atom or ion.

The measured ion energy distribution indicates a most probable energy of 30 eV with an average energy of ~ 100 eV. We have determined that the mass of the plume is approximately 200 ng which gives a plume energy of 12 mJ. As the incident laser energy was approximately 25 mJ / pulse we see that the plume absorbs < 50 % of the laser energy.

4.2.1 Ion angular distribution

By moving the probe around the target as shown in Fig.4.3(a), the shape of the plume can be obtained. We show in Fig.4.3(b) how the magnitude of the ion TOF signal decreases with increasing angle. By integrating the current detected at each angle, the angular distribution of the number of particles per unit area arriving is obtained.

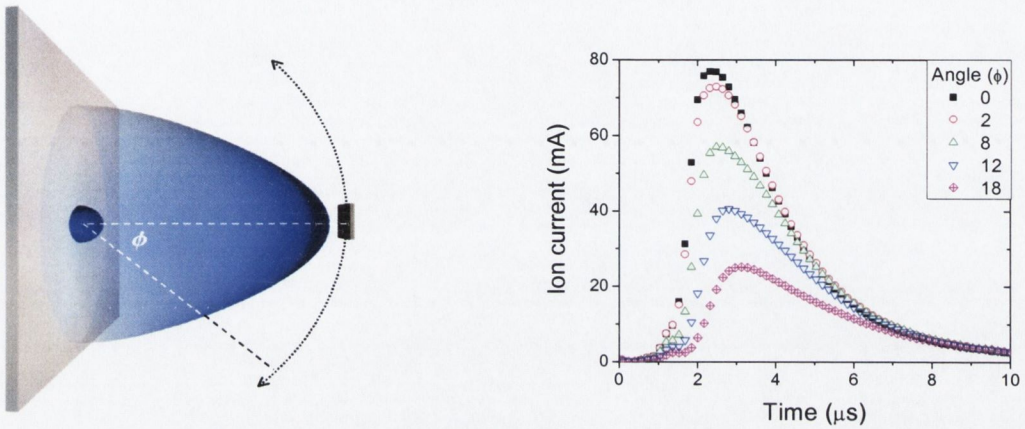

(a) **(b)**

Fig.4.3 (a) A schematic of the probe positioning to determine the angular distribution of the ablated particles **(b)** Ion TOF signals with increasing angle.

The ion angular distributions in both the X and Y directions were measured by rotating the probe in the ZX and ZY planes respectively. Fig.4.4(a) shows the ion angular distributions fitted using (1.23). The values of k obtained were $k_x = 2.9$ and $k_y = 1.9$. These results give an example of the flip over effect, which occurs whenever the laser profile at the target is not rotationally symmetric. The plume expansion is driven by the pressure gradients in the initial phase of the plume formation and since the pressure gradients will be greatest in the normal direction and in the lateral direction of the shortest extension the plume will be driven in the forward direction and in the direction with initially smallest dimension. Fig.4.4(b) shows the plume edge ratios determined from the Anisimov model. It indicates values of $k_x = 2.1$ and $k_y = 1.3$ which are somewhat lower than the experiment.

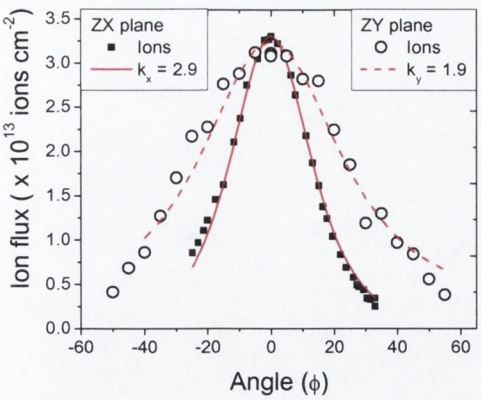

(a)

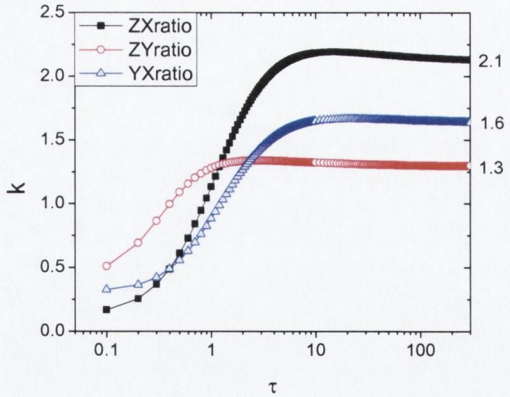

(b)

Fig.4.4 (a) The ion angular distribution in both the ZX and ZY planes **(b)** k determined using the Anisimov model.

From Fig.4.4(b) we can get some estimates of the time scale of the plasma expansion. The graph indicates that at $\tau = 1$, (~60 ns), the y-dimension becomes larger than the x-dimension indicating the flip-over effect, with the plume elongation reaching an asymptotic value at $\tau \sim 3$ (~180 ns).

It is possible to use the values of k from the experiment in the Anisimov model to determine an initial thickness Z_0. For $k_x = 2.9$ and $k_y = 1.9$, Z_0 corresponds to approximately 30 μm. Using (4.1), this thickness would result in a front velocity of ~ 8500 m s^{-1}. For a probe at 4.1 cm this would correspond to a TOF of 4.9 μs, which from Fig.4.2, is clearly not the case. This indicates that determining the initial thickness of the plasma using the front velocity is not the most accurate method.

4.2.2 Ion and neutral distribution

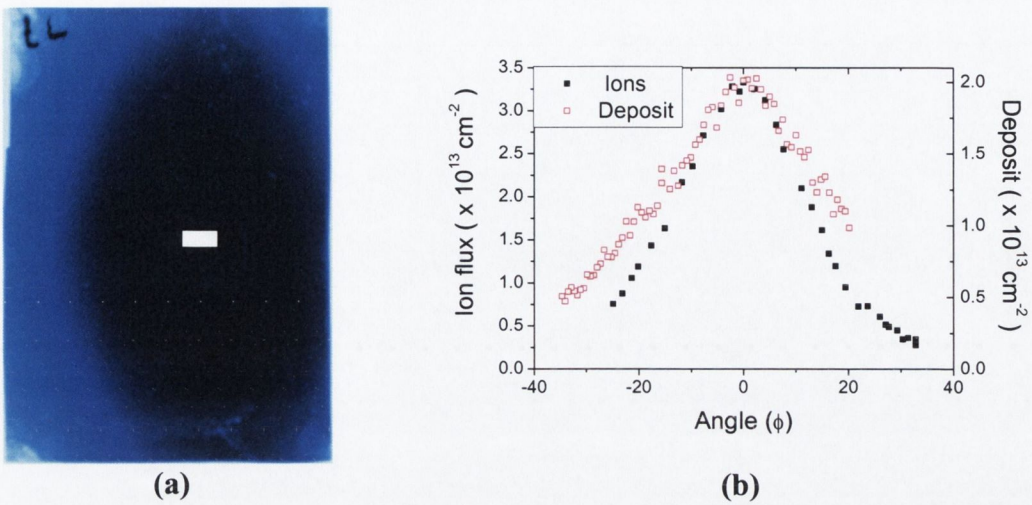

(a) **(b)**

Fig.4.5 (a) An image of a transparent film (7 x 11 cm), placed 5.7 cm from the target and deposited with 40,000 shots. The hole in the center allows the beam through to hit the target normally **(b)** The angular distribution of the ions compared to the deposit, adjusted to the probe distance of 4.1 cm.

We ablated silver at a fluence of 2 J cm^{-2} with 40,000 shots, and collected the material on a transparent film, placed 5.7 cm from the target. By measuring the optical transmission through the film, before and after the deposition, the thickness and angular distribution of material was calculated. The equations are presented in Appendix B. Fitting the angular distribution in the same way as before yielded k_x = 1.9 and k_y = 1.2 for the deposit, which shows that the ions have a more forward peaked distribution.

The total amount of material collected can be estimated from the Anisimov model using the equation:

$$F = \frac{2\pi d^2 F(0)}{k_x k_y} \tag{4.3}$$

where d is the distance in cm and F(0) is the flux at 0°. The thickest part of the film was determined to be 45 nm, which equates to F(0) = 6.2 x 10^{12} particles cm^{-2}. Using the k values obtained from the experiment, the yield was estimated to be 5.5 x 10^{14} particles / pulse. Similarly from the ion probe results the yield was estimated to be 6.2 x 10^{14} ions / pulse.

The mass loss and corresponding ablation depth was determined by weighing the target before and after ablation (60 mins, 10 Hz) using a microbalance with an accuracy of 2 μg. The ablation rates for a fluence of 1, 1.5 and 2 J cm^{-2} were determined to be 40, 65 and 200 ng per shot respectively. The ablation depths are then 3, 5 and 15 nm respectively.

A mass of 200 ng of silver corresponds to 1.1 x 10^{15} atoms. Comparing the ion yield to the mass loss, the ion fraction is then approximately 0.56. This is in good agreement with the value of 0.5 at 2 J cm^{-2} determined by Toftmann [2]. The discrepancy between the yield estimated from the deposited film and that from the mass loss results could be due a number of factors including the uncertainty in measuring the spot size or perhaps to sputtering from the impacting high-energy ions. From the ion energy distribution we saw that there were ions of up to 500 eV present. With the energy threshold being 10 – 25 eV for most metals we would expect some material to be removed. Fahler [3] determined the sputtering yield during PLD by measuring the deposition rate on a tilted substrate. From his results for a fluence of 2 J cm^{-2} the yield was approximately 0.4 for Ag ions. Even for a relatively low fluence of 1 J cm^{-2} he found a yield of 0.25. Comparing the mass loss to the yield determined from the film the sputtering yield appears to be approximately 0.5.

Table **4.1** presents a summary of the results obtained from the ablation of silver at 2 J cm^{-2}.

Table 4.1 A summary of the results for the ablation of silver at 2 J cm^{-2}.

Mass loss	Ion yield	Ion fraction	Deposit	Sputtered yield
1.1 x 10^{15}	6.2 x 10^{14}	0.56	5.5 x 10^{14}	0.5

4.2.3 Electron temperature

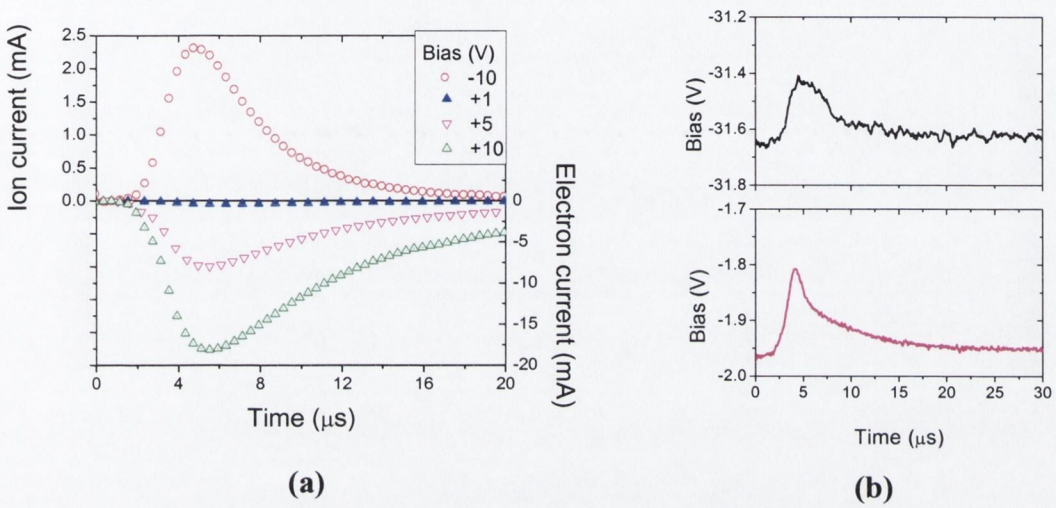

Fig.4.6 (a) Ion and electron signals for the probe oriented perpendicular to the flow. **(b)** Probe bias variation for a bias of -32 V (black) and -2 V (pink).

We show in Fig.4.6(a) some ion and electron probe signals obtained from a planar probe (13 x 3 mm^2), positioned 9.5 cm from the target. The fluence was maintained at 1.5 J cm^{-2}. The probe bias can be altered by the voltage drop across the load resistor (R_l) and the blocking capacitor (C_b). If we take the maximum current from Fig.4.6 of 2.3 mA, for a load resistor of 100 Ω implies a voltage drop of 0.23 V across the resistor. The voltage of $\sim \frac{1}{C_B}\int I(t)dt$ across the capacitor (0.6 μF) is approximately 20 mV.

The actual bias voltage is then the applied voltage minus these induced voltages. We show in Fig.4.6(b) the actual voltage on the probe for two bias voltages of -32 & -2 V. It is clear however that the load resistor has the largest influence and thus should be kept as small as possible.

Choosing a particular time and then plotting the current against the corrected bias voltage, the IV characteristic is obtained. For example at the peak TOF of 4.8 μF, the IV characteristic is plotted as shown in Fig.4.7(a). The electron temperature is found from a semi-logarithmic plot of the electron-retarding region after correcting the characteristic by subtracting the ion saturation current. From Fig.4.7(b) the value of $d\ln(I)/d(V)$ gives 0.25 eV for the electron temperature.

The best fit of the linear region is represented by the red line. The plasma potential (V_p) is obtained from the position of the knee of the electron saturation part of the characteristic. In practice this is determined using the intersecting slopes method as shown.

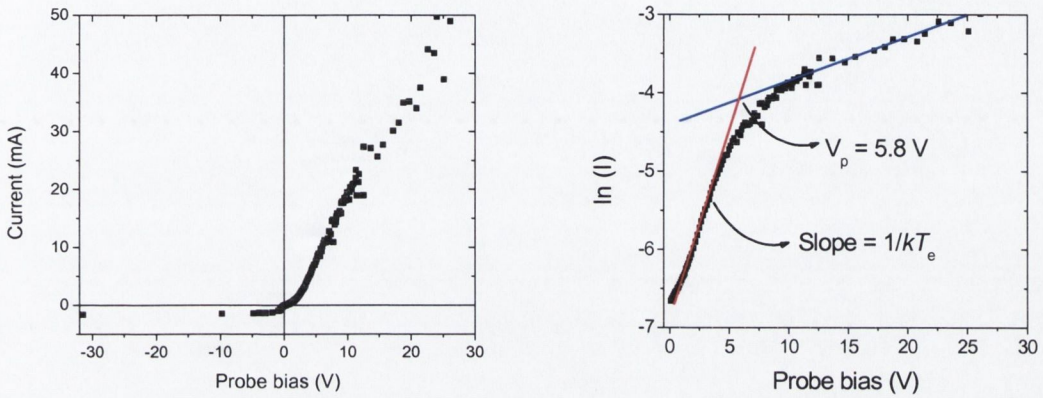

(a) **(b)**

Fig.4.7 (a) IV characteristic at 4.8 μs **(b)** Corrected semi-log plot showing how T_e and V_p are obtained.

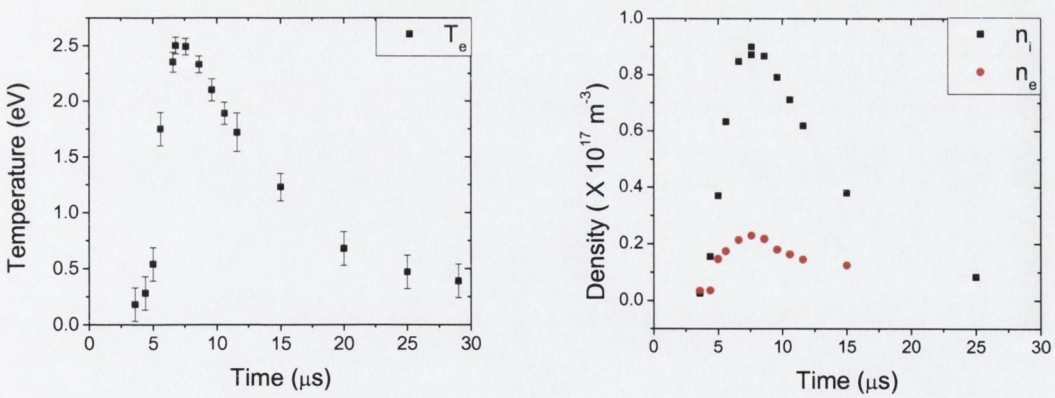

(a) **(b)**

Fig.4.8 (a) T_e variation determined from a range of IV characteristics for the planar probe perpendicular to flow. **(b)** Electron and ion density variation.

The temperature was found to increase to a maximum value of approximately 2.5 eV at 7.5 μs, which is slightly later than the peak in the ion TOF signals. This initial increase in temperature as the plasma arrives is consistent with the assumption that the plume is isentropic and the expansion is adiabatic. Similar work carried out by Hansen [1] has also seen this temperature variation. He ablated silver at a fluence of 0.8 J cm^{-2} and at a distance of 8 cm determined a maximum electron temperature of 0.7 eV.

Fig.4.8(b) shows the electron and ion density variation. Both show the same behaviour but with the electron density being a factor of four lower. The discrepancy between the ion and electron density is not yet fully understood. The results presented in section 3.5 would suggest that the opposite would occur as both Weber [4] and Stamate [5] indicate that increased electron collection should occur due to sheath effects.

4.3 Plane probe aligned parallel to flow

Aligning the probe surface parallel to the ion flow we have shown that the ion current due to the flow can be eliminated and so its influence on the overall IV characteristic might be avoided. An example of an IV characteristic obtained in this orientation is shown in Fig.4.9(a).

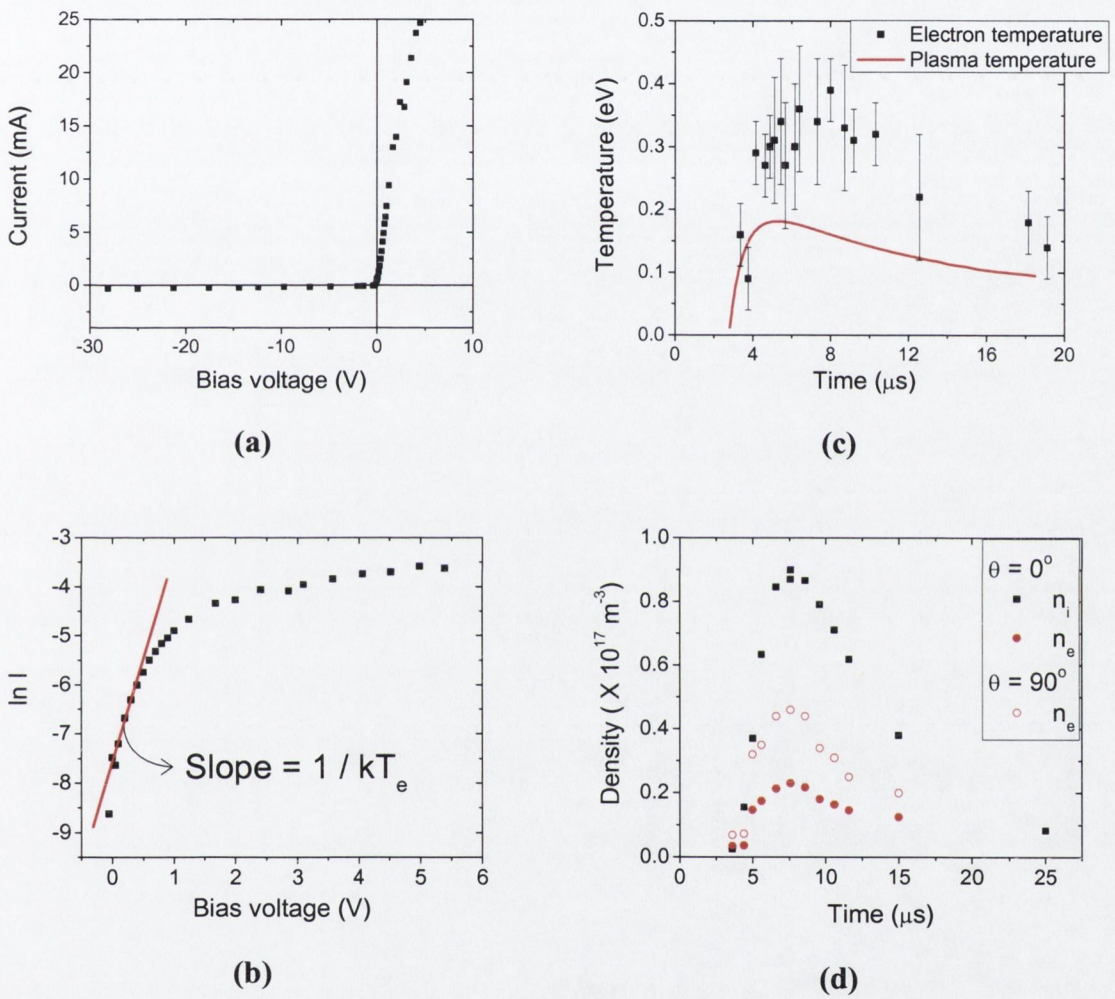

Fig.4.9 (a) The IV characteristic corresponding to the peak ion TOF (4.8 μs). **(b)** The semi-logarithmic plot **(c)** The variation of the measured electron temperature as the plasma flows past a probe compared to the calculated plasma temperature from the Anisimov model **(d)** The densities from both probe orientations.

We show in Fig.4.9(c) the time variation of the electron temperature determined from the IV characteristics. The temperature is seen to increase to a maximum of approximately 0.35 eV, a factor of four lower than that from the perpendicular case. The errors are larger in this case as determining the linear part of the log plot or the plasma potential is more difficult. The solid line in Fig.4.9(c) is the calculated temperature from the Anisimov model (1.12):

$$T = \frac{\varepsilon(5\gamma-3)(\gamma-1)}{2\gamma}\left(\frac{X_0 Y_0 Z_0}{XYZ}\right)^{\gamma-1}\left[1-\left(\frac{z}{Z}\right)^2\right]$$

where z is the probe distance and γ was taken to be 1.28. The electron density in Fig.4.9(d) for the parallel case is larger by approximately a factor of two. This is due to the fact that to maintain the constant current to the probe, as the temperature decreases, the density must increase.

4.4 PIII Models

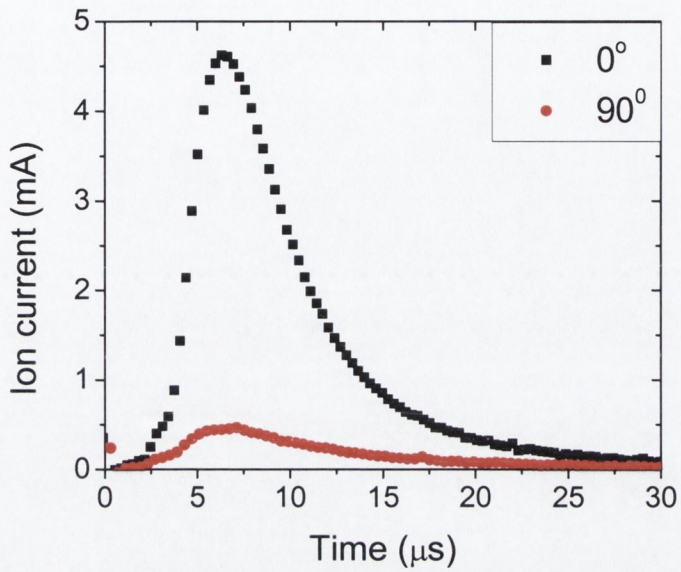

Fig.4.10 The ion TOF signal obtained at 0° and 90° with V_b = -30 V.

Fig.4.10 shows ion TOF signals obtained from both probe orientations. They were obtained using a plane probe (5 x 2 mm^2) positioned 9.2 cm from the target. If we look at the peak of the ion signal at 0° from it occurs at 6.6 μs, which corresponds to an ion flow velocity of: $v_i = 1.1 \times 10^4$ ms^{-1}. Thus it will take 0.14 μs, for this element of plasma to travel the length of the probe (2 mm). The peak ion current of 4.6 mA corresponds to an ion density of $n_i = 2 \times 10^{17}$ m^{-3}. The plasma ion frequency is then $\omega_{pi} = 5.8 \times 10^7 s^{-1}$ and so the normalised time is $T = \omega_{pi}t = 8$. As this extends into the sheath expansion regime as shown in Fig.3.12, we shall have to use the Riemann model to fully describe the ion current to the probe.

If we recall the models were previously calculated for an element of plasma with the parameters: $n_0 = 1.3 \times 10^{17}$ m^{-3}, V_0 = 20 kV, and an ion flow velocity of $v_i = 1.3 \times 10^4$ ms^{-1}. We can now look at the Riemann and DCU models for an element of plasma with a more reasonable bias voltage of V_0 = -30 V, and a maximum electron temperature as determined in the previous section of T_e = 0.5 eV. With this temperature, the maximum ratio of the Child to matrix sheath, s_c/s_0 , is 1.56 where:

$$s_c = s_0 \left(\frac{2}{9} \frac{u_0}{u_B} \right)^{1/2} \tag{4.4}$$

Fig.4.11(a) shows the un-normalised output from the Riemann and Sheerin and Turner models presented in the previous chapter. If we look at the matrix extraction phase, the integral for the Riemann and DCU models gives 159 and 137 respectively, Riemann being 14 % larger. This difference is due to the Riemann model being quite sensitive to low voltages (< 200 V), whereas at larger voltages both models show good agreement. To test the validity of the models, DCU have carried out PIC simulations of the experiment. The results are shown in Fig.4.11(b) and it shows excellent agreement with the models. As a result we can now use the PIC result to describe both the matrix and sheath expansion regimes.

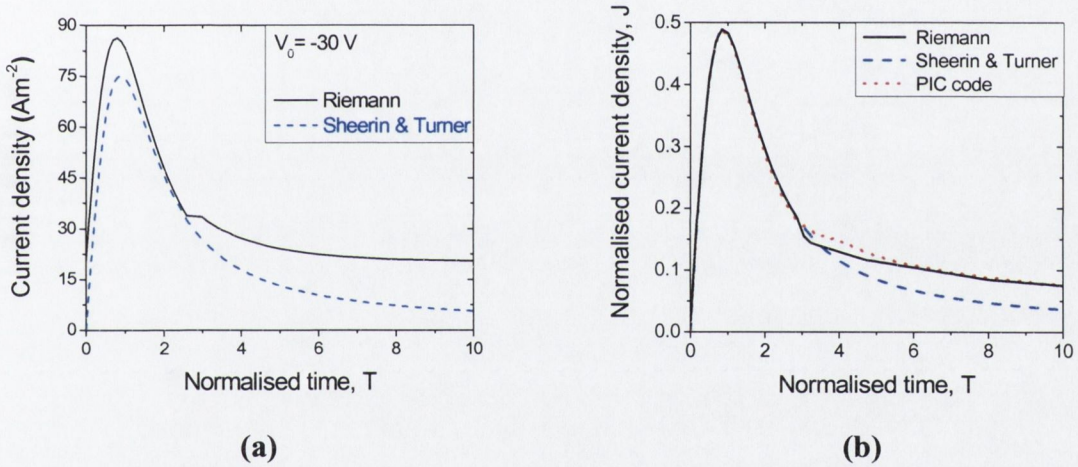

Fig.4.11 **(a)** A comparison of the Riemann and DCU for $n_0 = 1.32 \times 10^{17} m^{-3}$, $V_0 = -30$ V and $T_e = 0.5$ eV . **(b)** The two models compared to PIC calculations.

To estimate the total current contribution to the probe we consider the plume to be made up of a series of slices of plasma. Their evolution in space as they travel along the probe can be equated to the evolution in time of a static plasma in contact with a probe.

For an element of plasma we can write the current contribution as:

$$I = \int_0^L zj(x)dx \tag{4.5}$$

where x is the position of the plasma along the probe, L is the length and z is the width of the probe. If x = vt, then dx = vdt and if $T = \omega_{pi}t$, then $dT = \omega_{pi}dt$. Eqn.(4.5) can then be rewritten as:

$$I = \frac{zv}{\omega_{pi}} \int_0^{T_l} jdT$$

or

$$I = \frac{zen_0u_0v}{\omega_{pi}} \int_0^{T_l} JdT \tag{4.6}$$

where T_l is the normalised time taken for an element of plasma to traverse the probe and J is the normalised current density.

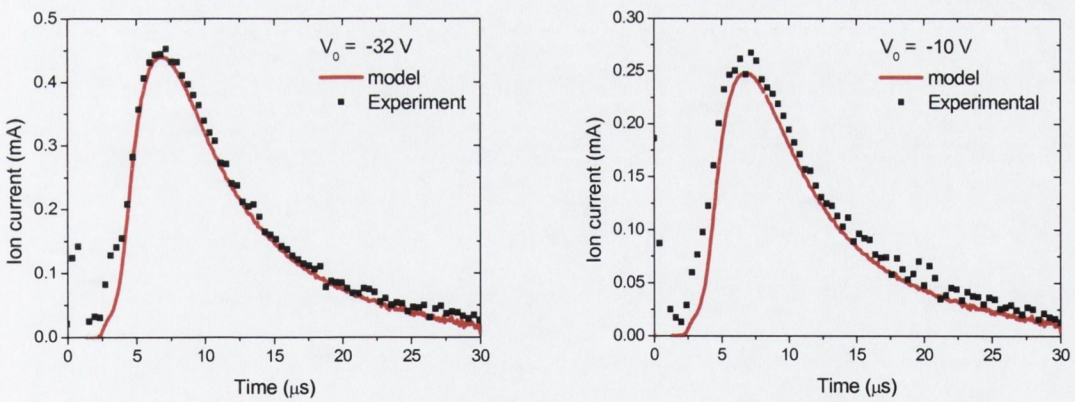

(a) **(b)**

Fig.4.12 The results from the model (4.6), compared to the experiment for two bias voltages.

The ion flow velocities and corresponding densities were obtained from the probe in the perpendicular position, and an average temperature of T_e = 0.3 eV was assumed. Depending on the time taken to traverse the probe (0.06 μs for the fastest ions to 0.66 μs for the slowest), the PIC result in Fig.4.11(b) was integrated over the relevant timescale. Fig.4.12 shows the results obtained compared to the experimental results.

It is interesting to note that the lower the electron temperature of the plasma, the longer it takes for the steady-state Child sheath to develop. For example if T_e = 0.1 eV, then T_c = 23 (the normalised time taken for the sheath to develop), while for T_e = 1 eV,

T_c = 6, Fig.4.13(a). Thus for a relatively short probe dimension (2 mm), the current is nearly independent of the electron temperature. It is also shown from the inset of Fig.4.3(a) that for these conditions the integral $\int_0^{T_1} JdT$ depends only very weakly on the value of V_0, so that from (4.6), $I \propto u_0 = \left(\frac{2eV_0}{M_i}\right)^{1/2}$. Thus we see that the model also predicts the observed dependence of the ion current on bias voltage. To investigate further the dependence of the current on the electron temperature we repeated the experiment with the plasma flow along the long dimension of an elongated probe. This axis was 13 mm and so for the same element of plasma it took 0.93 μs, (T = 54) to traverse the probe. It is clear that in this case there is enough time for the Child sheath to develop and so the integral now has a strong dependence on the temperature.

(a)

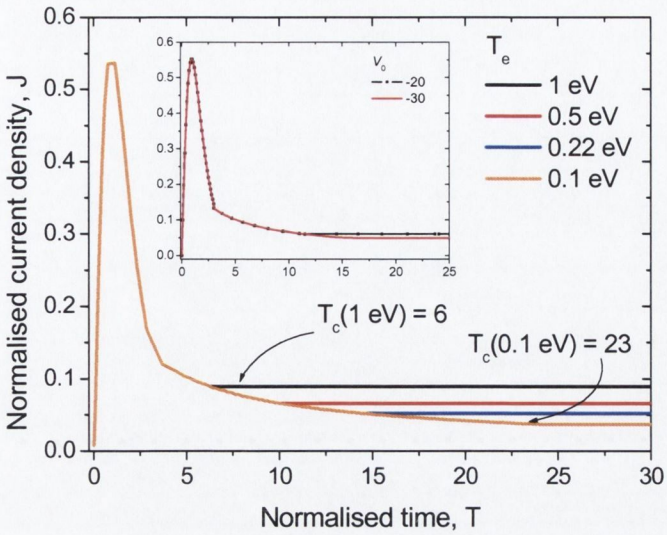

(b)

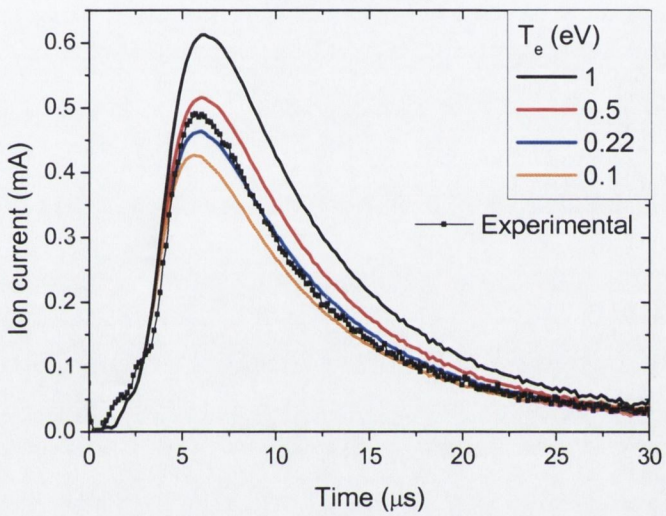

Fig.4.13 (a) The dependence of the model on the electron temperature and (inset) on the bias voltage.**(b)** The results from (4.6) for various temperatures compared to the experimental results.

Fig.4.13(b) shows the results from the model for various electron temperatures. The results suggest a temperature between $T_e = 0.22 - 0.5$ eV describes the plume at the peak TOF while a lower temperature of $T_e = 0.1 - 0.22$ eV fits at later times. These results are in good agreement with the electron temperatures determined in the parallel case.

4.5 Conclusion I

The results so far describe the plasma properties obtained using the different probe orientations. From the measured TOF signal the adiabatic index was estimated to be 1.28. However with this value the calculated TOF from the Anisimov model shows disagreement at late times. Using a lower value of γ would broaden the calculated signal, which suggests that 1.28 is an overestimation of the value.

The energy to mass ratio of 6×10^7 J Kg^{-1} indicates an average energy of 67 eV per atom or ion. From the ion energy distribution obtained from the probe results, the average energy is determined to be 110 eV with a most probable energy of 30 eV. From the mass loss results we determined that the plume absorbs approximately 45 % of the laser energy, which is a reasonable result if we take into account losses during the evaporation of the material.

Comparing the ion yield to the mass loss results indicates an ion fraction of 0.5. The discrepancy between the yield estimated from the deposited film and the measured mass loss is probably due to material removal due to the impact of the high-energy ions. The sputtering yield estimated from the difference is of the same order as determined by Faher of 0.5. This raises an interesting question as to whether the resputtered material will interact with the incoming plume. As the ions with the greatest energy are
found along the target normal, the effect will be largest here. This is also another advantage of aligning the probe parallel to the flow.

The electron temperature is probably one of the more difficult properties to measure in a laser-produced plasma. The temperature measured in the perpendicular case
using the corrected IV characteristics was a factor of four higher than that of the probe aligned parallel to the flow. This indicates that the ion flow has a large influence on the measured parameters. The peak in the measured temperature occurred at approximately 7 μs, which is later than the peak of the ion probe signals. This agrees with the results from the Anisimov model, Fig.1.4(b). The variation in temperature within the plume indicates that it is valid to use the adiabatic isentropic model of Anisimov to describe the plasma expansion.

Finally the ion density can be determined in the parallel case using the models of PIII. In addition the electron temperature could be determined by using a longer probe that allowed a Child sheath to develop. The agreement between the theoretical and experimental values of T_e, indicate it is valid to use the probe aligned parallel to the flow to obtain the temperature.

4.6 Multiply ionised species and contamination

The ion current to the probe as it rotates from 0° to 90° is well understood as the current is due to the ion flux and the magnitude depends on the area of the probe projected towards the flow direction. As the probe rotates beyond 90° the behaviour is not so clear. The signal begins to split into three distinct peaks with the early peaks TOF remaining relatively constant from 3 to 5 μs.

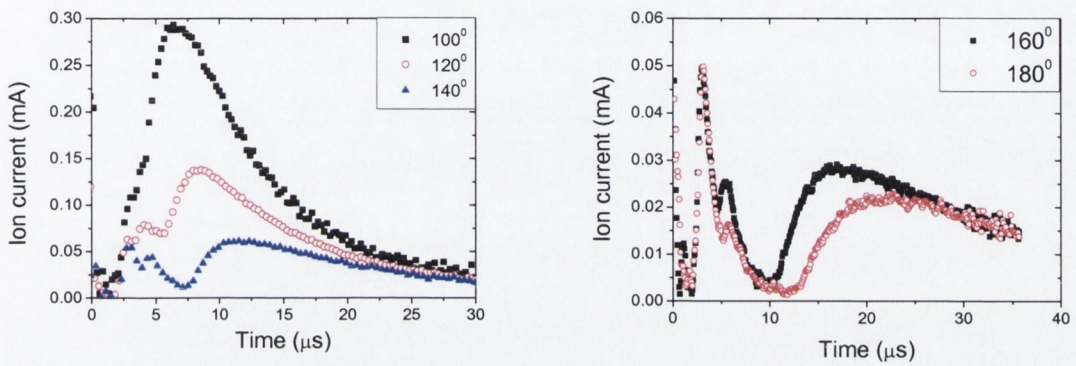

Fig.4.14 Ion current variation with probe angle, (100 – 180°) relative to the target. The probe bias was maintained at –32 V.

Fig.4.14 shows the ion TOF as the probe was rotated beyond 90°. During the experiment the target was continually rotating at ~1 Hz with the beam spot 1.3 cm off centre. If we stopped the rotation we found the magnitude of the peaks to decrease significantly (Fig.4.15), which suggests they are mostly surface contaminants. If we look at the result for 180°, the average ion energy from the silver peak is ~ 10 eV. If we assume the fast ions have the same energy distribution then their masses should range between 1 – 12 amu. These results indicate the presence of hydrogen, carbon or oxygen within the plume. Fig.4.15 also indicates that the recontamination time is greater than 1 second as there is little difference between a rep rate of 1 or 10 Hz. The beam spot was 0.5 mm in height so at a rep rate of 10 Hz there is still 7.5 mm between subsequent spots. We have found that a time interval of approximately 5 seconds is sufficient for the contamination peak to return after cleaning.

Whether this contamination originates from the surface of from the bulk of the target is not yet clear. The results suggest that a stationary target significantly reduces contamination during ablation, however the resulting cratering of the target is a major drawback.

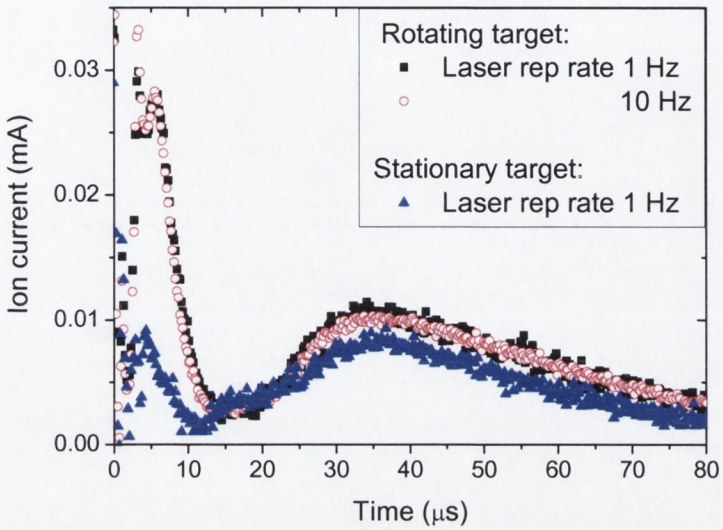

Fig.4.15 The ion current variation at 180° with the target rotation and laser rep rate. The contamination peaks drop significantly when the target is stationary indicating cleaning of the surface by the laser. The probe bias was maintained at – 32 V and the results were averaged over 10 shots.

While the current to the probe is predominately due to silver ions in the perpendicular case, we now see that there is a comparable contribution from surface contaminants in the range $\theta = 90^\circ - 180^\circ$.

Up to this point we have considered the plasma to consist of singly ionised silver ions, electrons and neutrals, and as most of the results presented in this thesis were carried out with a fluence of 1 to 2 J cm^{-2} the assumption seemed reasonable [6]. We have attempted to create multiply ionised species by ablating with higher fluences (4 J cm^{-2}). We kept the target stationary and used a repetition rate of 10 Hz to keep any contamination contribution to a minimum.

Fig.4.16 shows the ion current to the probe for various fluences. The fast peak dominates for fluences greater then 1.5 J cm^{-2} and with a TOF similar to the contamination peaks.

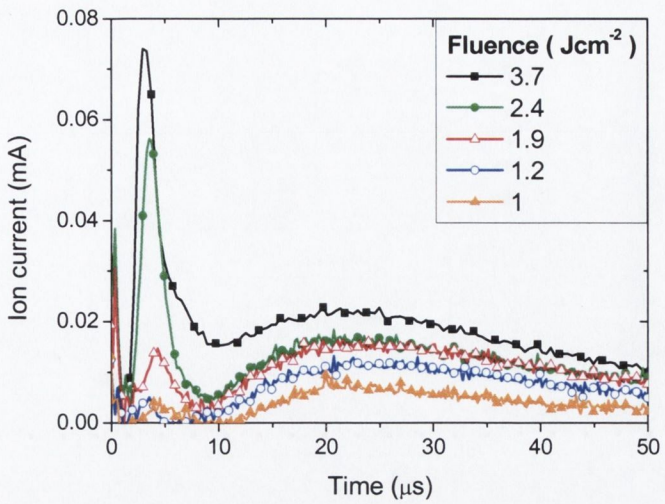

Fig.4.16 The ion current at 180° with varying fluence. The fast peak appears at approximately 1.5 J cm^{-2}. The probe bias was maintained at -32 V and the results were averaged over 10 shots.

The origin of these peaks are difficult to understand using only Langmuir probe results. As a result we designed and assembled the ES-TOFMS to identify these peaks and their energy distribution.

4.7 Energy Selective-Time of Flight Mass Spectrometer

We described in chapter 2 the specifications of the ES-TOFMS. Briefly two curved parallel plates were biased to allow only ions of a particular energy through to a detector. By varying the bias, a particular pass energy could be selected. Using this apparatus we should be able to distinguish between species of different charge states and contamination [6, 7]. The spectrometer was placed 30 cm along the target normal and had an energy range of 0 – 350 eV assuming singly ionised species. From Fig.4.2(b) this covers most of the measured ion energy distribution.

(a)

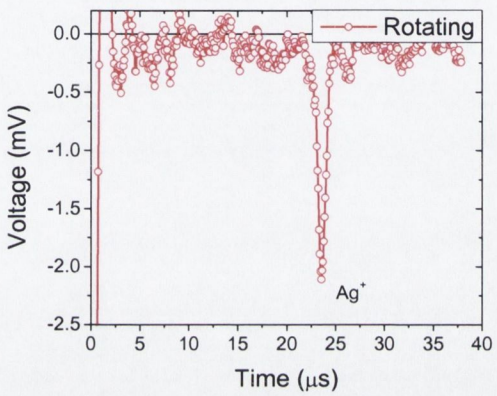

(b)

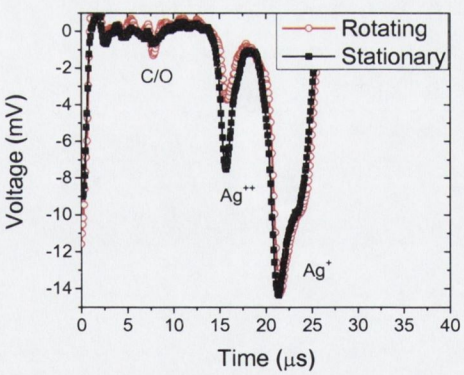

Fig.4.17 (a) The output from the analyser for a rotating silver target ablated at 1.1 J cm^{-2}. The target to detector length was 34.6 cm and the bias on the plates was ± 11 V, which corresponds to a pass energy of 119 eV. **(b)** The output for a rotating and stationary silver target ablated at 3.7 J cm^{-2}. The pass energy was 130 eV for Ag^{+} and C/O; and 260 eV for Ag^{++}.

Fig.4.17 (a) shows the typical output from the spectrometer. It was obtained from a rotating silver target ablated at a fluence of 1.1 J cm^{-2}. We show in Fig.4.17(b) the spectrum for ablation at the highest fluence obtainable of 3.7 Jcm^{-2}. It indicates that doubly ionised Ag is present and that rotating the target contributes contamination to the plume. The mass-to-charge ratio of the ion is determined by:

$$\frac{E}{Z} = \frac{e\Delta V R_0}{2d}$$
$$\therefore \frac{m}{Z} = \frac{e\Delta V R_0}{dv_i^2} \tag{4.7}$$

E is the ion energy in J, m is its mass, Z is the ion charge, ΔV is the voltage on the analyser(0 – 64 V), R_0 is the mean spectrometer radius (3.5 cm) and d is the plate separation (3 mm). The pass energy of the spectrometer in eV is calculated by:

$$E_{pass} = \frac{Z\Delta V R_0}{2d} \tag{4.8}$$

The error in the TOF can be estimated as shown in chapter 2:

$$\frac{\Delta E_{filter}}{E_{filter}} = \frac{\Delta R}{R} = \frac{2\Delta v}{v} = \frac{-2\Delta t}{t}$$
$$\therefore \Delta t = \frac{t}{2}\frac{\Delta R}{R} \tag{4.9}$$

For a TOF of 23.56 μs, ΔR = 3 mm and R =R_0, then Δt = 1.09 μs. This compares to a FWHM of 1.04 μs obtained from the experiment. One of the basic characteristics of a spectrometer is its resolving power. The mass resolution of an analyser is given by [8]:

$$R_m = \frac{m}{\Delta m} = \frac{t}{2\Delta t} \tag{4.10}$$

where t is the TOF of an ion that may be resolved from a neighboring ion, and Δt is the time between the resolved ion pulses.

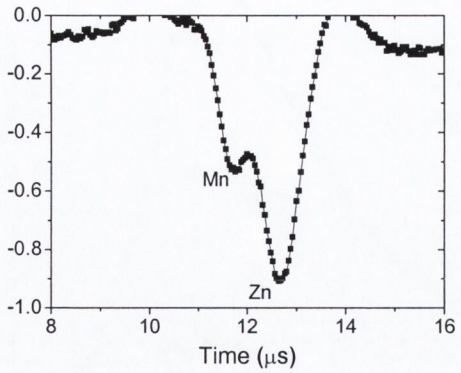

Fig.4.18 The output for the ablation of a ZnMn target showing the resolving power of the spectrometer.

Fig.4.18 shows the output from the ablation of a ZnMn target. The mass resolution was determined to be 6 with $\Delta t = 0.88$ μs. We also ablated a ZnCuO target to test the resolving power but could not distinguish between the Cu and Zn peaks.

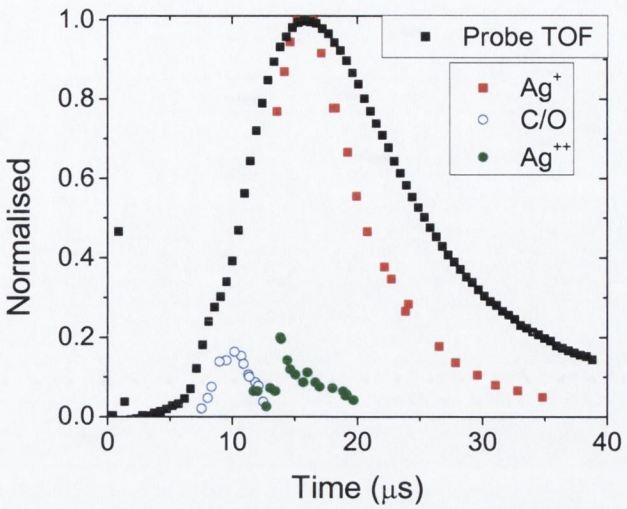

Fig.4.19 The normalised ion probe TOF signal, adjusted for the spectrometer distance compared to the TOF's of the ion species from the spectrometer for a fluence of 3.7 J cm^{-2}.

Fig.4.19 shows the magnitude and arrival time of the C/O and Ag^{++} peaks compared to the Ag^{+} peak for a fluence of 3.7 J cm^{-2}. The proportion of Ag^{++} and C/O to Ag^{+} is relatively small with the majority of ions being singly ionised. The fast peak in the probe signal can now be identified as due to contamination. Fig.4.20(a) shows the results obtained for a full energy spectrum of Ag ablated at 1.1 J cm^{-2}. The results indicate the presence of only singly ionised silver, with the maximum flux occurring at approximately 110 eV. The TOF for other ions we might expect to observe, such as Ag^{++} would be: $Ag^{++} = 0.7Ag^{+}$, $S = 0.55Ag^{+}$, $O = 0.38Ag^{+}$, $C = 0.33Ag^{+}$ and $H = 0.1Ag^{+}$. If the abundance of these species are 10 – 20 % that of the silver they should be detectable. The only difficulty would be interpreting a peak that contains the lighter elements of carbon and oxygen, as their peaks would be too close to differentiate.

At a fluence of 2.1 J cm^{-2}, Fig.4.20(b), we observe three peaks for a rotating target. Their mass-to-charge ratios correspond to singly and doubly ionised silver with a low Z contamination, probably carbon, though oxygen falls within the errors. By stopping the rotation the contamination peak is eliminated as we effectively clean the

target. The doubly ionised silver then extends to higher energies with the peak at ~275 eV. We found that similar to the probe results presented in the previous sections, the recontamination time corresponded to approximately 5 s. Finally, for the maximum fluence of 3.7 J cm^{-2}, the results show a similar trend but with the peaks extending to higher energies.

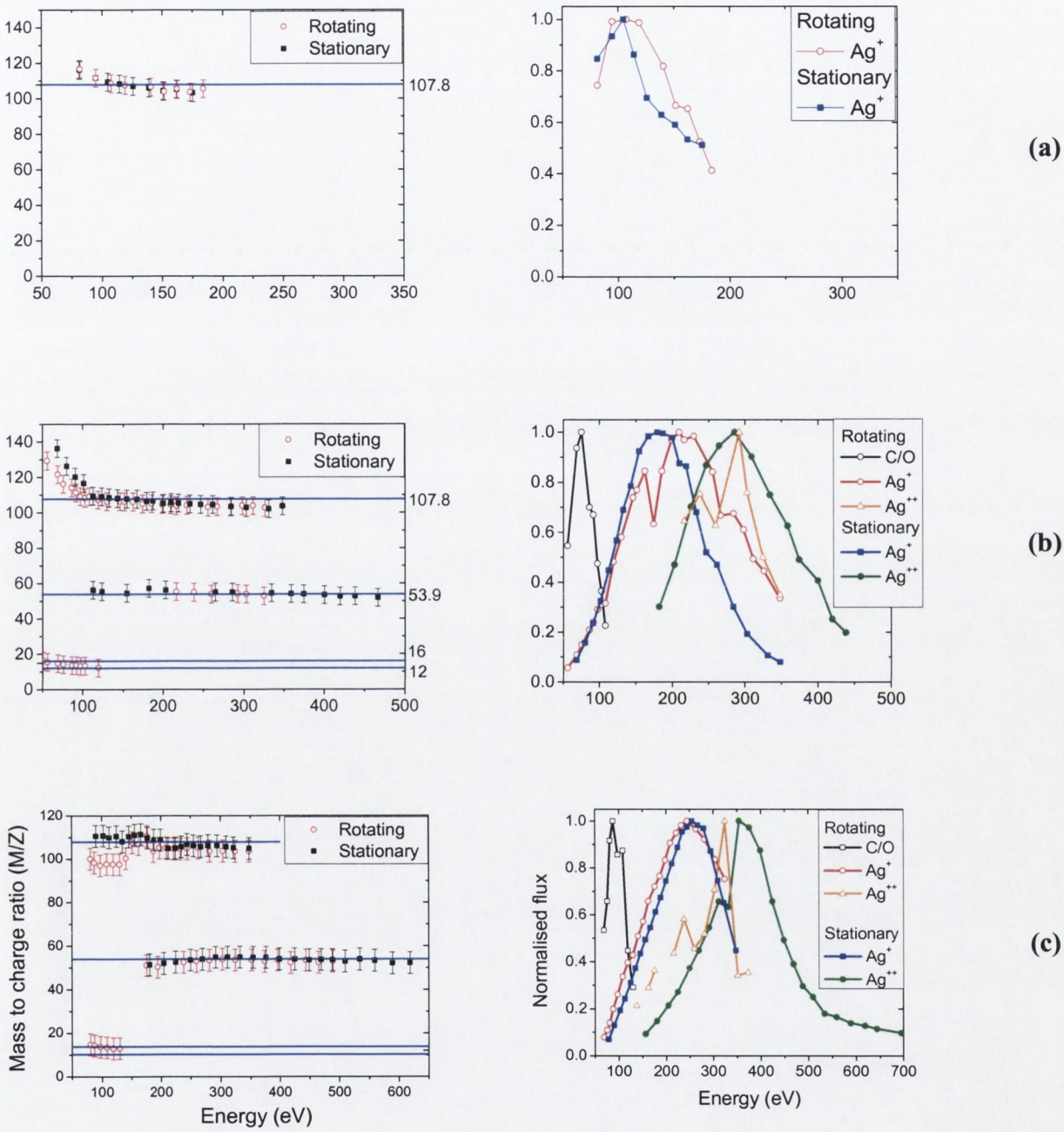

Fig.4.20 The energy spectra and distribution for Ag ablated at a fluence of: **(a)** 1.1 J cm^{-2} **(b)** 2.1 J cm^{-2} **(c)** 3.7 J cm^{-2}.

We have been unable as yet to identify the low Z contamination species. We ablated calcite (calcium carbonate – $CaCO_3$) and perspex (PMMA) at the maximum fluence in an attempt to produce carbon, oxygen or hydrogen ions but none were detected by the spectrometer. It is clear though that the contamination becomes significant at fluences above 1.5 J cm^{-2}. Similar results were observed by Woryna *et al* [9] who investigated the impurity layers of Ta, W and Au. They identified the contamination to consist of H, C and O atoms with a recontamination time of several seconds.

Comparing Ag^+ from Fig.4.20 we see little difference in the distribution at low fluence, (a), for a stationary and rotating target with the peak occurring at ~ 100 eV. This is similar to that determined from the ion TOF signals. At the high fluence, (c), the distribution is again similar but occurring at higher energies of 250 eV. Stopping the rotation increases the Ag^{++} distribution, with ions detected up to 700 eV, but with only a slight increase in the peak energy from about 300 to 350 eV.

We have not come across any other results for silver, though similar work has been carried out on the ion energy distribution of tantalum for low [10] and high [11] irradiances although at a higher wavelength of 1064 nm. Tantalum was chosen in their experiments due to its high mass of 181 amu. At low laser energies, 10 – 60 mJ, most of the ions for all angles were Ta^+ with energies up to 1000 eV detectable (though ions of up to Ta^{4+} were seen), with the average charge determined to be 1.6. At higher energies [11], (1 – 900 mJ per pulse, fluence = 10 – 100 J cm^{-2}) the tantalum charge state could reach 8+ with the maximum ion energy of 6 keV observed. They determined the mean energy of Ta^+ to be 250 and 1000 eV for fluences of 30 and 100 J cm^{-2} respectively.

Similarly the kinetic energy distribution of ions produced during XeF ablation of Al and Cu has been investigated by [7, 12]. For fluences between 1 – 4 J cm^{-2} they observed a bimodal distribution. The first peak occurred at ~ 1 eV which they related to a thermionic component. The second peak extended up to 60 eV for Cu ions ablated at 3.2 J cm^{-2}. They also observed Cu^{++} at this fluence though very little compared to the Cu^+ peak.

In the results presented in Fig.4.20, the deviations at low energies in the energy spectra could be due to the error in determining the TOF due to the large width of the peaks and/or due to space charge effects. By placing a probe at the entrance to

the spectrometer we can determine the density of the plasma at the slit. For a fluence of 1.1 J cm^{-2} the maximum ion density corresponded to $n_i = 2.3 \times 10^{15}$ m^{-3}. With a slit width of 50 μm the field due to space charge, E_{space}, corresponds to 1000 V m^{-1} (2.2). Applying a bias of ± 10 V, (E_{pass} = 100 eV), corresponds to an electric field of ~ 6000 V m^{-1}. Thus space charge effects should be a minimum above this pass energy. The effect can be further reduced by increasing the target-spectrometer distance thus reducing the density or by simply using a smaller slit. However we found that when using a 10 μm slit, we were unable to resolve the low Z elements. Fig.4.21(a) shows the ion TOF signals obtained from the probe at the spectrometer entrance. Fig.4.21(b) is the corresponding ion energy distribution. The average energies for the fluences of 1.1, 2.1 and 3.7 J cm^{-2} are 70, 140 and 190 eV respectively which are in reasonable agreement with the energy distributions from the spectrometer.

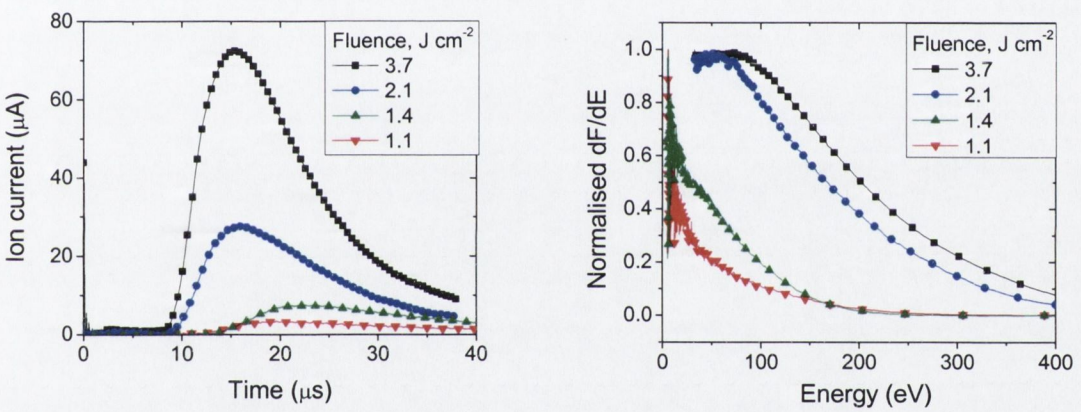

(a) **(b)**

Fig.4.21(a) The ion TOF signals for various fluences obtained from a probe at the spectrometer entrance. **(b)** The normalised ion energy distribution obtained from the TOF results.

Fig.4.22(a) shows the ion TOF signal for a fluence of 3.7 J cm^{-2} on the rotating and stationary target. Fig.4.22(b) shows the TOF for the stationary target compared to the full spectrometer results. The time of maximum ion flux through the spectrometer corresponds to the peak in the probe TOF signal once the extra length (5.4 cm) is taken into account. It shows that a substantial number of the low energy ions are not detected. This is not too surprising as these ions take the longest to travel through the

spectrometer. As a result beam 'blow-up'(space charge effect) will have a larger influence, reducing the final flux onto the detector.

We have taken the overall signal to approximate an ion TOF signal in an attempt to determine the total ion transmission. We used similar data to Fig.4.22(b), but using the results for 1.1 J cm^{-2} where we now know that the current is due to singly ionised silver. By integrating the probe signal we determined that 2.3 x 10^{8} ions enter the spectrometer. The detector only received 1.5 x 10^{16} ions which equates to 0.7 %.

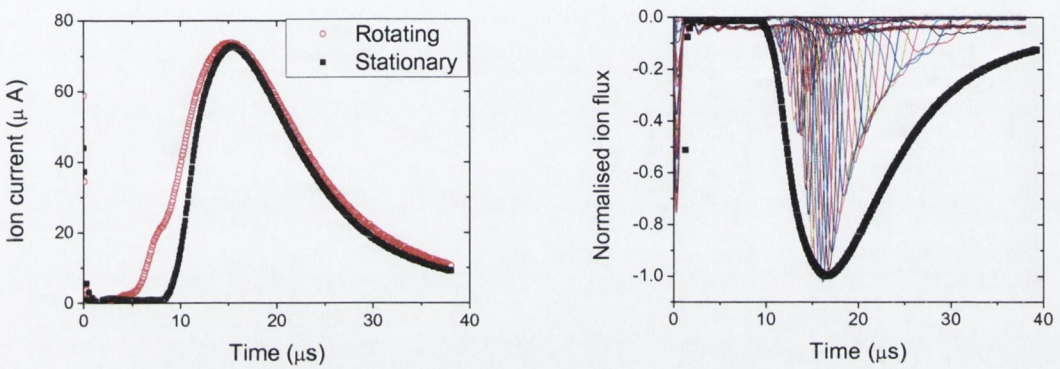

(a) **(b)**

Fig.4.22 (a) Ion TOF signals obtained at the entrance to the spectrometer for a fluence of 3.7 J cm^{-2}. The contribution due to contamination can be clearly seen **(b)** The inverted TOF signal for the stationary target (corrected for spectrometer length) compared to the full spectrometer results.

4.8 Conclusions II

Rotating the probe beyond 90° split the ion signal into three distinct peaks, with fast peaks occurring between 3 – 5 μs with the main silver peak moving to later times of 10 – 40 μs. We found that using a stationary target reduced these fast peaks considerably which suggests they are due to contamination from the target surface. However even with a stationary target for fluences greater than 1.5 J cm^{-2} a fast peak was detected.

The ES-TOFMS has proved to be a useful device, identifying the different species within the plume. With the target rotating or stationary we detected only Ag^+ at low fluence (1.1 J cm^{-2}). At higher fluences (>1.5 J cm^{-2}) there was a substantial difference between a rotating or stationary target. With a rotating target contamination due to carbon or oxygen was present. Doubly ionised silver was also at these higher fluences with energies extending up to 700 eV at the maximum fluence of 3.7 J cm^{-2}. The transmission of the spectrometer is quite poor as it is clear that few of the lower energy ions are detected. The wide peaks at these lower energies also give rise to large errors in determining their TOF which limited the spectrometers energy range.

4.9 References

1. Hansen, T.N., Schou, J., and Lunney, J.G., *Applied Physics A (Materials Science Processing)*, **69**(suppl.): p. 601(1999).
2. Toftmann, B., *Laser ablation of soft and hard materials - a study on deposition and characterization*, in *Riso National laboratory*. 2004: Roskilde, Denmark.
3. Fahler, S., Sturm, K., and Krebs, H.U., *Applied Physics Letters*, **75**(24): p. 3766(1999).
4. Weber, W.J., Armstrong, R.J., and Trulsen, J., *Journal of Applied Physics*, **50**(7): p. 4545(1979).
5. Stamate, E. and Ohe, K., *Applied Physics Letters*, **78**(2): p. 153(2001).
6. Amoruso, S., *et al.*, *Applied Surface Science*, **106**: p. 507(1996).
7. Amoruso, S., *et al.*, *Applied Surface Science*, **138-139**: p. 250(1999).
8. Woryna, E., Parys, P., Wolowski, J., and Mroz, W., *Laser and Particle Beams*, **14**(3): p. 293(1996).
9. Dinger, R., Rohr, K., and Weber, H., *Journal of Physics D (Applied Physics)*, **17**(8): p. 1707(1984).
10. Dinger, R., Rohr, K., and Weber, H., *Journal of Physics D (Applied Physics)*, **13**(12): p. 2301(1980).
11. Torrisi, L., Gammino, S., Ando, L., and Laska, L., *Journal of Applied Physics*, **91**(7): p. 4685(2002).
12. Amoruso, S., Berardi, V., Bruzzese, R., Spinelli, N., and Wang, X., *Applied Surface Science*, **127-129**: p. 953(1998).

Conclusions and future work

This thesis has attempted to further the application of Langmuir probes to laser produced plasmas. At this point it is worth summarising the main achievements from the thesis and considering some aspects which may be worth investigating further.

Scientific advances

The adiabatic expansion models of Anisimov and Singh and Narayan were shown to be very useful in describing the plasma expansion into vacuum. Both models have been used extensively in the literature to describe a typical ion time-of-flight signal with equal accuracy; however there was clearly a need to clarify which treatment of temperature was correct. One of the main achievements of this thesis was in determining, that for typical ns ablation conditions, the plasma can be treated as isentropic, provided the plasma temperature is less than 12 eV. As the plasma temperature at the target is usually below this, the Anisimov model can be applied to our results.

The ion flow velocity and ion energy distribution can be obtained quite easily from an ion TOF signal. This assumes that the probe distance is much larger than the ion source size and that the ion TOF is much longer than the ion production time. This is generally the case as the probe distance is usually a few centimetres away and the ion TOF is typically of the order of μs compared to ns for the ion production time. We show however, that the Anisimov model can determine the plasma formation and acceleration time. Subsequently, the ion TOF signals can be corrected for, before further analysis.

Diagnostic advances

The perturbation of the plasma by the probe was considered in detail in chapter 3. The work by Waymouth derived a relationship between the probe area, plasma temperature and a minimum number of electrons. The calculations by Sheridan provided a useful description of the sheath edge effects. He found significant effects even with a relatively large probe area. For example, a disk probe with a diameter of 1 mm, biased at – 30 V has a sheath with an area of up to twice the probe area. While

these two models are applicable to stationary plasmas and the probes were double sided, they can be used together to initially design a probe, large enough to keep edge effects to a minimum yet small enough to avoid perturbing the plasma.

With a suitably sized planar probe, we studied the behaviour where it is orientated so that the plasma flow is parallel to the collecting surface of the probe. In this way the ion current due to the ion flow can be eliminated. In this orientation we found similarities with the technique of plasma immersion ion implantation. The plasma flowing across the probe surface can be taken as slices of plasma, which are in contact with the probe for a certain length of time. The current to the probe will depend on the type of sheath formed. A fast element of plasma will be in contact long enough for only a matrix sheath to form, whereas a slow element will allow a Child-Langmuir sheath develop. The implantation models show that if the probe is long enough for a Child-Langmuir sheath to develop then the current to the probe is proportional to the electron temperature. This provides an independent means of determining the electron temperature. The results were consistent with the assumption that the plume is isentropic and the expansion is adiabatic.

Finally we produced multiply ionised species by ablating at high fluences. By using the ES-TOFMS, the mass-to-charge ratios of the various species and their energy distribution could be determined. Typically we found that for moderate fluences, we could detect doubly ionised silver with energies up to a few hundred eV. Interestingly, we found that a rotating target produced a 'contamination' peak which had energies up to 100 eV. Using a stationary target eliminated this peak, but also had the effect of increasing the energy range of the doubly ionised silver.

Current research / future work

The theory used to describe the ablation process and subsequent plume expansion was presented in chapter one. The laser heating model developed by Lunney and Jordan was a useful tool in that it describes the target heating and subsequent ablation rate. Although the model was found to give good agreement with the experimental results for iron and magnesium close to the fluence threshold, we have had difficulty in correlating it to our results for the ablation of silver. The discrepancy could be due to a number of reasons.

The most probable is that we took as constant the thermal conductivity of silver. This model is constantly being reviewed, and at the present we are working on including a temperature dependent value for the thermal conductivity.

The work presented in this thesis concerned rotating the probe from 0° to 90°. Currently we are continuing this work to where the probe is rotated 180°. This is being done with an aim to understanding Mach probe behaviour. Mach probes are essentially double sided planar probes. They are inserted into the path of a flowing plasma to determine the flow velocity by comparing the current collected from the upstream and downstream face. In conjunction with our experimental results, theoretical calculations are bring carried out in DCU to provide a description of the ion current to the probe in the downstream orientation.

The laser ablation of multi-component targets is a common procedure. However questions concerning preferential ablation rates, different yields and energy distributions remain. The ES-TOFMS has proved itself capable of answering these questions. At present a more compact spectrometer is being designed which will allow us to determine the angular and energy distribution of multi-component plasmas. Finally, by increasing the resolution the contamination peak will be identified.

Appendix A: Laser heating model

Properties of the laser pulse:

$$f[n_] := f_0 * \frac{n}{(3.35 \times 10\text{^}{-7})} * \text{Exp}\left[-\left(\frac{n}{26}\right)^2\right];$$

(* Analytical expression for temporal profile of laser irradiance *)

$f_0 = 2;$ (* Average laser energy fluence [J cm^{-2}] *)

$x = 1;$ (* Timestep [ns] *)

$\Delta\tau = x \times 10^{-9};$ (* Timestep [s] *)

tmax = 100; (* Calculation limit in time (timesteps after start of laser pulse) *)

spot = 0.0126; (* Laser spot area [cm^2] *)

$\delta t_{pulse} = 26 \times 10^{-9};$

(* FWHM of laser pulse *)

Properties of silver:

(*Thermal and physical properties*)

$\kappa = 4.29;$ (* Thermal conductivity of target material [W cm^{-1} K^{-1}] *)

$\rho = 10.5;$ (* Mass density of target [g cm^{-3}] *)

SpecHeat = 25.4; (* Molar heat capacity [J K^{-1} mol^{-1}] *)

c = 0.235; (* Specific (mass) heat capacity [J K^{-1} g^{-1}] *)

$M_{molar} = 107.87;$ (* Molar mass of evaporating species [a.m.u.] *)

$k_B = 1.38 \times 10^{-23};$ (* Boltzmann constant [J K^{-1}] *)

HeatVap = 258; (* Heat of vaporisation [kJ mol^{-1}] *)

$Lv = \frac{\text{HeatVap} \times 10^3}{N_{Av}};$ (* Latent heat of vapourisation per particle [eV] *)

T0 = 300; (* Initial target surface temperature [K] *)

$T_{boil} = 2436;$ (* Boiling temperature at standard pressure (10^5 Pa) [K] *)

k = 1.39; (* Extinction coefficient at 248 nm *)

$\lambda = 248 \times 10^{-9};$ (* Laser wavelength *)

ref = 0.2; (* Surface reflectivity of target to laser radiation *)

$N_{Av} = 6.022 \times 10^{23};$ (* Avogadro's constant *)

$a_m = 1.66 \times 10^{-27};$ (* Atomic mass unit [kg] *)

$\sigma = 1.3 \times 10^{-17};$ (* Absorption cross-section in plume for 248 nm radiation *)

$$A = \frac{2(1 - \text{ref}) * \sqrt{\Delta\tau}}{\sqrt{\pi * \kappa * \rho * c}};$$ (* Constant factor in temperature evaluation *);

$$r = \sqrt{\frac{t - n + x}{x}} - \sqrt{\frac{t - n}{x}};$$

(* Parameter determining contribution of previous time intervals to present temperature *);

(* Surface temperature calculation *)

(* Expression for surface temperature as a function of time:*)

(* $T(t)=\frac{(1-ref)}{\sqrt{\pi*K*\rho*C}}\int_0^t \frac{f(t-\tau)}{\sqrt{\tau}}\,d\tau=\lim_{i\to\infty}\sum_{n=1}^{i} f(t-\tau_n)\times\frac{\Delta\tau_n}{\sqrt{\tau_n}}\simeq\sum_{n=1}^{s} f(t-\tau_n)\times\left(\sqrt{(s-n)+1}-\sqrt{s-n}\right)\times\sqrt{\Delta\tau}$ *)

```
Irradiance = {};
TempList = {0};                    (* Surface temperature at each timestep *)
TotalVapour = {0};                 (* Flux of particles evaporated during each timestep *)
Massloss = {0};                    (* Mass of particles evaporated during each timestep *)
PressVap = {};

For[t = x, t ≤ tmax, t += x, Irradiance = Append[Irradiance, f[t]]];
(* Irradiance values before vapour attenuation *)

TempList = Append[TempList, A * Irradiance[[1]]];   (* Temperature increase for first timestep *)

P_Ag = 10^5 * Exp[ Lv/k_B × ( 1/T_boil - 1/Tsurf ) ];          (* Vapour pressure [Pa] *)

Rate = 10^-4 × P_Ag × Sqrt[ 1 / (2 × π × k_B × a_m × M_molar × Tsurf) ];   (* Evapouration rate [particles cm^-2 s^-1 *)

InstFlux = Rate × Δτ;                                          (* Flux for individual timesteps [cm^-2] *)
```

```
(* Routine for calculating Surface temperature,Vapour pressure and evaporation rate *)

For[t = 2 x, t < tmax, t += x,
  Tsurf = T0 + Sum[((A * Irradiance[[n/x]]) * r * Exp[-(σ x TotalVapour[[(n-x)/x]])/0.866]), {n, 2 x, t, x}];
  TempList = Append[TempList, Tsurf]; PressVap = Append[PressVap, P_Ag];
  TotalVapour = Append[TotalVapour, (TotalVapour[[(t-x)/x]] + InstFlux)]];

Massloss = TotalVapour x M_molar / N_Av x spot;

TotMass = Last[Massloss] "(= Total mass Ag evaporated per laser shot [grams] )"

AblDepth = TotMass / (ρ * spot) x 10^7 "(=ablation depth (nm))" "(* Ablation depth per pulse in nm *)"

("Note: time scale in units of timestep (x=0.5 ns) e.g. 200 on scale = 100 ns ")
```

(*Optical absorption and thermal diffusion depth calculations*)

```
Diffusivity = κ / (ρ * c);                    (* Thermal diffusivity [cm^2 s^-1] *);

d_abs = N[10^9 x λ / (4 * π * k)]   "(absorption depth in nm)"   (* Optical absorption depth @ 248 nm [cm] *)

d_diff = N[10^7 x √(Diffusivity x δt_pulse)]   "(Diffusion length in nm)"   (* Thermal diffusion length [nm] *)
```

Appendix B: Light transmission calculation

```
Clear[r1];
Clear[r2];
Clear[β];
Clear[Ref];
Clear[t1];
Clear[t2];
Clear[Trans];
n1 = 1;
n2 = 0.14 + 4.15 i;
n3 = 1.5;
λ = 635;
d = 12;
β = 2 π n2 d / λ;
r1 = (n1 - n2) / (n1 + n2);
r2 = (n2 - n3) / (n2 + n3);
t1 = 2 n1 / (n1 + n2);
t2 = 2 n2 / (n2 + n3);
Ref = (Abs[(r1 + (r2 Exp[- 2 i β])) / (1 + (r1 r2 Exp[- 2 i β]))])^2;
Trans = (n3 / n1) (Abs[(t1 t2 Exp[i β]) / (1 + r1 r2 Exp[2 i β])])^2
```

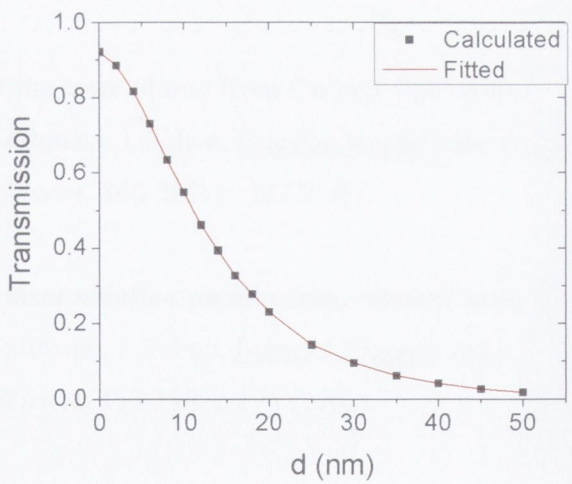

Fig.B.1 The calculated transmission of 635 nm light through a transparency as a function of thickness of silver. At d = 0 nm, T = 0.92 due to losses at the two interfaces.

Appendix C: Publications

Behaviour of a planar Langmuir probe in a laser ablation plasma

Brendan Doggett, Casper Budtz-Jorgensen, J. G. Lunney, P. Sheerin, and M. M. Turner,

Applied Surface Science, **247** (1-4): p.134 (2005).

Model for laser ablation plasma expansion in gas

Casper V. Budtz-Jørgensen, Michael M. Mond, Brendan Doggett and J. G. Lunney,

Journal of Physics D: Applied Physics, **38** (12): p.1892 (2005).

Langmuir probe study of plasma expansion in femtosecond pulsed laser ablation of silver

P. Mannion, S. Favre, G. M. O'Connor, T. J. Glynn, Brendan Doggett and J. G. Lunney,

Proc. SPIE vol **5827**, p.457 (2005).

Interaction of surface plasmons with CdTe quantum dot excitons

K. K. Vamsi, Yu. P. Rakovich, A. L. Bradley, J. F. Donegan, Brendan Doggett, T. Donnelly, J. G. Lunney, N. Gaponik and A. Susha

Proc. SPIE vol **5955**, p.137 (2005).

A comparison of the laser plume from Cu and YBCO studied with ion probes

B. Thestrup, B. Toftmann, J. Schou, Brendan Doggett and J. G. Lunney,

Applied Surface Science, **208-209**: p. 33 (2003).

Ion dynamics in laser ablation plumes from selected metals at 355 nm

B. Thestrup, B. Toftmann, J. Schou, Brendan Doggett and J. G. Lunney,

Applied Surface Science, **197-198**: p.175 (2002).